

Wrocław University of Technology  
Centre of Advanced Materials and Nanotechnology

---

# Materials Science-Poland

Vol. 28



No. 4



2010



Oficyna Wydawnicza Politechniki Wrocławskiej

**Materials Science-Poland** is an interdisciplinary journal devoted to experimental and theoretical research into the synthesis, structure, properties and applications of materials.

**Among the materials of interest are:**

- glasses and ceramics
- sol-gel materials
- photoactive materials (including materials for nonlinear optics)
- laser materials
- photonic crystals
- semiconductor micro- and nanostructures
- piezo-, pyro- and ferroelectric materials
- high- $T_c$  superconductors
- magnetic materials
- molecular materials (including polymers) for use in electronics and photonics
- novel solid phases
- other novel and unconventional materials

The broad spectrum of the areas of interest reflects the interdisciplinary nature of materials research. Papers covering the modelling of materials, their synthesis and characterisation, physicochemical aspects of their fabrication, properties and applications are welcome. In addition to regular papers, the journal features issues containing conference papers, as well as special issues on key topics in materials science.

Materials Science-Poland is published under the auspices of the Centre of Advanced Materials and Nanotechnology of the Wrocław University of Technology, in collaboration with the Institute of Low Temperatures and Structural Research of the Polish Academy of Sciences and the Wrocław University of Economics.

All accepted manuscripts are placed on the Web page of the journal and are available at the address:  
<http://MaterialsScience.pwr.wroc.pl>

All published papers are placed on the Web page of the journal and are **freely accessible** at the address:  
<http://MaterialsScience.pwr.wroc.pl>

**Materials Science-Poland is abstracted/indexed in: Chemical Abstracts, Materials Science Citation Index, Science Citation Index Expanded, Scopus.**

### **Editor-in-Chief**

Jan Felba

Faculty of Microsystem Electronics and Photonics  
Wrocław University of Technology  
Wybrzeże Wyspiańskiego 27  
50-370 Wrocław, Poland  
[jan.felba@pwr.wroc.pl](mailto:jan.felba@pwr.wroc.pl)

### **Associate Editors**

Wiesław Stręk

Institute of Low Temperature  
and Structure Research  
Polish Academy of Sciences  
P. O. Box 1410  
50-950 Wrocław 2, Poland  
[strek@int.pan.wroc.pl](mailto:strek@int.pan.wroc.pl)

Jerzy Hanuza

Department of Bioorganic Chemistry  
Faculty of Industry and Economics  
Wrocław University of Economics  
Komandorska 118/120  
53-345 Wrocław, Poland  
[hanuza@credit.ac.wroc.pl](mailto:hanuza@credit.ac.wroc.pl)

### **Advisory Editorial Board**

Frédéric Bernard, Dijon, France  
Mikhaylo S. Brodyn, Kyiv, Ukraine  
Alexander Bulinski, Ottawa, Canada  
J. Paulo Davim, Aveiro, Portugal  
Roberto M. Faria, São Carlos, Brazil  
Andrzej Gałęski, Łódź, Poland  
Reimund Gerhard, Potsdam, Germany  
Paweł Hawrylak, Ottawa, Canada  
Andrzej Klonkowski, Gdańsk, Poland  
Shin-ya Koshihara, Tokyo, Japan  
Krzysztof J. Kurzydłowski, Warsaw, Poland  
Janina Legendziewicz, Wrocław, Poland

Jerzy Lis, Cracow, Poland  
Tadeusz Luty, Wrocław, Poland  
Bolesław Mazurek, Wrocław, Poland  
Ram M. Mehra, New Delhi, India  
Jan Misiewicz, Wrocław, Poland  
Jerzy Mroziński, Wrocław, Poland  
Krzysztof Nauka, Palo Alto, CA, U.S.A.  
Stanislav Nešpůrek, Prague, Czech Republic  
Marek Samoć, Wrocław, Poland  
Jacek Ulański, Łódź, Poland  
Vladislav Zolin, Moscow, Russia

**Editorial Secretary**  
**Marek Łata**

**Native English Consultant**  
**Daniel Davies**

**Printed in Poland**

© Copyright by Oficyna Wydawnicza Politechniki Wrocławskiej, Wrocław 2011

## Impedance and modulus spectroscopy studies of $\text{Ba}_4\text{SrSmTi}_3\text{V}_7\text{O}_{30}$ ceramics

P.S. SAHOO<sup>1</sup>, A. PANIGRAHI<sup>2</sup>, S.K. PATRI<sup>3</sup>, R.N.P. CHOUDHARY<sup>3\*</sup>

<sup>1</sup>Department of Physics, Betnoti College Betnoti, Mayurbhanj, Orissa, India

<sup>2</sup>Department of Physics, D.N. College, Itanagar, Arunachal Pradesh, India

<sup>3</sup>Department of Physics & Meteorology, IIT, Kharagpur, 721302, India

Modulus and impedance spectroscopy studies on barium strontium samarium vanadate ( $\text{Ba}_4\text{SrSmTi}_3\text{V}_7\text{O}_{30}$ ) were carried out, as functions of frequency (1 kHz–1 MHz) and temperature (31–500 °C). XRD analysis of  $\text{Ba}_4\text{SrSmTi}_3\text{V}_7\text{O}_{30}$  ceramic revealed the formation of single phase compound in an orthorhombic structure. The Cole–Cole plots showed a non-Debye type of dielectric relaxation. The dc and ac analyses of  $\text{Ba}_4\text{SrSmTi}_3\text{V}_7\text{O}_{30}$  reveal typical negative temperature coefficient of resistance (NTCR) behaviour. The electric modulus, which describes the dielectric relaxation of the compound, is fitted to the Kohlrausch exponential function. Modulus analysis suggests the existence of a hopping mechanism for the electrical transport processes of the material.

Keywords: *electrical properties; SEM; X-ray diffraction*

### 1. Introduction

Materials of tungsten bronze (TB) structure belong to an important family of dielectric materials. Extensive studies of some ferroelectric materials of the TB structural family exhibit the occurrence of high electric permittivity ( $\epsilon$ ) and low dielectric loss [1, 2] along with interesting ferroelectric, pyroelectric, piezoelectric, and nonlinear optical properties are useful for various devices such as transducers, actuators, capacitors, and ferroelectric random access memory devices [3–7]. Various ionic substitutions in TB structures play an important role in tailoring their physical properties [4–7]. A detailed literature survey shows that not much work has been reported on the said compound  $\text{Ba}_4\text{SrSmTi}_3\text{V}_7\text{O}_{30}$  (BSSTV). The dielectric and electrical (ac conductivity) properties of BSSTV have already been reported elsewhere [8]. The present paper summarizes the impedance properties of the BSSTV compound.

---

\*Corresponding author, e-mail: crnpfl@phy.iitkgp.ernet.in

## 2. Experimental

*Preparation of the material.* A polycrystalline sample of BSSTV was fabricated using a high temperature solid state reaction technique. High purity (99.9 %) powders of BaCO<sub>3</sub>, SrCO<sub>3</sub>, TiO<sub>2</sub>, Sm<sub>2</sub>O<sub>3</sub> (Sarabhai M. Chemicals Pvt. Ltd., India), and V<sub>2</sub>O<sub>5</sub> (Koch Light Ltd., England) in stoichiometric proportion were weighed and thoroughly ground in an agate mortar to obtain a homogeneous mixture, and then calcined at 950 °C for 12 h. The calcined powder was cold pressed into cylindrical pellets 10 mm in diameter and 1–2 mm thick under the pressure of  $5 \times 10^6$  N/m<sup>2</sup> using a hydraulic press. Polyvinyl alcohol (PVA) was used as a binder to reduce the brittleness of the pellets, which was burnt out during high temperature sintering. Then the pellets were sintered at 1000 °C for 12 h in an air atmosphere using an alumina crucible. The sintered pellets were polished with fine emery paper to make the surfaces flat and parallel. To study the electrical properties of the compound, the both flat surfaces of the pellets were electroded with air-drying conducting silver paste. After electroding, the pellets were dried at 150 °C for 4 h to remove moisture, if any, and then cooled to room temperature before taking any measurement.

*Characterization of the material.* X-ray diffraction (XRD) data were collected with a Rigaku X-ray powder diffractometer (model: Miniflex) in a wide range of the Bragg angles ( $20^\circ \leq 2\theta \leq 80^\circ$ ) with CuK<sub>α</sub> ( $\lambda = 1.5405$  Å). The surface morphology and energy dispersive X-ray spectra (quantitative elemental analysis) were recorded under a scanning electron microscope JEOL (model: JSM-5800F). The electrical properties (i.e., the impedance and modulus parameters) of BSSTV were studied using a computer-controlled LCR meter (PSM 1735, model: N 4L) in a wide frequency range (from 1 kHz to 1MHz) at the ac signal (amplitude) of 1 V, starting at room temperature (31 °C) and ranging up to 500 °C.

## 3. Results and discussion

### 3.1. Structural study

Sharp, single peaks of the XRD pattern (Fig. 1) confirmed the formation of a new compound. All the prominent peaks were indexed, and the lattice parameters were refined using the least-squares refinement subroutine of the computer program POWDMULT [9]. The best agreement between observed (obs) and calculated (cal) interplanar spacing ( $d$ ) was found in the orthorhombic crystal system. However, a few small peaks in the XRD pattern were identified. The refined lattice parameters of BSSTV are:  $a = 10.8212$  (14) Å,  $b = 8.4211$ (14) Å,  $c = 20.7605$ (14) Å (with the estimated standard deviation in parenthesis). The Scherrer equation [10] was used to calculate the crystallite/particle size of the sample. The average particle size of the material was found to be 21 nm.

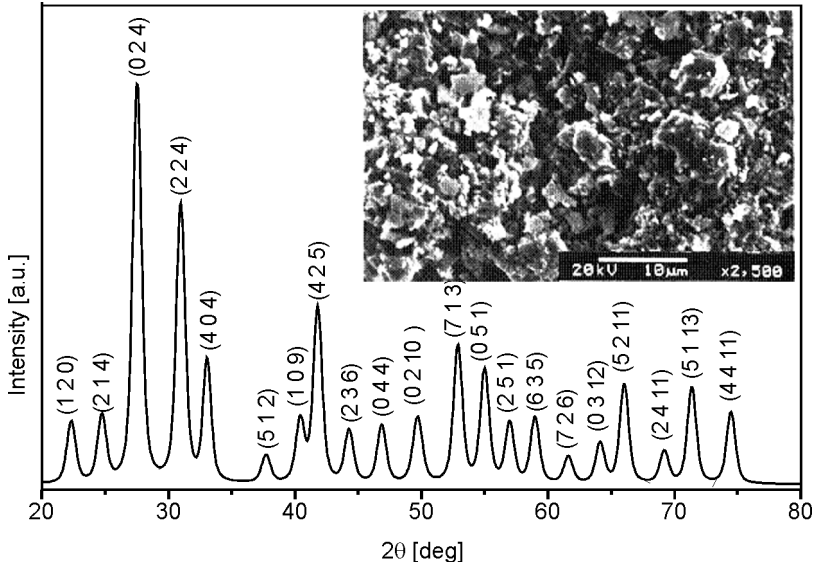


Fig. 1. Room temperature XRD pattern and SEM micrograph (inset) of  $Ba_4SrSmTi_3V_7O_{30}$

The inset of Figure 1 shows the scanning electron micrograph of the BSSTV pellet at room temperature. The micrograph revealed the presence of uniformly and densely distributed nearly-spherical grains with a certain degree of porosity. The grain size (diameter of individual grains of ceramics) of the compound was found to be in the range of 1.2–2.2  $\mu m$ . A similar type of microstructure was observed in many crystalline materials of this family [11–13].

### 3.2. Electrical analysis

The electrical behaviour of the system was studied over a wide range of frequencies and temperatures using an ac impedance spectrum (CIS) technique. The method enables us to separate real and imaginary components of the electrical parameters, and hence provides a true picture of the material properties. Using the CIS method, the grain and the grain boundary properties (having different time constants) of a polycrystalline material can usually be seen as two successive semicircles in the data representation.

#### 3.2.1. Impedance spectrum analysis

Figure 2 shows the Nyquist plots (complex impedance spectrum) of BSSTV at some selected temperatures (200–500  $^{\circ}C$ ). The spectrum is characterized by a single semicircular arc whose pattern of evolution changes upon increasing temperature which indicates the beginning of intergranular activities within the material sample with definite contributions from bulk (grain interior). In addition, the point of intercept

of the arcs on the real axis has also been observed to shift towards the origin of the complex plane plot. This type of shift suggests a decrease in the resistive behaviour of the sample, assisted by the grain boundary conduction upon increasing temperature [14]. Such electrical phenomena in the material can appropriately be modelled in terms of an equivalent  $rc$  electrical circuit. This observation clearly indicates that the electrical properties of this material are largely controlled by its microstructure.

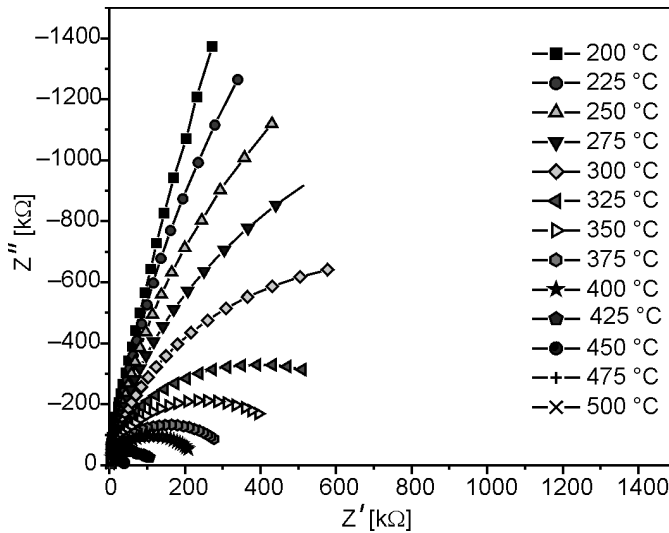


Fig. 2. Nyquist plot of  $\text{Ba}_4\text{SrSmTi}_3\text{V}_7\text{O}_{30}$

Figure 3a shows the dependence of the imaginary part of the impedance ( $Z''$ ) on the frequency (i.e., loss spectrum) at various temperatures (200–500 °C). The loss spectrum has some important features: (i) the appearance of a peak in the loss spectrum  $Z''_{\text{max}}$  ( $\geq 300$  °C), (ii) typical peak broadening, and (iii) value of  $Z''_{\text{max}}$  decreases and shifts to higher frequencies as temperature increases. The asymmetric peak broadening suggests a spread of the relaxation time (i.e., the existence of a temperature dependent electrical relaxation phenomenon in the material) [15]. The peak heights are proportional to the bulk resistance ( $R_b$ ), as expressed in the equation

$$Z'' = R_b \frac{\omega\tau}{1 + \omega^2\tau^2}$$

where  $\omega$  is angular frequency and  $\tau$  – relaxation time. The relaxation process in the material may be due to the presence of immobile species/electrons at low temperatures and defects/vacancies at high temperatures. Figure 3b shows the variation of the real part of the impedance  $Z'$  as a function of the frequency at various temperatures (200–500 °C) for  $\text{Ba}_4\text{SrSmTi}_3\text{V}_7\text{O}_{30}$ . It is observed that  $Z'$  decreases as temperature increases, indicating a negative temperature coefficient of the resistance in the system.

The plateau region of the plot also indicates the presence of a relaxation process in the material.

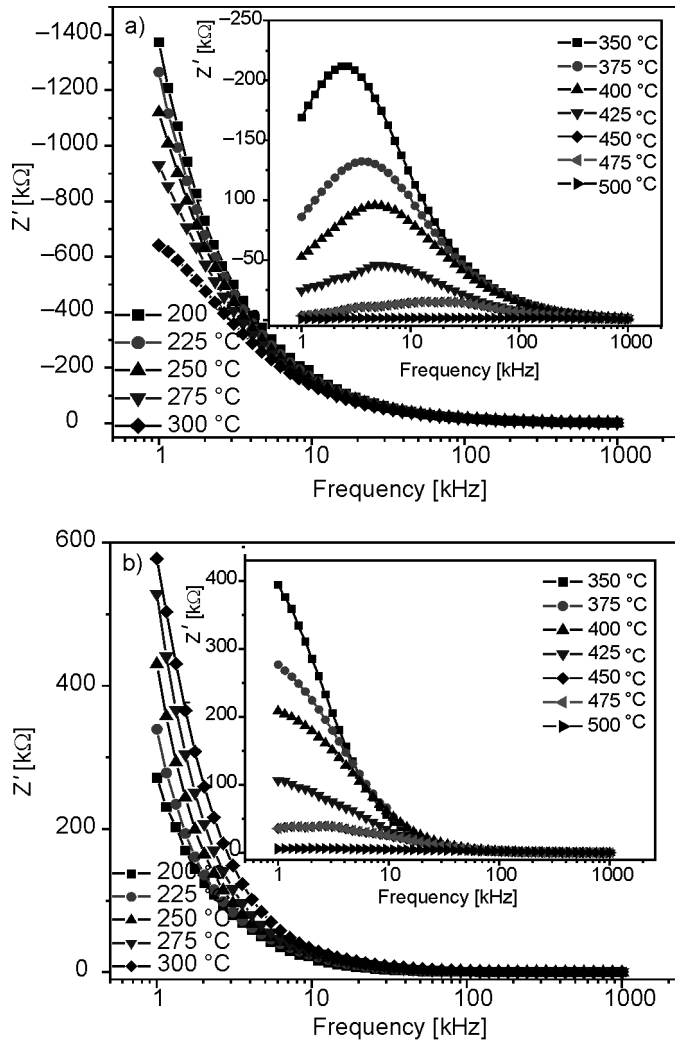


Fig. 3. Dependences of imaginary ( $Z''$ ) (a) and real ( $Z'$ ) (b) parts of complex impedance of  $Ba_4SrSmTi_3V_7O_{30}$  on the frequency

In the relaxation system, one can determine the most probable relaxation time ( $\tau$ ) from the position of the loss peak in the  $Z''$  or  $M''$  with frequency plots according to the dependence:  $\tau = 1/\omega = 1/2\pi f$ . The variation of relaxation time ( $\tau$ ) with the reciprocal temperature  $1/T$  ( $K^{-1}$ ) of BSSTV at high temperatures is shown in Fig. 4. The plot satisfies the Arrhenius equation,  $\tau = \tau_0 \exp(-E_a/K_B T)$ , where the symbols have their usual meaning. The relaxation time is related to the thermally activated process. The activation energy of the compound, calculated from the above equation, is found to be

0.58 eV (Fig. 4). Based on the modulus plot, the dependence of  $\tau$  on temperature is shown in the inset of Fig. 4. The value of the activation energy, obtained from the slope of the curve in the plot of  $\log\tau$  against  $10^3T^{-1}$ , is found to be  $\sim 0.64$  eV. It is clear that the activation energy of the compound (as calculated from the loss and modulus spectra) is nearly the same, and the relaxation process may be attributed to the same type of charge carrier.

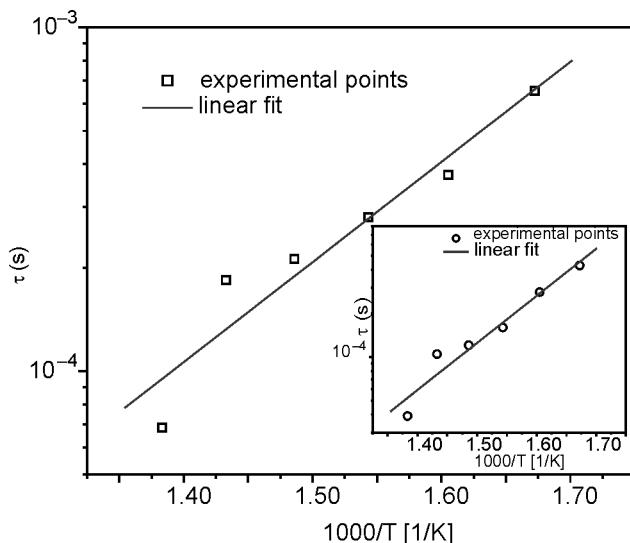


Fig. 4. Dependence of the relaxation time of  $\text{Ba}_4\text{SrSmTi}_3\text{V}_7\text{O}_{30}$  on  $1000/T$  calculated from the impedance spectrum ( $Z''$  vs. frequency) and modulus spectrum ( $M''$  vs. frequency) (inset)

### 3.2.2. Modulus spectrum analysis

In polycrystalline materials, the modulus of the impedance emphasizes the grain boundary conduction process, while bulk effects on frequency domain dominate in the electric modulus formalism. Modulus spectroscopy plots are particularly useful for separating spectral components of materials having similar resistances but different capacitances. The other advantage of the electric modulus formalism is that the electrode effect is suppressed. Due to the above reasons, complex electric modulus formalism has been opted. For the dielectric relaxation, studies have been carried out in the complex modulus  $M^*$  formalism. Variation of real ( $M'$ ) and imaginary ( $M''$ ) parts of the electric modulus in function of frequency at various temperatures are shown in Fig. 5.

It is evident from Fig. 5a that for each temperature,  $M'$  reaches a constant value at higher frequencies. Also, at lower frequencies  $M'$  approaches 0, confirming the presence of an appreciable electrode and/or ionic polarization at the studied temperature. The value of  $M'$  increases from a low frequency towards high frequency limit and the dispersion shifts to higher frequencies as temperature increases. The dependences of  $M''$  on frequency at various temperatures (Fig. 5b) reveals that as the frequency in-

creases,  $M''$  increases and attains a peak value at a particular frequency, for temperatures higher than 400 °C. The peak value of  $M''$  at 450 °C is much lower compared with the corresponding peak value at other temperatures, indicating the transition temperature of the sample is ca. 450 °C. Above 450 °C, the value of  $M''$  starts from the origin, increases proportionally with frequency, and attains a peak value at a particular frequency, and it subsequently decreases in inverse proportion to frequency. A similar trend has been found for all temperatures above 450 °C. However, at such temperatures, the peak values of  $M''$  shift towards the higher frequency range as temperature increases.

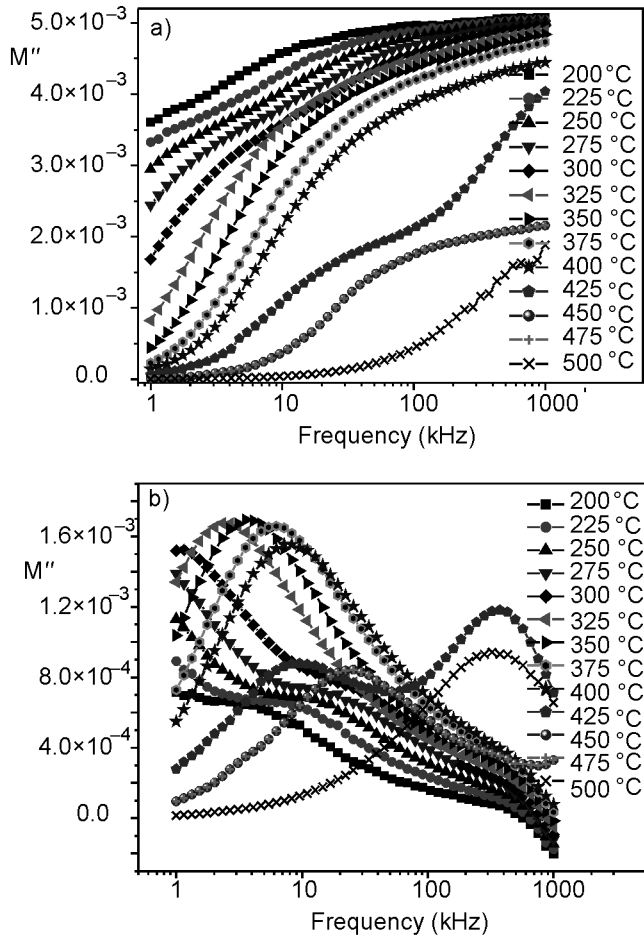


Fig. 5. Dependences of real (a) and imaginary (b) parts of the complex modulus ( $M'$  and  $M''$ ) of  $Ba_4SrSmTi_3V_7O_{30}$  on frequency

The complex modulus spectrum of BSSTV at higher temperatures (200–500 °C) is shown in Fig. 6. It is clear that the modulus plane shows two semicircles for tempera-

tures higher than 300 °C; the intercept of the first (smallest) semicircle with the real axis indicates the total capacitance contributed by the grain, while the intercept of the second semicircle indicates the total capacitance contributed by the grain boundary. The modulus spectrum shows a marked change in its shape upon increasing temperature, suggesting a change in the value of capacitance of the material with temperature.

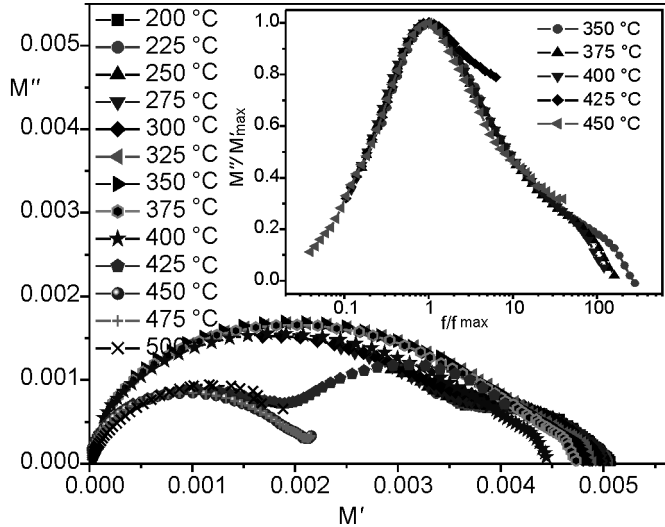


Fig. 6. Complex modulus spectrum ( $M''$  vs.  $M'$ ) at various temperatures and dependence of  $M''/M''_{\max}$  on  $f/f_{\max}$  (inset) of  $\text{Ba}_4\text{SrSmTi}_3\text{V}_7\text{O}_{30}$

The scaling behaviour of the sample was studied by plotting normalized parameters (i.e.,  $M''/M''_{\max}$  vs.  $\log(f/f_{\max})$ ,  $f_{\max}$  is the frequency corresponding to  $M''_{\max}$ ) at various temperatures (inset of Fig. 6). The coincidence of all the curves of different temperatures into a single master curve indicates temperature independent dynamic processes [16]. This curve provides us with information about dielectric processes occurring in the material and the magnitude of mismatch between the peaks.

### 3.2.3. Conductivity analysis

The temperature–frequency dependence of electrical conductivity can be represented by an equation proposed by Jonscher [17]:

$$\sigma_{ac} = \sigma_{dc} + A\omega^n$$

where  $\sigma_{dc}$  conductivity is due to the excitation of electrons from a localized state to the conduction band, and  $A\omega^n$  is the ac conductivity which consists of all dispersion phenomena.  $A$  is the frequency independent constant and  $n$  an exponent,  $0 < n < 1$ ; both of these terms are temperature dependent. Figure 7 shows the dependence of ac conduc-

tivity on frequency at various temperatures. The conductivity pattern shows that it is strongly frequency dependent and obeys Jonscher's power relation, as given above.

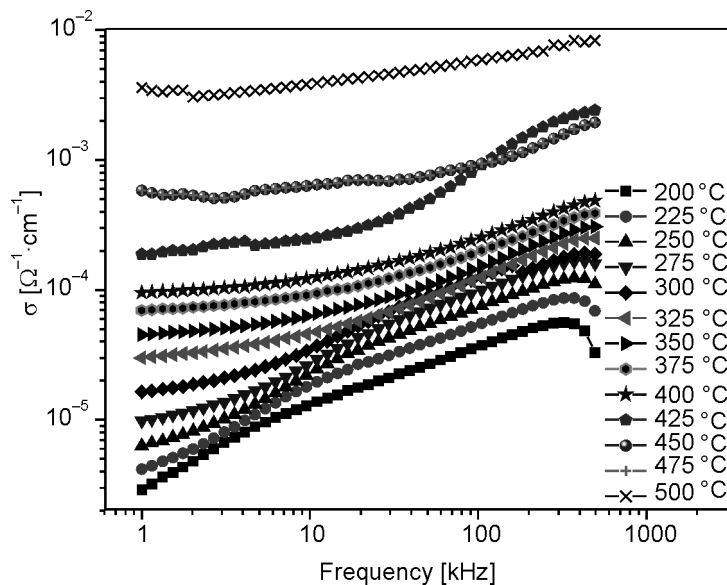


Fig. 7. Dependence of  $\sigma_{ac}$  of  $Ba_4SrSmTi_3V_7O_{30}$  on frequency

It clearly indicates that low and high frequency dispersive regions are separated by a change in slope at a particular frequency. The frequency at which a change in the slope occurs is called the hopping frequency.

#### 4. Conclusions

$Ba_4SrSmTi_3V_7O_{30}$  was prepared by the mixed-oxide method. Preliminary X-ray analysis shows that the compound has an orthorhombic crystal structure at room temperature. Impedance spectroscopy was used to characterize the electrical properties of the material. The bulk effect was observed above 300 °C. The complex impedance plots show that the bulk resistance decreases upon increasing temperature, indicating the negative temperature coefficient of resistance behaviour of the sample. Analysis of the frequency dependence of ac conductivity shows that ac resistance follows the universal power law, as suggested by Jonscher. The conduction mechanism of the material may be due to the hopping of charge carriers.

#### References

- [1] CHEN X.M., SUN Y.H., ZHENG X.H., J. Eur. Ceram. Soc., 23 (2003), 1571.
- [2] FANG L., CHEN L., ZHANG H., DIAO C.L., YUAN R.Z., Mater. Lett., 58 (2004), 2654.

- [3] NEURGAONKAR R.I., HALL W.F., OLIVER J.R., HO W.W., CORY W.K., *Ferroelectrics*, 87 (1998), 167.
- [4] NEURGAONKAR R.R., CORY W.K., *J. Opt. Soc. Am.*, 3 (1986), 276.
- [5] NEURGAONKAR R.R., NELSON J.G., OLIVER J.R., *Mater. Res. Bull.*, 25 (1990), 959.
- [6] PANIGRAHI A., SINGH N.K., *J. Mater. Sci. Lett.*, 18 (1999), 1579.
- [7] RAJU M.R., CHOUDHARY R.N.P., *J. Phys. Chem. Solids*, 64 (2003), 847.
- [8] SAHOO P.S., PANIGRAHI A., PATRI S.K., CHOUDHARY R.N.P., *Mat. Lett.*, 63 (2009), 864.
- [9] WU E., *POWD, An Interactive Powder Diffraction Data Interpretation and Indexing Program, Version 2.1*, School of Physical Sciences, Flinders Univ. of South Australia.
- [10] CULLITY B.D., *Elements of X-ray Diffraction*, Addison-Wesley Publishing Co. Inc., 1978.
- [11] BEHERA B., NAYAK P., CHOUDHARY R.N.P., *Mater. Lett.*, 59 (2005), 3489.
- [12] BEHERA B., NAYAK P., CHOUDHARY R. N. P., *Mater. Chem. Phys.*, 100 (2006), 138.
- [13] SAHOO P.S., PANIGRAHUA, PATRI S.K., CHOUDHARY R.N.P., *Mod. Phys. Lett., B*, 30 (2008), 2999.
- [14] MACDONALD J.R., *Impedance Spectroscopy Emphasizing Solid Materials and Systems*, Wiley, New York, 1987.
- [15] SCHERRER P., *Göttinger Nachrichten*, 2 (1918), 98.
- [16] SAHA S., SINHA T.P., *Phys. Rev. B*, 65 (2002), 134103.
- [17] JONSCHE A.K., *Nature* 267 (1977), 673.

*Received 21 September 2008*

*Revised 7 August 2009*

# Cycling behaviour of barium doped $\text{LiMn}_2\text{O}_4$ cathode materials for Li ion secondary batteries

H. SAHAN\*, H. GÖKTEPE, S. PATAT

Department of Chemistry, Faculty of Science, Erciyes University, 38039 Kayseri, Turkey

In order to improve the cycling performance of  $\text{LiMn}_2\text{O}_4$ , the spinel phase  $\text{LiMn}_{2-x}\text{Ba}_x\text{O}_4$  ( $x = 0.01, 0.02$  and  $0.05$ ) compounds were fabricated by the glycine-nitrate method. The structures of the products were investigated by X-ray diffraction. Electrochemical studies were carried out using the  $\text{Li}|\text{LiMn}_2\text{O}_4$  and  $\text{Li}|\text{LiMn}_{2-x}\text{Ba}_x\text{O}_4$  cells. The capacity loss of  $\text{Li}|\text{LiMn}_2\text{O}_4$  cell is about 15% after 30 cycles, whereas that for Ba doped spinel materials ( $x = 0.01, 0.02$  and  $0.05$ ) are 7.5%, 3.5% and 1.8% respectively. The good capacity retention of  $\text{LiMn}_{2-x}\text{Ba}_x\text{O}_4$  electrodes is attributed to stabilization of the spinel structure by Ba doping of Mn sites. Ba substituted spinels display better cycle performance in terms of cycle life compared with  $\text{LiMn}_2\text{O}_4$ .

Keywords:  $\text{LiMn}_2\text{O}_4$ ; glycine nitrate method; cycle life; Ba doping

## 1. Introduction

Increasing demand for portable electronic devices is driving the development of compact lightweight batteries of high energy density. Lithium secondary batteries show great promise as power sources for portable electronic devices such as cellular phones, camcorders and laptop computers because of their high output voltages, high specific energy densities, and excellent cycle performance [1]. Among the cathodic materials investigated,  $\text{LiMn}_2\text{O}_4$  based spinels are promising candidates for replacing  $\text{LiCoO}_2$ , which is the material currently used in commercial lithium batteries. Spinel  $\text{LiMn}_2\text{O}_4$  has been considered a potential alternative to  $\text{LiCoO}_2$  for use as the positive electrode in rechargeable lithium ion batteries because of its low cost, environmental friendliness and high safety [2–4]. However, stoichiometric  $\text{LiMn}_2\text{O}_4$  exhibits an unacceptably high capacity fade on cycling. The origin for this capacity loss has not been clearly identified, but several possibilities exist, e.g. (i) occurrence of lattice (Jahn–Teller) distortion on the surface of  $\text{LiMn}_2\text{O}_4$  due to inhomogeneity in discharge and formation of tetragonal  $\text{Li}_2\text{Mn}_2\text{O}_4$  [5],(ii) manganese dissolution into electrolyte [6],

---

\*Corresponding author, e-mail: halil@erciyes.edu.tr

(iii) formation of oxygen defects [7], (iv) formation of new phases [8], (v) loss of crystallinity [9], (vi) instability arising from the existence of two cubic phases during the charge–discharge process [10].

Among various approaches to overcome these problems, one effective approach is to substitute a small amount of Mn ions with dopant ions [11, 12]. It is believed that the dopant ions occupy 16d sites of Mn ions in the spinel lattice and stabilize the spinel structure. Research shows that suitable elements doping are good way of improving the properties of  $\text{LiMn}_2\text{O}_4$  cathode materials [13]. Extensive research studies on doping have hitherto focused on such elements as Na, Mg, Al, Zn, B, F, S, Co, Ti, Cr, Mn, Cd, Sn, Ga, Fe, etc. [14–17]. However, the atomic radii of all these elements are lower than or comparable to that of Mn.

In this work Ba was selected as the substitute material, because it has a larger atomic radius than Mn. Bare and Ba substituted materials were prepared by the rapid glycine-nitrate method (GNM) and wherein Mn was partially replaced with Ba ions, to improve the cycle performance of  $\text{LiMn}_2\text{O}_4$  spinel materials.

## 2. Experimental

$\text{LiMn}_2\text{O}_4$  and  $\text{LiMn}_{2-x}\text{Ba}_x\text{O}_4$  ( $x = 0.01, 0.02$  and  $0.05$ ) spinels were fabricated with stoichiometric amounts of raw  $\text{LiNO}_3$  (Riedel-de Haen),  $\text{Mn}(\text{CH}_3\text{COO})_2 \cdot 4\text{H}_2\text{O}$  (Sigma) and  $\text{Ba}(\text{NO}_3)_2$  (Surechem). The raw materials were dissolved in distilled water. Glycine (Merck) was added to the mixture either as a solid or as water solution. Its role was to serve both as a fuel for combustion and as a complexing agent to prevent inhomogeneous precipitation of individual components prior to combustion. Finally, nitric acid with the same concentration of acetate anions was added to the solution. The molar ratio of glycine to nitrate was 1:4. The solution was heated continuously without any previous thermal dehydration. Afterwards the solution became a transparent viscous gel which auto-ignited automatically, giving a voluminous, black, sponge-like ash product of combustion. The resulting ash was heated at  $800\text{ }^\circ\text{C}$  for 12 h.

Phase identification of the samples was carried out by the XRD analyses using a Bruker AXS D8 diffractometer with monochromatic  $\text{CuK}_\alpha$  radiation. The DiffracPlus and Win-Metric programs were used to obtain information about the crystal structures of the samples. In all cases, the XRD patterns could be indexed based on a cubic cell. The morphologies of the powders were observed using a scanning electron microscope (SEM, LEO 440) operated at 20 kV.

Electrochemical studies were performed using a cylindrical two-electrode teflon cell assembled in an argon-filled dry box and tested at room temperature. Fabrication of the electrodes was as follows. The cathode material consisted of 86 wt. % of active material, 9 wt. % of acetylene black was used as the conductive material and 5 wt. % of poly(tetrafluoroethylene) as a binder. A lithium piece 13 mm in diameter, 1 M  $\text{LiPF}_6$  solution in ethylene carbonate/diethyl carbonate (EC:DEC = 1:1) and a glass filter were used as the anode, electrolyte and separator, respectively.

Diethyl carbonate, ethylene carbonate, and acetylene black were used after purification by the methods described elsewhere [18]. 100 cm<sup>3</sup> of diethyl carbonate (DEC) was washed with aqueous 10%  $\text{Na}_2\text{CO}_3$  solution (20 cm<sup>3</sup>), saturated  $\text{CaCl}_2$  (20 cm<sup>3</sup>) and then with water (30 cm<sup>3</sup>). After drying over solid  $\text{CaCl}_2$  for 1 h (note that prolonged contact should be avoided because slow combination with  $\text{CaCl}_2$  occurs), it should be fractionally distilled. Ethylene carbonate was dried over  $\text{P}_2\text{O}_5$ , then fractionally distilled under the pressure of 10 mm Hg and crystallized from dry ethyl ether. Acetylene black was leached for 24 h with 1:1 HCl to remove oil contamination, then washed repeatedly with distilled water. Then it was dried in air, and eluted for 1 day each with benzene and acetone. Again it was dried in air at room temperature and then heated in vacuum for 24 h at 600 °C to remove adsorbed gases.

The test cell performance was measured on a computer controlled multi-channel charge/discharge apparatus (MLab100, Wenking). In order to study their cycling performance, the test cells were galvanostatically charged/discharged at a constant current rate of 1 C within the voltage range of between 3.5 V and 4.5 V (vs.  $\text{Li}/\text{Li}^+$ ).

### 3. Results and discussion

The powder X-ray diffraction patterns of the  $\text{LiMn}_2\text{O}_4$  and  $\text{LiMn}_{2-x}\text{Ba}_x\text{O}_4$  ( $x = 0.01, 0.02$  and  $0.05$ ) are shown in Fig. 1. The XRD spectra confirmed there were no phase differences between the Ba doped  $\text{LiMn}_2\text{O}_4$  spinel samples and pure, undoped  $\text{LiMn}_2\text{O}_4$  spinel samples (in particular, BaO phase was not present in the Ba doped  $\text{LiMn}_2\text{O}_4$  samples).

The powder X-ray diffraction patterns of the samples synthesised for this study could be indexed to the spinel space group ( $Fd\bar{3}m$ ) in which lithium ions occupy the tetrahedral (8a) sites.  $\text{Mn}^{3+}$  and  $\text{Mn}^{4+}$  ions as well as the doping metal ions, as in  $\text{LiMn}_2\text{O}_4$  structure, occupy the (16d) sites [19]. For simplicity, these structures can be expressed as  $[\text{Li}]_{\text{tetrahedral}}[\text{Mn}_{2-y}\text{M}_y]_{\text{octahedral}}[\text{O}_4]$  [20]. The ionic radius of six coordinate  $\text{Mn}^{4+}$  is 0.53 Å, but the ionic radius of six coordinate  $\text{Mn}^{3+}$  depends on the spin state. In the low spin state (LS) its ionic radius is 0.58 Å, but in the high spin state (HS) it is 0.645 Å. However, the ionic radius of sixth coordinate  $\text{Ba}^{2+}$  is 1.49 Å [21]. Therefore, the lattice parameter of substituted spinel should be higher than that of undoped spinel  $\text{LiMn}_2\text{O}_4$ .

Table 1. The cubic lattice parameter  $a$  and the unit cell volume  $V$  for  $\text{LiMn}_2\text{O}_4$  and  $\text{LiMn}_{2-x}\text{Ba}_x\text{O}_4$  ( $x = 0.01, 0.02$  and  $0.05$ ) samples

Compound	$a$ [Å]	$V$ [Å <sup>3</sup> ]
$\text{LiMn}_2\text{O}_4$	$8.24095 \pm 0.00163$	559.669
$\text{LiMn}_{1.99}\text{Ba}_{0.01}\text{O}_4$	$8.24150 \pm 0.00272$	559.781
$\text{LiMn}_{1.98}\text{Ba}_{0.02}\text{O}_4$	$8.23597 \pm 0.00163$	558.656
$\text{LiMn}_{1.95}\text{Ba}_{0.05}\text{O}_4$	$8.23846 \pm 0.00163$	559.162

On the contrary, as shown in Table 1, the cubic lattice parameters of Ba substituted spinels, as calculated with the Win-Metric program, were similar or lower than those of the unsubstituted compound. This may be explained by the fact that the value of  $\Delta_f G$  of BaO ( $-525 \text{ kJ}\cdot\text{mol}^{-1}$ ) is more negative than  $\Delta_f G$  of  $\text{MnO}_2$  ( $-465 \text{ kJ}\cdot\text{mol}^{-1}$ ). Thus, doped metal ions enhance the stability of the octahedral sites and decrease the lattice constant of a spinel skeleton structure because the bonding energy of the doped metal oxygen (Ba–O:  $548 \text{ kJ}\cdot\text{mol}^{-1}$ ) is stronger than that of Mn–O ( $402 \text{ kJ}\cdot\text{mol}^{-1}$ ) [22]. A similar result was also reported by Xu et al. [23].

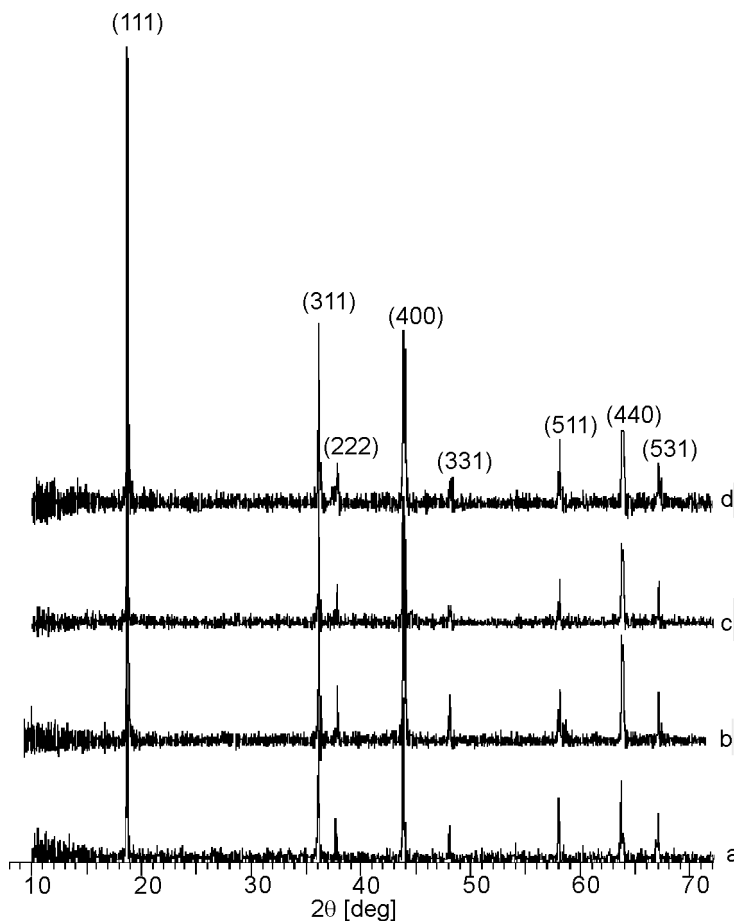


Fig. 1. X-ray diffraction patterns of: a)  $\text{LiMn}_2\text{O}_4$ , b)  $\text{LiMn}_{1.99}\text{Ba}_{0.01}\text{O}_4$ , c)  $\text{LiMn}_{1.98}\text{Ba}_{0.02}\text{O}_4$ , d)  $\text{LiMn}_{1.95}\text{Ba}_{0.05}\text{O}_4$  powders

Because the particle size and surface morphology are also important factors for the cycling performance of cathode materials, they were examined by SEM. Figure 2 shows the micrographs of  $\text{LiMn}_2\text{O}_4$  and  $\text{LiMn}_{2-x}\text{Ba}_x\text{O}_4$  ( $x = 0.01, 0.02$  and  $0.05$ ) powders. The average particle size of all samples was calculated by the Image Pro-Plus 5.0

program. The average particle sizes of the powders were slightly below 400 nm. The substituted spinel particles are not isolated, but are connected (cf. Figs. 2a–d). Consequently, the specific surface area of substituted spinel particles decreases. Matsuda et. al reported that the smaller the specific surface area of active material particles, the better the cycle performance of the cell is [24]. Thus we may expect the capacity fade of the  $\text{Li}|\text{LiMn}_{2-x}\text{Ba}_x\text{O}_4$  ( $x = 0.01, 0.02$  and  $0.05$ ) cell to be lower than that of the  $\text{Li}|\text{LiMn}_2\text{O}_4$  cell; large specific surface area of  $\text{LiMn}_2\text{O}_4$  particles promotes Mn dissolution into the electrolyte.

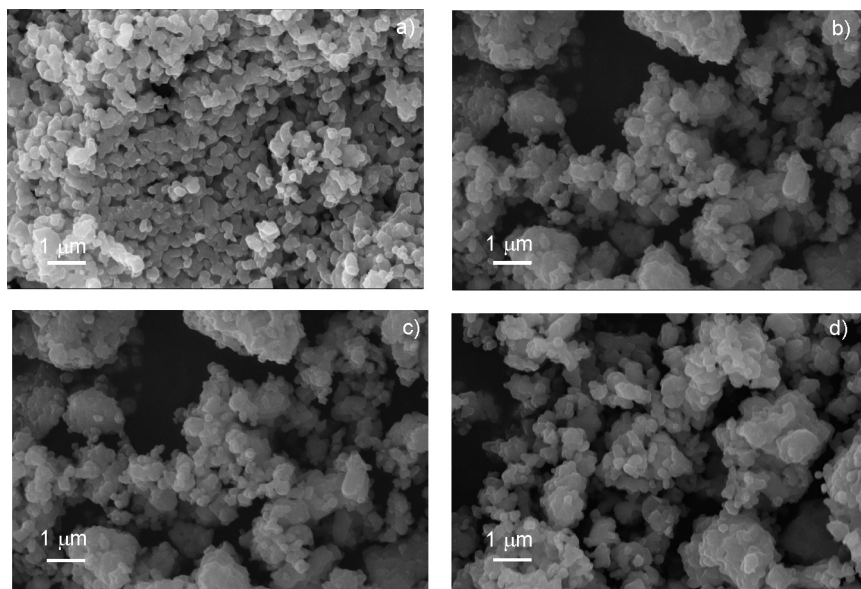


Fig. 2. Scanning electron micrographs of spinel powders:  $\text{LiMn}_2\text{O}_4$  (a),  $\text{LiMn}_{2-x}\text{Ba}_x\text{O}_4$ ,  $x = 0.01$  (b),  $x = 0.02$  (c) and  $x = 0.05$  (d)

Figure 3 shows the discharge profiles of  $\text{LiMn}_2\text{O}_4$  and  $\text{LiMn}_{2-x}\text{Ba}_x\text{O}_4$  ( $x = 0.01, 0.02$  and  $0.05$ ) cathodes for 1–30th cycles at room temperature. As can be clearly seen, the discharge curves of all samples had two plateaus at approximately 4.0 and 4.1 V, which indicates a remarkable characteristic of a well defined  $\text{LiMn}_2\text{O}_4$  spinel. The initial discharge capacity of the  $\text{Li}|\text{LiMn}_2\text{O}_4$ ,  $\text{Li}|\text{LiMn}_{2-x}\text{Ba}_x\text{O}_4$  ( $x = 0.01, 0.02$  and  $0.05$ ) cells reached 120.1, 115.2, 115.2 and 89.7  $\text{mAh}\cdot\text{g}^{-1}$ , respectively. This is due to the decreasing amount of  $\text{Mn}^{3+}$  ions in the substituted spinel phase, since during the intercalation–deintercalation of  $\text{Li}^+$  in  $\text{LiMn}_2\text{O}_4$  only the  $\text{Mn}^{3+}$  contributes to the charge capacity.

Dependences of the discharge capacity on the cycle number for all cathodes are shown in Fig. 4. The discharge capacity and capacity fading rates for various numbers of cycles were evaluated (Table 2). As is clearly seen, the cycle performance of the Ba doped  $\text{LiMn}_2\text{O}_4$  cathodes was a significant improvement over the undoped cathodes. After 30 cycles, the discharge capacity and capacity loss of undoped  $\text{LiMn}_2\text{O}_4$  was

101.7  $\text{mAh}\cdot\text{g}^{-1}$  and 15.1%, respectively. However, the discharge capacity of  $\text{LiBa}_{0.02}\text{Mn}_{1.98}\text{O}_4$  still kept 111.2  $\text{mAh}\cdot\text{g}^{-1}$  and capacity fading was only 3.5%, after 30 cycles. As shown in Fig. 4 and Table 2,  $\text{LiMn}_{1.99}\text{Ba}_{0.01}\text{O}_4$  and  $\text{LiMn}_{1.98}\text{Ba}_{0.02}\text{O}_4$  electrodes have the same initial discharge capacity but the discharge capacity fade of the  $\text{LiMn}_{1.99}\text{Ba}_{0.01}\text{O}_4$  electrode is higher than that of the  $\text{LiMn}_{1.98}\text{Ba}_{0.02}\text{O}_4$  electrode. Although initial discharge capacity fading of  $\text{LiMn}_{1.95}\text{Ba}_{0.05}\text{O}_4$  electrode is only 1.8% because the molar ratio of  $\text{Ba}^{2+}$  ions in the crystal lattice is increased, this electrode has the lowest initial discharge capacity. For these reasons, the electrode performance of  $\text{LiMn}_{1.98}\text{Ba}_{0.02}\text{O}_4$  is better than the others.

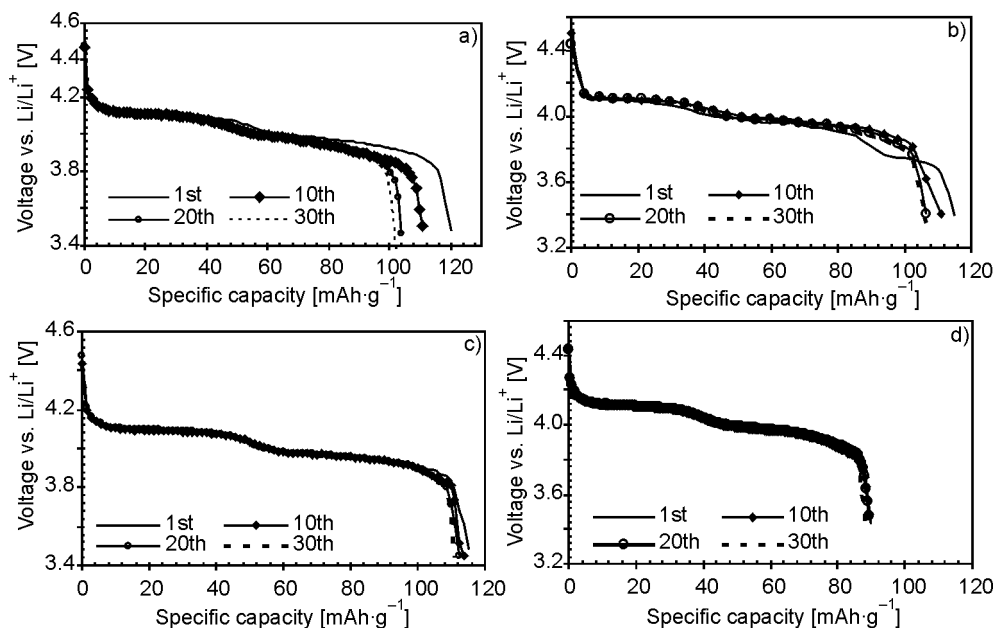


Fig. 3. Discharge profiles of the electrodes:  $\text{LiMn}_2\text{O}_4$  (a) and  $\text{LiMn}_{2-x}\text{Ba}_x\text{O}_4$ ;  $x = 0.01$  (b),  $x = 0.02$  (c),  $x = 0.05$  (d)

Table 2. Discharge capacity performance of the base  $\text{Li}|\text{LiMn}_2\text{O}_4$  and  $\text{Li}|\text{LiMn}_{2-x}\text{Ba}_x\text{O}_4$  ( $x = 0.01, 0.02$  and  $0.05$ ) cells

Cathode material	Discharge capacity ( $\text{mAh}\cdot\text{g}^{-1}$ )				Capacity fading [%]
	1st	10th	20th	30th	
$\text{LiMn}_2\text{O}_4$	120.1	111.1	104.0	101.7	15.3
$\text{LiMn}_{1.99}\text{Ba}_{0.01}\text{O}_4$	115.2	115.2	111.0	106.6	7.5
$\text{LiMn}_{1.98}\text{Ba}_{0.02}\text{O}_4$	115.2	114.0	112.6	111.2	3.5
$\text{LiMn}_{1.95}\text{Ba}_{0.05}\text{O}_4$	89.7	89.7	89.3	88.1	1.8

Because barium substitutes manganese in the lattice, the decrease of  $\text{Mn}^{3+}$  reduces the Jahn–Teller distortion and also stabilizes the structural integrity, improved electro-

chemical stability of  $\text{LiMn}_{2-x}\text{Ba}_x\text{O}_4$  ( $x = 0.01, 0.02$  and  $0.05$ ) electrodes is obtained. In addition, the bonding energy of Ba–O is higher than that of Mn–O. Thus the dopants enhance the stability of the spinel structure and prevent structural degradation of the material.

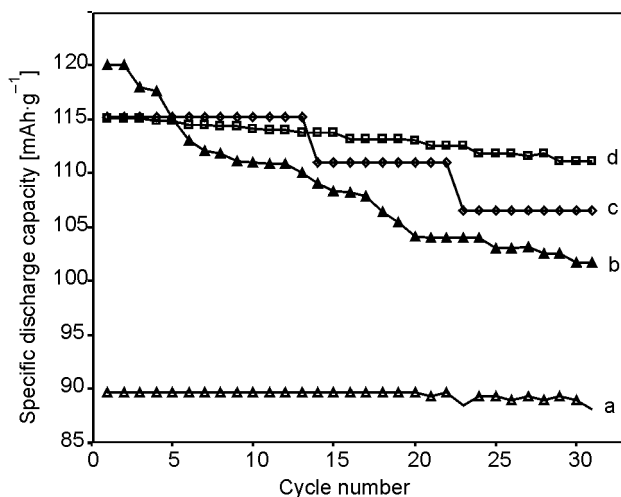


Fig. 4. Dependences of discharge capacity on the cycle number for the cells:  $\text{Li}|\text{LiMn}_2\text{O}_4$  (b) and  $\text{Li}|\text{LiMn}_{2-x}\text{Ba}_x\text{O}_4$ ;  $x = 0.01$  (c),  $x = 0.02$  (d) and  $x = 0.05$  (a)

As recent work has shown, Er and La doped  $\text{LiMn}_2\text{O}_4$  spinel has excellent cycling performance, and cell polarization decreased as the number of cycles increased [25, 26]. Thus, we assumed that Ba doping improves cathodic properties of  $\text{LiMn}_2\text{O}_4$  and ensures better electrochemical performance.

## 4. Conclusions

In this study,  $\text{LiMn}_2\text{O}_4$  and  $\text{LiMn}_{2-x}\text{Ba}_x\text{O}_4$  ( $x = 0.01, 0.02$  and  $0.05$ ) powders having spinel structure were synthesized by the glycine-nitrate method.  $\text{LiMn}_{2-x}\text{Ba}_x\text{O}_4$  ( $x = 0.01, 0.02$  and  $0.05$ ) cathode materials showed lower initial discharge capacity than unmodified  $\text{LiMn}_2\text{O}_4$ . Chemical substitution of Ba for Mn in  $\text{LiMn}_2\text{O}_4$  improves the cycling performance. The improvement in the cycling properties might be attributed to the stabilization of the spinel structure and the suppression of the Jahn–Teller distortion via Ba metal doping. Tu et al. confirmed that the charge transfer resistance is slowed down by La doping on  $\text{LiMn}_2\text{O}_4$  [26]. We may expect that the effect on charge transfer resistance of Ba doping is the same as La doping.

### Acknowledgements

This study was financially supported by the Research Foundation of Erciyes University (Kayseri, Turkey). The authors thank Mrs. F.Kılıç for the SEM observation.

## References

- [1] KIM J., MANHIRAM A., *Nature*, 390 (1997), 265.
- [2] SUN X., YANG X.O., BALASUBRAMANIAN M., MCBREEN J., XIA Y., SAKAI T., *J. Electrochem. Soc.*, 149 (2002), A842.
- [3] SAITOH M., SANO M., FUJITA M., SAKATA M., TAKATA M., NISHIBORI E., *J. Electrochem. Soc.*, 151 (2004), A17.
- [4] REIMERS J.N., DAHN R.J., *J. Electrochem. Soc.*, 151 (1992), 2091.
- [5] THACKERAY M.M., SHAOHORN Y., KAHAIAN A.J., KEPLER K.D., SKINNER E., VAUGHEY T., HACKNEY S.A., *Electrochem. Solid State Lett.*, 1 (1998), 7.
- [6] YAMANE H., INOUE T., SANO M., *J. Power Sources*, 99 (2001), 60.
- [7] WANG X., NAKAMURA H., YOSHIO H., *J. Power Sources*, 110 (2002), 19.
- [8] PALACIN M.R., CHABRE Y., DUPONT L., HERVIEU M., MASQUELIER C., *J. Electrochem. Soc.*, 47 (2000), 845.
- [9] HUANG H., VINCENT C.A., BRUCE P.G., *J. Electrochem. Soc.*, 146 (1999), 3649.
- [10] XIA Y., YOSHIO M., *J. Power Sources*, 66 (1997), 129.
- [11] EIN-ELI Y., VAUGHTY J.T., THACKERAY M.M., MUKERJEE S., YANG X.Q., MCBREEN J., *J. Electrochem. Soc.*, 146 (1999), 908.
- [12] HAYASHI N., IKUDA H., WAKIHARA M., *J. Electrochem. Soc.*, 146 (1999), 1351.
- [13] HWANG B.J., SANTHANAM R., HU S.G., *J. Power Sources*, 108 (2002), 250.
- [14] FU Y.P., SU Y.H., LI.C.H., *Solid State Ionics*, 166 (2004), 137.
- [15] TANIGUCHI I., *Mater. Chem. Phys.*, 92 (2005), 172.
- [16] SAHAN H., GÖKTEPE H., PATAT S., *Inorg. Mater.*, 44 (2008), 420.
- [17] LIU R.S., SHEN C.H., *Solid State Ionics*, 157 (2003), 95.
- [18] ARMAREGO W.L.F., PERIN D.D., *Purification of Laboratory Chemicals*, Heinemann, 4th Ed. Oxford, 2002.
- [19] GUOHUA L., IKUTA H., UCHIDA T., WAKIHARA M., *J. Electrochem. Soc.*, 143 (1996), 178.
- [20] WEST A.R., *Basic Solid State Chemistry*, Wiley, New York, 1991, p. 57.
- [21] SHANNON R.D., *Acta Cryst.*, A32 (1976), 751.
- [22] BREWER L., BRACKETT E., *Chem. Rev.*, 61 (1961), 425.
- [23] XU C.Q., LIU L.Y., *Mater. Chem. Phys.*, 98 (2006), 532.
- [24] MATSUDA K., TANIGUCHI I., *J. Power Sources*, 132 (2004), 156.
- [25] LIU H.W., ZHANG K.L., *Mater. Lett.*, 58 (2004), 3049.
- [26] TU J., ZHAO X.B., ZHUANG D.G., ZHU T.J., TU J.P., *Physica B*, (2006), 382.

*Received 19 March 2009*

*Revised 28 October 2010*

# A study of a block copolymer synthesized by RAFT polymerization containing carbazole groups and a europium complex

W. WANG<sup>1,2\*</sup>, Q.D. LING<sup>2</sup>, M.J. LIN<sup>1</sup>, Q.H. CHEN<sup>1</sup>

<sup>1</sup>College of Chemistry and Material Science, Fujian Normal University, Fuzhou 350007, P.R. China

<sup>2</sup>Fujian Key Laboratory of Polymer Materials, Fujian Normal University, Fuzhou 350007, P.R. China

A series of block copolymers containing carbazole groups were synthesized via reversible addition fragmentation chain transfer (RAFT) polymerization of styrene monomer. Then the block copolymer containing carbazole groups and europium complex was synthesized by coordination. The block copolymers were characterized by elemental analyses, FT-IR, <sup>1</sup>HNMR, GPC, Uv-vis absorption, fluorescence spectroscopy and cyclic voltammetry. The GPC result shows that the block copolymers have narrow polydispersity and controlled molecular weights (MWs). The fluorescence spectroscopy of the block copolymer containing carbazole groups and europium complex shows red emission assigned to f-f transitions of europium ions in solid state. In addition, the presence of europium complex in the block copolymer was further evidenced by fluorescence characteristic of europium ions. The CV data reveals that in the block copolymer containing carbazole groups and the europium complex a balance can be achieved between electron currents and the electron-hole currents. Thus, the copolymer is a potentially useful candidate for fabricating memory or light emitting devices.

Keywords: *reversible addition; fragmentation chain transfer; controlled polymerization; block copolymer; europium complex*

## 1. Introduction

Carbazole based compounds are attractive as photoconductors or charge transporting materials due to their relatively high charge carrier mobilities, hole transporting capability, high thermal and photochemical stability, and electroluminescent properties [1–3]. Rare earth compounds are excellent chromophores exhibiting intense fluorescence with a narrow spectral bandwidth and relatively long lifetime ( $10^{-2}$ – $10^{-6}$  s) [4]. They are the most widely used materials in CRT (cathode ray tube) displays and OLEDs (organic light emitting devices) [5]. Recently, flash (rewritable) and WORM

---

\*Corresponding author, e-mail: polywangwen@yahoo.com.cn

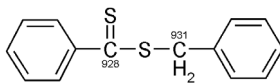
(write once read many times) memories with on carbazole and Eu complex based polymers were demonstrated [6, 7]. In these polymers, the carbazole groups served as electron donors and the hole transporting moieties, and the Eu complex, which was known to exhibit memory effects, was used to hold the charges. Among them, they were synthesized from the corresponding methacrylate or vinyl monomer by free-radical polymerization with 2,2'-azobis(isobutyronitrile) (AIBN) as the initiator. However, it is difficult to control the molecular weights (MWs) and their architectures because most of these polymers with pendant carbazole groups and Eu complexes were synthesized by conventional radical polymerization. The intrinsic wide polydispersity and the difficulty in purifying polymers possibly affect the performance of diode devices. It is desirable to establish new synthetic methods to control MWs, polydispersities, topologies and compositions to manifest their unique properties.

Controlled/living radical polymerization combines the virtues of living polymerization with the versatility and convenience of free radical polymerization. Among all the controlled/living radical polymerizations, RAFT can be considered one of the most promising methods as it allows controlling the homopolymerization of a great variety of monomers such as styrenes, acrylates, methacrylates and vinyl esters [8–12]. RAFT technique has also been successfully applied for controlled polymerization of methacrylate derivatives with carbazole or oxadizole as pendant groups [13].

In this study, the block copolymer containing carbazole groups with controlled MWs and narrow polydispersity were synthesized via RAFT polymerization of styrene monomers. The europium complex which was known to exhibit memory and luminescence properties was synthesized. Then the block copolymer containing carbazole groups and europium complex was synthesized by coordination with europium ion linkage  $\pi$  electron of benzene ring of the block copolymer. By this method, the block copolymer containing carbazole groups and europium complex which had predictable MW and low polydispersity was obtained. Such material has potential use in the fabrication of memories or light emitting devices.

## 2. Experimental

*Material.* All chemicals were obtained commercially and used without further purification unless other-wise noted. Benzene was washed with concentrated sulfuric acid for several times, and then washed with water, aqueous solution of  $\text{Na}_2\text{CO}_3$  (10 wt. %) and water, dried over anhydrous  $\text{CaCl}_2$ , distilled, and preserved over sodium before use. Toluene was refluxed over sodium in the presence of benzophenone until a persistent blue color appeared and then distilled prior to use. 2,2'-azobis(isobutyronitrile) (AIBN) was purified by recrystallization from ethanol. Chain transfer agent, benzyl dithiobenzoate (BDB) was synthesized according to the procedure reported in the literature [14]. The product was purified by the column chromatography on silica with petroleum ether as the eluent to afford BDB as a purple solid (Scheme 1).



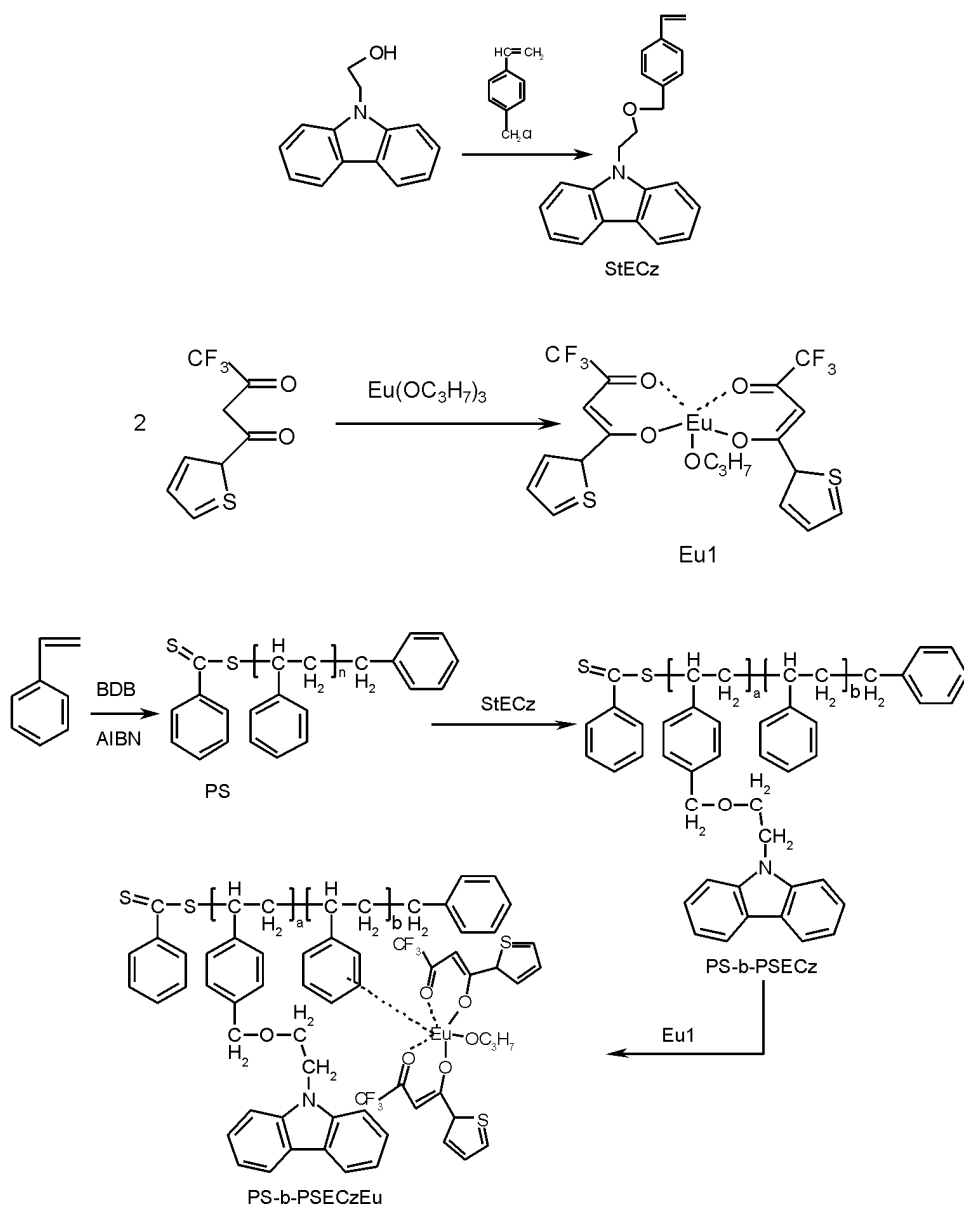
Scheme 1. Chemical structures of the BDB

*Instrumentation.*  $^1\text{H}$ NMR measurements were conducted with a Bruker ACF 300 spectrometer in  $\text{CDCl}_3$  or  $\text{CD}_3\text{OD}$  with tetramethylsilane (TMS) as an internal standard. Infrared (IR) spectra of the compounds in KBr pellets were recorded on a Nicolet 5700FT-IR spectrophotometer. Gel permeation chromatography (GPC) analyses were conducted with a Shimadzu LC-10AD vp using standard polystyrene samples as the MW references and tetrahydrofuran (THF) as the eluent at the flow rate of  $1.0 \text{ cm}^3/\text{min}$ . UV-vis absorption spectra were obtained using a Shimadzu UV 3150 UV-vis spectrometer. Fluorescence spectra were recorded using Edinburgh F900 spectrofluorometer. Elemental microanalyses (for C, H and N) were performed on a Perkin-Elmer 2400 elemental analyser. Eu content was determined by EDTA titration after polymer were decomposed by concentrated  $\text{HNO}_3/\text{HClO}_4$  (1:1, v/v). Cyclic voltammetry (CV) measurements were performed on an Autolab potentiostat/galvanostat system using a three electrode cell under argon atmosphere. The polymer films on a Pt disk electrode (working electrode) were scanned anodically and cathodically in a solution of tetrabutylammonium hexafluorophosphate ( $n\text{-Bu}_4\text{NPF}_6$ ) in acetonitrile (0.1 M) with  $\text{Ag}/\text{AgCl}$  and a platinum wire as the reference and counter electrodes, respectively.

*Synthesis of monomers and the block copolymers. Synthesis of the monomer 2-(9H-carbazol-9-yl) methyl styrene (StECz).* A dimethyl sulphoxide solution of NaOH and  $\text{H}_2\text{O}$  was added to the mixture of 2-(9H-carbazol-9-yl) ethanol (2.11 g, 10 mmol), a small quantity of NaI and tetrabutylammonium bromide. The mixture was stirred for 2 h at  $50 \text{ }^\circ\text{C}$ , then chloromethyl styrene was added dropwise to the mixture. The reaction mixture was stirred for 4 h at  $50 \text{ }^\circ\text{C}$ . The salt was removed by extraction with dichloromethane and water and the solvent was removed by evaporation. The yellow residue was purified by silica gel column chromatography using petroleum and ethyl acetate as an eluent, and further purified by recrystallization in petroleum. Yield: 80% (2.60 g). Anal. Calcd for  $\text{C}_{23}\text{H}_{21}\text{NO}$  (wt. %): C, 84.37; H, 6.46; N, 4.28. Found: C, 84.00; H, 6.70; N, 4.12. IR (KBr,  $\text{cm}^{-1}$ ): 3047.0, 2939.0, 2877.1, 2850.3, 1652.7 ( $\nu_{\text{C}=\text{C}}$ ), 1592.9, 1483.0, 1457.9, 1041.3, 748.2, 719.3 (carbazole ring).  $^1\text{H}$ NMR ( $\text{CDCl}_3$ , 300 MHz):  $\delta$ (ppm): 3.86(2H, s,  $-\text{CH}_2\text{N}-$ ), 4.00(2H, s,  $-\text{CH}_2-$ ), 4.51(2H, s,  $-\text{OCH}_2-$ ), 5.21 (1H, d, C = C), 5.71(2H, d, C = C), 7.09~8.10 (the H of carbazole and benzene ring) (Scheme 2).

*Synthesis of the europium complex (Eu1).* Europium trisopropoxide (3 mmol) was dissolved in  $15 \text{ cm}^3$  of anhydrous 2-propanol and toluene (1:1, V/V) by heating in a flask under nitrogen atmosphere. A solution of thenoyltrifluoroacetone (1.44 g, 6 mmol) in  $5 \text{ cm}^3$  toluene was added dropwise into the flask. The reaction mixture was

refluxed for 2 h and cooled. The excess solvent was evaporated and a yellow solid was obtained. Yield: 80% (2.0 g). Eu content for  $\text{EuC}_{19}\text{H}_{15}\text{O}_5\text{S}_2\text{F}_6$  (wt. %): 22.6%. Found: 23.3%. FT-IR (KBr pellet,  $\text{cm}^{-1}$ ): 3110, 2921( $\nu_{\text{C-H}}$ ), 1611( $\nu_{\text{C=O}}$ ), 1541( $\nu_{\text{C=C(THA)}}$ ), 1455, 1412, 1306( $\nu_{\text{C-F}}$ ), 1142, 787, 644( $\nu_{\text{C-CF}_3}$ ), 581, 463( $\nu_{\text{Eu-O}}$ ).  $^1\text{H NMR}$  ( $\text{CD}_3\text{OD}$ , 300 MHz):  $\delta$  (ppm): 1.53(6H, s, 2 $\text{CH}_3$ ), 2.73(H, s, CH), 3.50(2H, s, 2 $\text{COCHCO}$ ), 7.36–8.51(6H, m, 2 $\text{C}_4\text{H}_3\text{S}$ )



Scheme 2. Synthetic routes of the monomer and polymer

*RAFT polymerization of styrene.* All polymerizations were carried out in Schlenk tubes at homogeneous conditions. For a typical polymerization, styrene (8.72 mmol), BDB ( $4.4 \times 10^{-2}$  mmol), AIBN ( $1.4 \times 10^{-2}$  mmol) and dry benzene ( $0.5 \text{ cm}^3$ ) were placed in a dry Schlenk tube equipped with a magnetic stirrer bar. Then the solution was thoroughly deoxygenated by three freeze–pump–thaw cycles, backfilled with nitrogen, and the polymerization was conducted at  $70 \text{ }^\circ\text{C}$  for 24 h. The reaction mixture was precipitated in an excess of methanol, collected by filtration, and dried under vacuum to yield (PS) as pink powder. (Scheme 1) The monomer conversion was measured by the gravimetric method. The resulting powder was analyzed by GPC and had number average molar mass  $M_n = 0.6 \times 10^4$ ,  $M_w = 0.7 \times 10^4$  ( $M_w$  is weight average molar mass) and polydispersity index  $PDI = M_w/M_n = 1.13$ .

*The RAFT copolymerization using PS as macro-RAFT agent.* All copolymerizations were carried out in Schlenk tubes at homogeneous conditions. For a typical polymerization, 2-(9H-carbazol-9-yl) methyl styrene (StECz) (0.5 mmol), PS ( $M_n = 0.6 \times 10^4$ ,  $PDI = 1.13$ ) ( $12.5 \times 10^{-2}$  mmol), AIBN ( $3.75 \times 10^{-2}$  mmol) were placed in a dry Schlenk tube equipped with a magnetic stirrer bar. Then the polymerization was carried out in a similar way as described above. The resulting copolymer PS-*b*-PStECz was analyzed by GPC and had  $M_n = 1.03 \times 10^4$ ,  $M_w = 1.18 \times 10^4$ ,  $PDI (M_w/M_n) = 1.15$ .  $^1\text{H NMR}$  ( $\text{CDCl}_3$ , 300 MHz):  $\delta(\text{ppm})$ : 3.87(2H, s,  $-\text{CH}_2\text{N}-$ ), 4.20(2H, s,  $-\text{CH}_2-$ ), 4.53(2H, s,  $-\text{OCH}_2-$ ), 5.22(1H, d,  $-\text{C}$  (bonded benzene ring) H-C), 5.73(2H, d,  $-\text{C}-\text{CH}-$ ), 7.08–8.11 (H of carbazole and benzene ring).

*Preparation of the block copolymer containing carbazole groups and Eu complex (PS-*b*-PSECzEu).* PS-*b*-PSECz (0.5 mmol) ( $M_n = 1.03 \times 10^4$ ,  $M_w = 1.18 \times 10^4$ ,  $PDI = 1.15$ ), the europium complex (Eu1) ( $2.5 \times 10^{-2}$  mmol) and dry benzene ( $0.5 \text{ cm}^3$ ) were placed in a dry Schlenk tube equipped with a magnetic stirrer bar. Then the mixture was heated at  $70 \text{ }^\circ\text{C}$  for 24 h. The reaction mixture was precipitated in an excess of methanol, collected by filtration, and dried under vacuum to yield as yellow powder. The resulting powder was analyzed by GPC and had  $M_n = 1.03 \times 10^4$ ,  $M_w = 1.43 \times 10^4$ ,  $PDI = 1.39$ .  $^1\text{H NMR}$  ( $\text{CDCl}_3$ , 300 MHz):  $\delta(\text{ppm})$ : 1.56(6H, s, 2CH<sub>3</sub>), 3.87(2H, s,  $-\text{CH}_2\text{N}-$ ), 4.20(2H, s,  $-\text{CH}_2-$ ), 4.53(2H, s,  $-\text{OCH}_2-$ ), 5.22(1H, d,  $-\text{C}$  (bonded benzene ring) H-C), 5.73(2H, d,  $-\text{C}-\text{CH}-$ ), 7.08–8.11 (the H of carbazole and benzene ring). The Eu content was 2.57% (wt. %).

### 3. Results and discussion

#### 3.1. Living characters of the polymerization

In the RAFT copolymerization for the St-*b*-StECz system, styrene was the first monomer form the macro-RAFT agent. 2-(9H-carbazol-9-yl) methyl styrene (StECz) served as the second monomer.

A successful RAFT polymerization requires careful selection of a suitable CTA, depending upon the monomer. Benzyl dithiobenzoate (BDB) was selected as the CTA because BDB is an excellent CTA for RAFT polymerization of styrene monomers [15]. The homo-polymerizations of styrene were carried out in benzene at 70 °C using BDB as the chain transfer agent (CTA) and AIBN as an initiator under various conditions. In Table 1, details on syntheses of polystyrenes have been presented.

Table 1. Molecular weights and polydispersity indexes of polystyrene prepared in various conditions

Monomer – St [10 <sup>3</sup> M]	CTA–BDB [10 <sup>5</sup> M]	<i>t</i> [h]	AIBN [10 <sup>5</sup> M]	<i>M<sub>n</sub></i> ×10 <sup>-4</sup>	<i>M<sub>w</sub></i> ×10 <sup>-4</sup>	<i>PDI</i> ( <i>M<sub>w</sub></i> / <i>M<sub>n</sub></i> )	<i>M<sub>n, theor.</sub></i> ×10 <sup>-4</sup>	Conv. [%]
8.72	0	24	0.8	6.71	16.9	2.51		77.8
	4.4	24	2.2	0.92	1.16	1.26	0.85	40.9
	4.4	24	1.4	0.63	0.71	1.13	0.69	32.1
	2.2	24	1.1	1.12	1.34	1.20	1.46	35.2
	2.2	24	0.7	1.40	1.74	1.24	1.60	37.8

The theoretical number-average MW ( $M_{n, \text{theor.}}$ ) was calculated from monomer conversion according to Eq. (1) [16]:

$$M_{n, \text{theor.}} = \frac{[\text{monomer}]_0}{[\text{CTA}]_0} M_{\text{monomer}} \times \text{Conv} + M_{\text{CTA}} \quad (1)$$

where  $M_{\text{monomer}}$  and  $M_{\text{CTA}}$  are the molecular weights (MWs) of monomers and CTA, and  $[\text{monomer}]_0$  and  $[\text{CTA}]_0$  are the initial concentrations of monomer and CTA, respectively.

The GPC-determined number average MWs are roughly comparable to the theoretical values ( $M_{n, \text{theor.}}$ ), calculated from the monomer/CTA molar ratio and conversion of the monomer using Eq. (1). The polydispersity index (*PDI*) of the resulting polystyrene was lower than 1.3 which demonstrates that the RAFT polymerization system of styrene was well controlled.

The polystyrene ( $M_n = 0.6 \times 10^4$ ,  $M_w/M_n = 1.13$ ) obtained from the RAFT polymerization was chosen as the macro RAFT agent, AIBN as the initiator and 2-(9H-carbazol-9-yl) methyl styrene (StECz) as the second monomer. The block copolymerizations were carried out in benzene at 70 °C under various conditions, respectively. Table 2 shows the summary of the conditions and results.

In an ideal case, the theoretical  $M_{n, \text{theor}}$  of the block copolymer is calculated according to Eq. (2) [17]:

$$M_{n, \text{theor.}} = \frac{[\text{monomer}]_0}{[\text{polymer CTA}]_0} M_{\text{monomer}} \text{Conv} + M_{\text{polymer-CTA}} \quad (2)$$

where  $M_{\text{polymer-CTA}}$  is MWs of the first block (polystyrene from the RAFT polymerization),  $M_{\text{monomer}}$  is MWs of the second block (second monomer), Conv is the fractional conversion of the second monomer, and  $[\text{monomer}]_0$  and  $[\text{polymer CTA}]_0$  are the initial concentrations of monomer and polymer CTA, respectively.

Table 2. Molecular weights and polydispersity indexes of PS-*b*-PSECz copolymers in various conditions

Monomer [ $10^{-3}$ mol]	PS [ $10^{-5}$ mol]	<i>t</i> [h]	AIBN [ $10^{-5}$ mol]	$M_n$ $\times 10^4$	$M_w$ $\times 10^4$	<i>PDI</i> $M_w/M_n$	$M_n$ theor. $\times 10^4$	Conv. [%]
0.5	8.33	24	2.50	1.17	1.38	1.18	0.86	19.1
	12.5		3.75	1.03	1.18	1.15	0.93	24.5
	25		7.50	0.72	0.91	1.27	0.84	35.1
	12.5		6.25	0.91	1.11	1.22	0.96	26.8

As shown in Table 2, when the ratio of [monomer]: [polymer CTA]: [AIBN] = 40:1:0.3, the polydispersity index *PDI* of the resulting block copolymer is narrow (<1.15) and the MW is close to that calculated from Eq. (2).

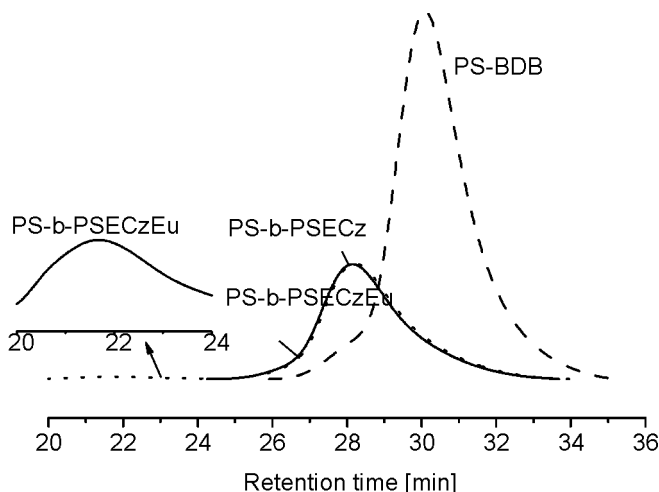


Fig. 1. GPC curves of PS-*b*-PSECz, PS-*b*-PSECzEu and polystyrene; dashed line – PS made from RAFT polymerization ( $M_n = 0.6 \times 10^4$ , *PDI* = 1.13), dotted line: PS-*b*-PSECz ( $M_n = 1.03 \times 10^4$ , *PDI* = 1.15), solid line: PS-*b*-PSECzEu ( $M_n = 1.03 \times 10^4$ , *PDI* = 1.39).

The inset is the the GPC curve of PS-*b*-PSECzEu for higher molecular weights

The GPC curves of the block copolymers and polystyrene made from RAFT polymerization are shown in Fig. 1. There is an obvious peak shift from the macro-RAFT agent (PS-BDB) to the block copolymer (PS-*b*-PSECz). The peak for macro-RAFT agent (PS-BDB) almost disappeared. In addition, the *PDI* values of these two polymers are similar. These demonstrate that the macro-RAFT agent was successfully

extended to block copolymer and PS-*b*-PSECz block copolymer was successfully produced through RAFT polymerization.

In comparison, the curve for PS-*b*-PSECzEu similar to the curve for PS-*b*-PSECz, had a shoulder in the higher molecular weight range (shown in the inset), which resulted in the broader *PDI* range (from 1.15 to 1.39). This indicates introducing europium complex to the block copolymer containing carbazole. The europium complex does not change the molecular weight of the PS-*b*-PSECz due to its low content (ca. 2.57%) and small molecular weight. The coupling of europium and  $\pi$  electrons of the benzene ring results in partial cross-linking in PS-*b*-PSECz-Eu. Thus, a higher molecular weight peak appears, and the *PDI* becomes higher. However, in previous studies, the polymers containing europium complex have higher *PDI* (*PDI* > 1.6) through the conventional radical polymerization [6, 7, 18]. We have successfully obtained a block copolymer containing carbazole groups and europium complex for which the the *PDI* is narrow, and it has a controlled molecular weight, through RAFT polymerization.

### 3.2. FT-IR analysis

The FT-IR spectrum of PS-*b*-PSECz shows characteristic absorption bands at 3050-2900  $\text{cm}^{-1}$  (Fig. 2) characteristic of C-H stretching vibrations of carbazole and

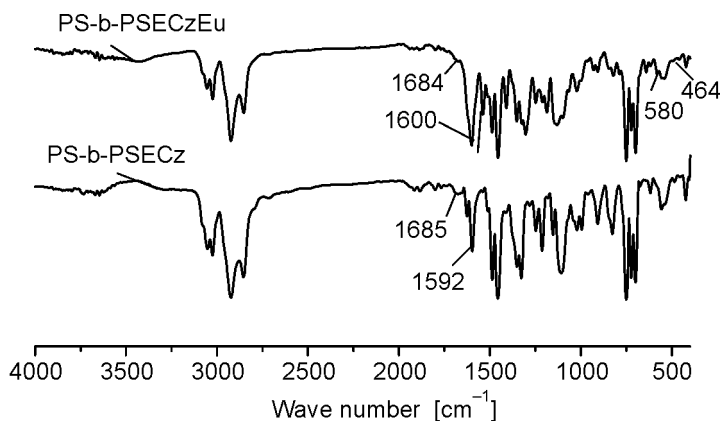


Fig. 2. FT-IR spectra of PS-*b*-PSECz and PS-*b*-PSECzEu

benzene rings. The absorption peaks at 1460  $\text{cm}^{-1}$ , 1489  $\text{cm}^{-1}$  and 1592  $\text{cm}^{-1}$  are assigned to skeleton stretching vibrations of the benzene ring. The peaks at 755 and 724  $\text{cm}^{-1}$  are assigned to vibrations of the carbazole group. However, the peak at 1685  $\text{cm}^{-1}$ , which is assigned to the stretching vibrations of S=C=S, appears in the spectrum of PS-*b*-PSECz indicating that the chain transfer agent was introduced to the end chain of the copolymer by the RAFT polymerization. The spectrum of PS-*b*-PSECzEu is similar to that of PS-*b*-PSECz, the band at 1600–1550  $\text{cm}^{-1}$  becomes

broader and red shifted because the coupling of europium and the  $\pi$  electrons of the benzene ring changes the electron density of the benzene ring. Two absorption peaks at 580 and 464  $\text{cm}^{-1}$ , associated with the Eu–O stretching vibrations [19], are also evident. Due to low content of europium complex in PS-b-PSECzEu, the absorption peaks associated with the ligands are buried under those of other aromatic species.

### 3.3. Optical properties

Optical properties of PS-b-PSECz and PS-b-PSECzEu were examined by UV absorption in dilute THF solutions and photoluminescence in solid state. As shown in Fig. 3, there is no significant difference in the spectrum of PS-b-PSECz and PS-b-PSECzEu. Three peaks at 299, 325 and 344 nm have observed, attributed to  $\pi \rightarrow \pi^*$  transitions of benzene and carbazole ring. The intensity of UV absorption bands in PS-b-PSECzEu is stronger than that in PS-b-PSECz. This indicates that the conjugated intensity of the copolymer containing the europium complex increases with the introduction to the europium.

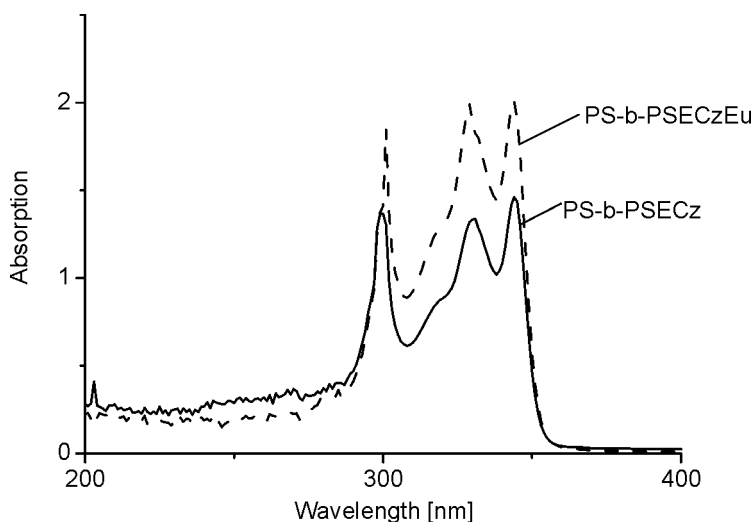


Fig. 3. UV absorption of PS-b-PSECz and PS-b-PSECzEu

Fluorescence spectra of PS-b-PSECz and PS-b-PSECzEu in solid state are shown in Fig. 4. In the excitation spectrum of PS-b-PSECz, excitation peaks appear at 383 nm and 400 nm and are attributed to the  $\pi \rightarrow \pi^*$  transitions of benzene and the carbazole ring, respectively. In the emission spectrum of PS-b-PSECz, two emission peaks at 408 and 433 nm are detected. These emissions can be attributed to the  $\pi \rightarrow \pi^*$  transitions of benzene and the carbazole ring, respectively.

In the excitation spectrum of PS-b-PSECzEu, the strongest excitation band appears at 360–400 nm, which is attributed to the overlap of the  $\pi \rightarrow \pi^*$  transition of ben-

zene, the carbazole ring and the ligand (thenoyltrifluoroacetone). In the emission spectrum, only one group of emission peaks at 577, 592, 614, 650 nm is detected.

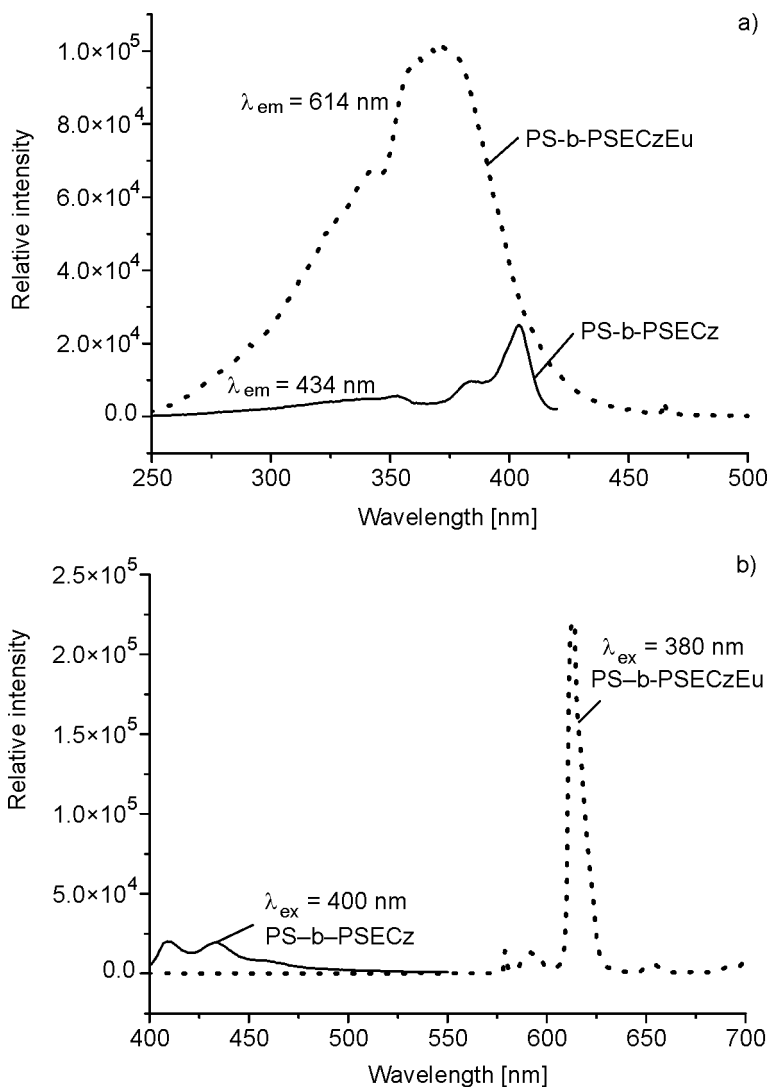


Fig. 4. Fluorescence spectra of PS-b-PSECz and PS-b-PSECzEu: a) the excitation fluorescence spectrum of PS-b-PSECz recorded in the range of 250–430 nm by monitoring the emission at 434 nm; the excitation fluorescence spectrum of PS-b-PSECzEu recorded in the range of 250–500 nm by monitoring the emission at 614 nm; b) the fluorescence spectra recorded in the range of 400–700 nm excited by the peak wavelength in the relative excitation spectra

They are assigned to the f-f transitions of the europium ions [4]. 4f levels of europium ions are protected from environmental perturbations by the occupied  $5s^2$  and  $5p^6$  orbitals, thus the fluorescence peaks of europium ions are expected to be sharp and

narrow. In addition, the presence of europium complex in PS-*b*-PSECzEu is further evidenced by the characteristic fluorescence of europium ions. The emission peaks from benzene and carbazole groups have almost been completely suppressed. This phenomenon can be explained by a long distance (Förster) energy transfer from the benzene and the carbazole groups (donors) to the europium complex (acceptor) in the excited states. Dexter energy transfer from the triplet states (T1) of the ligand (thenoyltrifluoroacetone) to the excited states of  $\text{Eu}^{3+}$  in PS-*b*-PSECzEu by molecular interaction is expected to be similar to the energy transfer mechanism in a low molecular weight europium complex. In addition, the terminal cumyl end group of copolymer by RAFT process has no effect on the luminescence property.

### 3.4. Electrochemical properties

Matching of the valence band (or the highest occupied molecular orbital (HOMO)) and conduction band (or the lowest unoccupied molecular orbital (LUMO)) energy levels of the active material to the work functions of the corresponding cathode and anode is important for the performance of a device. Cyclic voltammetry is an effective method for exploring the relative ionization and reduction potentials. The electrochemical property of PS-*b*-PSECzEu has been investigated using cyclic voltammetry.

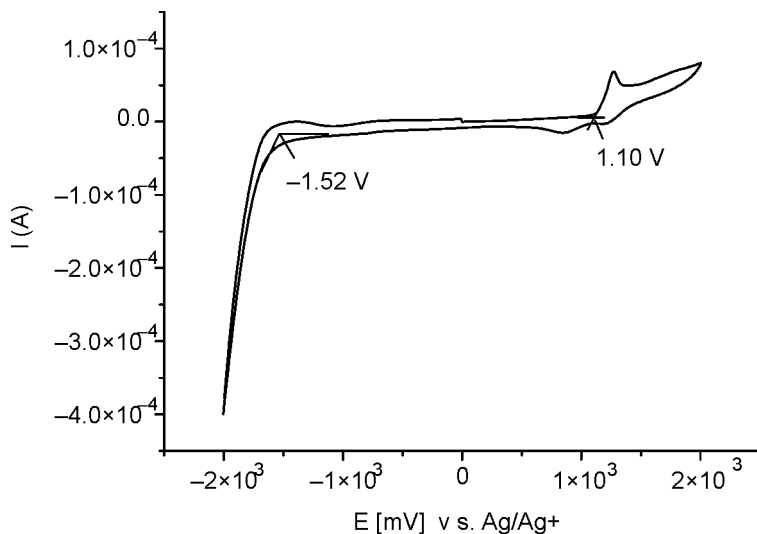


Fig. 5. Cyclic voltammogram of PS-*b*-PSECzEu in 0.1 M  $n\text{-Bu}_4\text{NPF}_6/\text{acetonitrile}$

The reduction and the oxidation onset potential of PS-*b*-PSECzEu is  $-1.52$  V and  $1.10$  V. The HOMO and LUMO energy levels of the polymer materials can be calculated from the  $E_{\text{onset}}(\text{ox})$  and  $E_{\text{onset}}(\text{red})$ , based on the reference energy level of ferrocene ( $4.8$  eV below the vacuum level) [20, 21]:

$$\text{HOMO} = E_{\text{onset(ox)}} + 4.8 - E_{\text{Foc}} \quad (3)$$

$$\text{LUMO} = E_{\text{onset(red)}} + 4.8 - E_{\text{Foc}} \quad (4)$$

wherein  $E_{\text{Foc}}$  is the potential of Foc(ferrocene)/Foc<sup>+</sup> vs. Ag/AgCl. The value of  $E_{\text{Foc}}$  is 0.46 V [22]. Based on Eqs. (3) and (4), the HOMO and LUMO energy levels of PS-*b*-PSECzEu relative to the vacuum level are estimated to be 5.44 eV and 2.82 eV, respectively. The result indicates that the HOMO and LUMO energy levels of PS-*b*-PSECzEu match well the respective work functions of ITO (4.80 eV) and Ca (2.89 eV) when used as the memory or light emitting material between the two electrodes. With the copolymer PS-*b*-PSECzEu, a balance can be achieved between the electron currents and the electron–hole currents. Thus, the block copolymer containing carbazole groups and the europium complex is a potentially useful candidate for fabricating memory or light-emitting devices.

## 4. Conclusion

A block copolymer containing carbazole groups and europium with controlled molecular weights (MWs) and narrow polydispersity was synthesized via reversible addition fragmentation chain transfer (RAFT) polymerization and coordination. The elemental analysis shows the europium content is 2.57 wt. %. The fluorescence spectroscopy of the block copolymer containing the carbazole groups and the europium complex exhibits red emission which can be attributed to the f-f transitions of the europium ion in the solid state. The long distance (Förster) energy transfer from benzene and the carbazole groups (donors) to the europium complex (acceptor) in excited states exists in the block copolymer under investigation. In addition, Dexter energy transfer from triplet states (T1) of the ligand (thenoyltrifluoroacetone) to excited states of Eu<sup>3+</sup> also takes place in the copolymer. The cyclic voltammetry data indicate that, in the copolymer, a balance can be achieved between the electron currents and the electron–hole currents. Thus, the copolymer is a potentially useful candidate for fabricating memory or light emitting devices.

### Acknowledgement

The author thanks the Key Nano Special Item of Fujian Province of China (Grants 2005HZ01-5) and Natural Scientific Foundation of Fujian Province of China (Grants E0510017, A0710001).

### References

- [1] GRAZULEVICIUS J.V., STROHRIEGL P., PIELICHOWSKI J., PIELICHOWSKI K., *Prog. Polym. Sci.*, 28 (2003), 1297.
- [2] MENG H., CHEN Z.K., YU W.L., PEI J., LIU X.L., LAI Y.H., HUANG W., *Synth. Met.*, 100 (1999), 297.
- [3] LU S., LIU T.X., KE L., MA D.C., CHUA S.J., HUANG W., *Macromolecules*, 38 (2005), 8494.
- [4] LING Q.D., KANG E.T., NEOH K.G., *Macromolecules*, 36 (2003), 6995.

- [5] JÜSTEL T., NIKOL H., RONDA C., *Angew. Chem. Int. Ed.*, 37 (1998), 3084.
- [6] LING Q.D., WANG W., SONG Y., ZHU C.X., CHAN D.S.H., KANG E.T., NEOH K.G., *J. Phys. Chem. B*, 110 (2006), 23995.
- [7] LING Q.D., SONG Y., DING S.J., ZHU C.X., CHAN D.S.H., KWONG D.L., KANG E.T., NEOH K.G., *Adv. Mater.*, 17 (2005), 455.
- [8] LOWE A.B., MCCORMICK C.L., *Aust. J. Chem.*, 55 (2002), 367.
- [9] FAVIER A., CHARREYRE M.T., CHAUMONT P., PICHOT C., *Macromolecules*, 35 (2002), 8271.
- [10] ZHANG W., ZHU X.L., ZHOU D., WANG X.Y., ZHU J., *J. Polym. Sci. Part A: Polym. Chem.*, 43 (2005), 2632.
- [11] LADAVIERE C., DÖRR N., CLAVERIE J.P., *Macromolecules*, 34 (2001), 5370.
- [12] SAHNOUN M., CHARREYRE M.T., VERON L., DELAIR T.D., AGOSTO F., *J. Polym. Sci. Part A: Polym. Chem.*, 43 (2005), 3551.
- [13] MORI H., NAKANO S., ENDO T., *Macromolecules*, 38 (2005), 8192.
- [14] LE T.P., MOAD G., RIZZARDO E., THANG S.H., WO 98/01478, (1998).
- [15] HE T., ZOU Y.F., PAN C.Y., *Polymer*, 34 (2002), 138.
- [16] RAY B., ISOBE Y., MATSUMOTO K., HABAUE S., OKAMOTO Y., KAMIGAITO M., SAWAMOTO M., *Macromolecules*, 37 (2004), 1702.
- [17] SMULDERS W., MONTEIRO M.J., *Macromolecules*, 37 (2004), 4474.
- [18] WANG L.H., WANG W., ZHANG W.G., KANG E.T., HUANG W., *Chem. Mater.*, 12 (2000), 2212.
- [19] MÖLLER T., *Gmelin Handbook of Inorganic Chemistry*, Springer, New York, 1981.
- [20] BREDAS J.L., SILBEY R., BOUDREAUX D.S., CHANCE R.R., *J. Am. Chem. Soc.*, 105 (1983), 6555.
- [21] LEE Y.Z., CHEN X.W., CHEN S.A., WEI P.K., FANN W.S., *J. Am. Chem. Soc.*, 123 (2001), 2296.
- [22] WU T.Y., SHEU R.B., CHEN Y., *Macromolecules*, 37 (2004), 725.

Received 14 May 2009  
Revised 12 November 2010

# The effect of Congo red inhibitor on the corrosion of various steels in a 3.5% NaCl medium

M. SAHIN<sup>1</sup>, A. ASAN<sup>2\*</sup>, H. CELIKKAN<sup>2</sup>, M.L. AKSU<sup>4</sup>

<sup>1</sup>Turkish Mineral Research and Exploration Institute, 06500, Ankara, Turkey

<sup>2</sup>Hitit University, Faculty of Engineering, Department of Chemical Engineering, 19030, Çorum, Turkey

<sup>3</sup>Gazi University, Faculty of Science Department of Chemistry, 06500, Ankara, Turkey

<sup>4</sup>Gazi University, Faculty of Education, Department of Chemistry Education, 06500, Ankara, Turkey

This study is concerned with the use of Congo red as an inhibitor for low alloyed carbon steel, petroleum steel and boron steel at 60 °C in 3.5% NaCl aqueous solution. Analysis was performed using the Tafel polarization measurements and electrochemical impedance spectroscopy. Congo red was observed to cover the surface by adsorbing upon it, and its inhibition efficiency depended on the concentration. The efficiency was the highest one in low-alloyed carbon steels, followed by petroleum and boron steels. The type of adsorption occurring on the metal surface was also determined.

Keywords: *alloy steels; corrosion testing; inhibitor; Congo red; EIS*

## 1. Introduction

One of the ways to prevent corrosion of metals and metal alloys is using inhibitors [1–3]. Inhibitors are organic or inorganic compounds which prevent the corrosion of metals and their alloys. Depending upon their structures [4], they achieve this by forming a protective film or an oxide layer, either by forming a complex with the metal after surface adsorption, or by oxidation of the metal. The surface adsorption of the inhibitors is realized by heteroatoms such as sulfur, nitrogen, oxygen or phosphorous with triple bonds, or aromatic rings present in their structures. Adsorption occurs as a result of the electrostatic interactions between the molecule and charged metal atoms or the electron pair or a  $\pi$  electron on the molecule and the metal surface. Thus molecules of the selected inhibitor should contain nitrogen originating from long chain aliphatic, aromatic or heterocyclic amines and their derivatives [5–8]. The inhibiting efficiency of these compounds is proportional to the number of aromatic rings and the

---

\*Corresponding author, e-mail: asanabdurrahman@hotmail.com

number of electronegative atoms in the structure [9]. It is preferable that the inhibitor be soluble in aqueous media, since the corrosion rate is particularly high in media such as HCl, H<sub>2</sub>SO<sub>4</sub> and NaCl.

This study is concerned with the inhibition effect of Congo red, containing N atoms and aromatic rings, on the corrosion of three different steels in 3.5% NaCl solution at 60 °C. Analyses were performed using the Tafel extrapolation, linear polarization, and electrochemical impedance spectroscopy (EIS). The chemical structure of the compound is shown in Fig. 1.

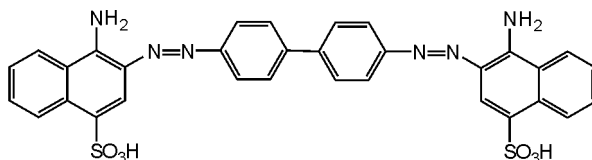


Fig. 1. Chemical structure of Congo red

## 2. Experimental

A three-compartment Pyrex glass cell was used in the experiments. The working electrodes of the compositions given in Table 1 embedded into polyester, having a 4 mm diameter surface area were placed in the middle compartment. The reference, and counter electrodes were saturated Ag/AgCl electrode and 1cm<sup>2</sup> Pt plate, respectively. The solution was purged with nitrogen purified by passing through pyrogalol, vanadium chloride, and HCl prior to each experiment in order to remove dissolved oxygen and blanketed thereafter. All solutions were prepared with triply distilled water. Before the experiments, the working electrodes were first polished with 1200 grid fine emery paper then polished with 0.5 μm alumina. The temperature of the system was kept constant within ±1 °C accuracy with a circulating water bath.

Table 1. The compositions of the steels used

Type of steel	Content [%]											
	C	Si	Mn	P	Cr	Mo	Ni	B	Al	Ti	V	R
Petrol line steel	0.28	0.44	1.46	0.01	1.18	0.07	1.20	–	–	–	–	0.1
Low alloyed carbon steel	0.30	0.03	1.35	0.03	1.0	–	0.40	–	0.050	–	–	0.10
Boron steel	0.2	0.1	1.70	0.025	0.80	0.80	–	0.04	0.03	0.26	0.60	0.05

The potentiostatic and impedance measurements were carried out with a CHI 660 electrochemical analyzer equipped with electrochemical software. The polarization curves were taken at the scan rate of 2 mV/s between 250 mV anodic and cathodic of the open circuit or the equilibrium potential.

### 3. Results and discussion

#### 3.1. Polarization measurements

Figures 2–4 show the potential–current curves of three different steels in a 3.5% NaCl medium for various concentrations of the inhibitor. The corrosion potentials shifted to significantly higher anodic values and the corrosion currents showed a marked decrease upon the addition of the inhibitor. The fact that the corrosion potential

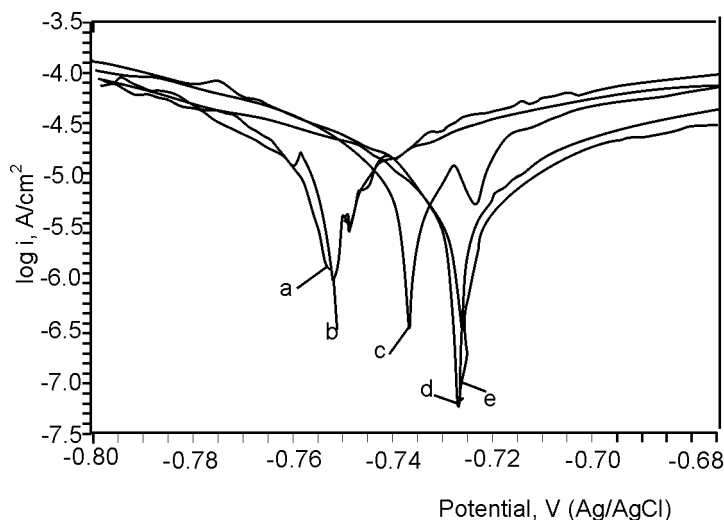


Fig. 2. The current–potential curves of low alloyed carbon steel blank (a) and with Congo red of the concentration: b)  $1 \times 10^{-4}$  M, c)  $2 \times 10^{-4}$  M, d)  $5 \times 10^{-4}$  M, e)  $1 \times 10^{-3}$  M

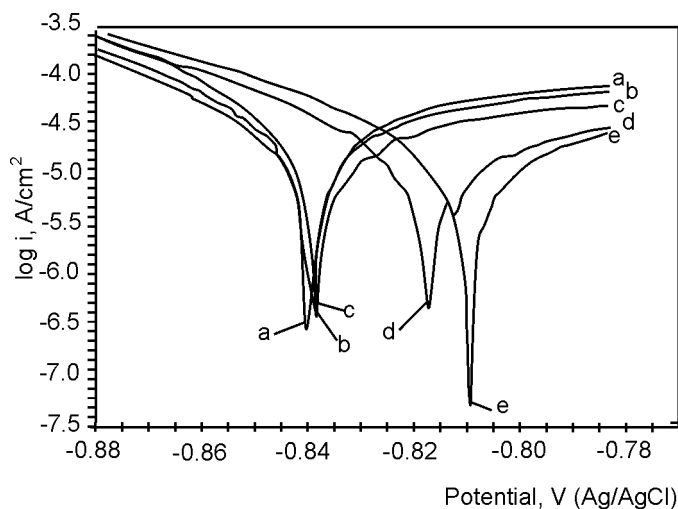


Fig. 3. The current–potential curves of petroleum steel blank (a) and with Congo red of the concentration: b)  $1 \times 10^{-4}$  M, c)  $2 \times 10^{-4}$  M, d)  $5 \times 10^{-4}$  M, e)  $1 \times 10^{-3}$  M

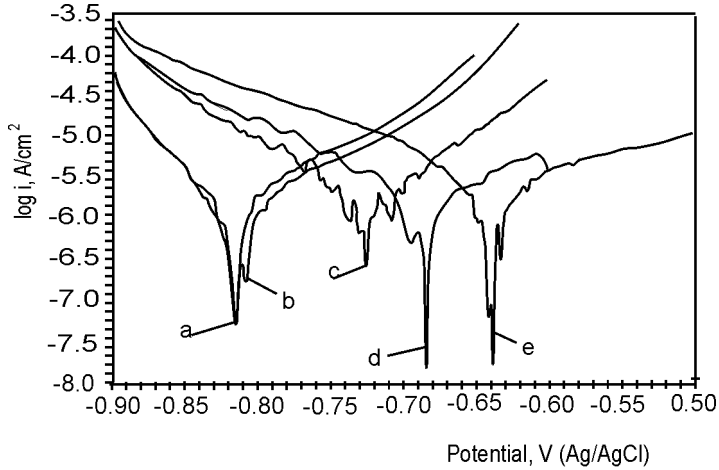


Fig. 4. The current potential curves of boron steel blank (a) and with Congo red of the concentration: b)  $1 \times 10^{-4}$  M, c)  $2 \times 10^{-4}$  M, d)  $5 \times 10^{-4}$  M, e)  $1 \times 10^{-3}$  M

displayed an anodic shift of nearly 200 mV for boron steel in the presence of Congo red indicates that it is a good anodic inhibitor. Other steels also show similar behaviour demonstrating that formation of adsorbed films on their surfaces [11]. The compound has the efficiency of 88% and acts as a good inhibitor of mixed type. Steel containing boron was found to have the corrosion resistance twenty times higher than the other steels.

### 3.2. Electrochemical impedance spectroscopy measurements

Figures 5–7 show the Nyquist diagrams obtained for the steels under investigation in a 3.5% NaCl solution for various concentrations of Congo red.

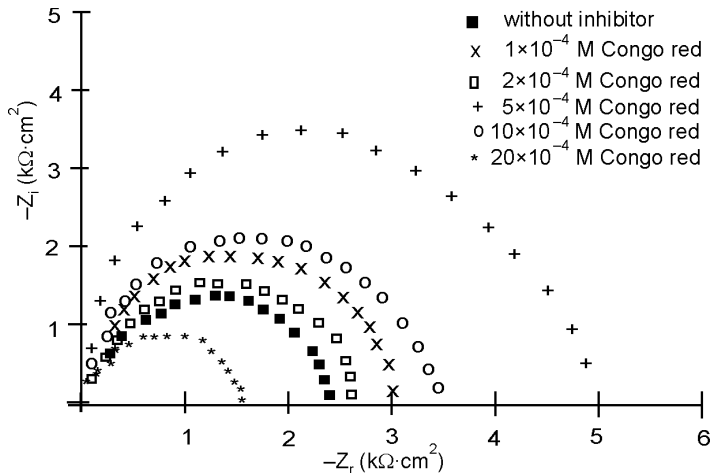


Fig. 5. The Nyquist diagrams of boron steel

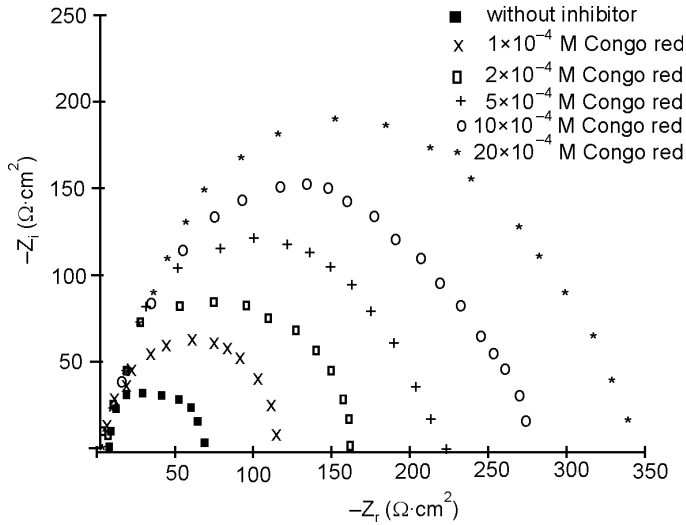


Fig. 6. The Nyquist diagrams of low alloyed carbon steel

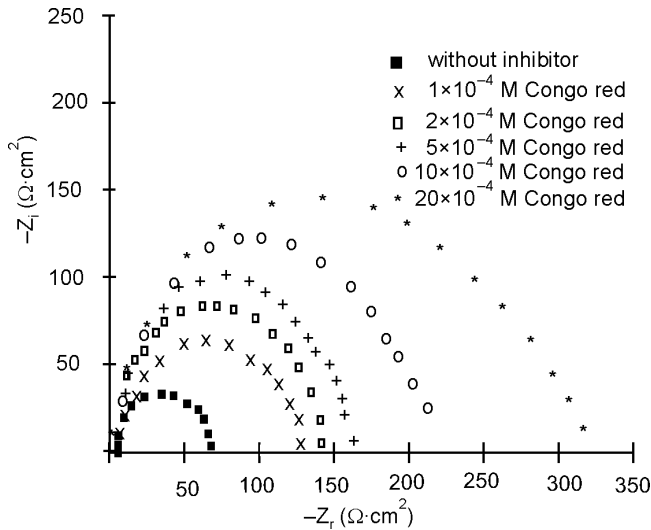


Fig. 7. The Nyquist diagrams of petroleum steel

The curves were obtained in the frequency range of  $10^5$ – $10^{-2}$  Hz. It is seen that the diameters of the semi circles increase as the concentration of the inhibitor increases, indicating the increase of the charge transfer resistance  $R_p$  [12]. The  $R_p$  values and the inhibition efficiencies  $\eta_{eis}$  calculated for each concentration are tabulated in Table 2. Here  $\eta_{eis}$  is calculated according to

$$\eta_{eis} = \frac{R_{ti} - R_t}{R_{ti}} \times 100 \quad [\%]$$

where,  $R_{ti}$  and  $R_t$  represent the charge transfer resistances obtained with and without the inhibitor.

### 3.3. Linear polarization method

The  $R_p$  values obtained from impedance spectroscopy measurements can also be calculated by the linear polarization method. Here using the polarization curves, the  $R_p$  values can be computed from the Stern–Geary equation as follows [13]:

$$i_{\text{cor}} = \frac{B}{R_p}$$

where  $B$  is given as

$$B = \frac{\beta_a \beta_c}{2.303(\beta_a + \beta_c)}$$

$R_p$  is calculated from the slope of the polarization curve. The values for the inhibition efficiency  $\eta_{ip}$  obtained by the linear polarization method are also given in Table 2, for comparative purposes.

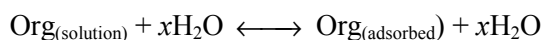
Table 2. Inhibition parameters obtained by the measurements

Steels	Concentration ( $\times 10^4$ M)	$-E_{\text{cor}}$ [mV]	$R_{p,\text{seis}}$ [ $\Omega \cdot \text{cm}^2$ ]	$\eta_{\text{eis}}$ [%]	$R_{p,\text{lp}}$ [ $\Omega \cdot \text{cm}^2$ ]	$\eta_{\text{lp}}$ [%]
Low alloyed carbon steel	blank	775	62.2	–	68	–
	1	756	127.7	51.3	144	53.2
	2	742	164.1	62.1	154	66.2
	5	733	211.6	70.6	262	74.3
	10	735	286.6	78.3	357	81.5
	20	720	351.4	82.3	503	86.5
Petroleum steel	blank	840	67.6	–	73	–
	1	841	124.0	45.5	140	48.3
	2	839	142.6	52.8	162	55.6
	5	821	158.3	57.3	196	63.1
	10	816	218.4	71.3	331	78.2
	20	810	336.3	79.9	429	83.6
Boron steel	blank	819	1462.3	–	1510	–
	1	818	2473.7	40.1	2745	45.1
	2	727	2732.7	46.5	3032	50.2
	5	684	3064.9	52.3	3355	55.3
	10	639	3610.3	59.5	4070	63.1
	20	605	5147.8	71.6	6040	75.6

#### 4. Discussion

The efficiency of an organic inhibitor of metallic corrosion is dependent not only on the size of its molecules but also on the environment, nature of the metal, experimental parameters such as the inhibitor concentration [14], molecular structure and the nature of the molecule itself [15].

The adsorption of the organic compound at metal–solution interface in aqueous solution may be illustrated by the following equation [16]



where  $x$  is the number of water molecules replaced by the adsorption per mole of organic compound.

There are three major types of mathematical models describing adsorption isotherms, namely the Langmuir, Frumkin and Temkin isotherms [17–20]. All these isotherms are generally given as

$$f(\theta, x)\exp(-2a\theta) = KC$$

Here  $f(\theta, x)$  is a configuration factor dependent upon the physical model employed,  $\theta$  and  $C$  are the surface coverage ratio and the concentration of the inhibitor, respectively;  $x$  stands for the magnitude factor, being the intermolecular interaction parameter and  $K$  is the adsorption parameter [21].

According to Temkin and Langmuir, isotherms are given as  $\exp(-2a\theta) = KC$  and  $\theta = KC(1 - \theta)$ . In this study, the adsorption of the inhibitor was found to be best described by the Langmuir isotherm when boron steel was used as the adsorbent, whereas it was best described by the Temkin isotherm when other steels were used (Figs. 8, 9).

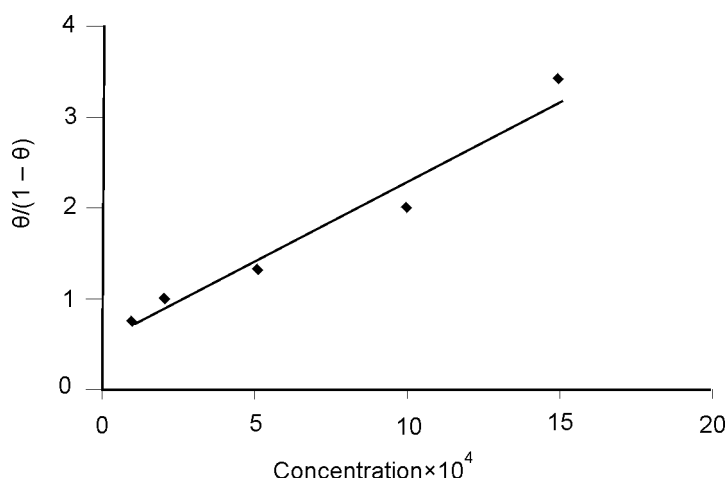


Fig. 8. The Langmuir isotherm of boron steel obtained by the addition of Congo red inhibitor at various concentrations in 3.5% NaCl medium

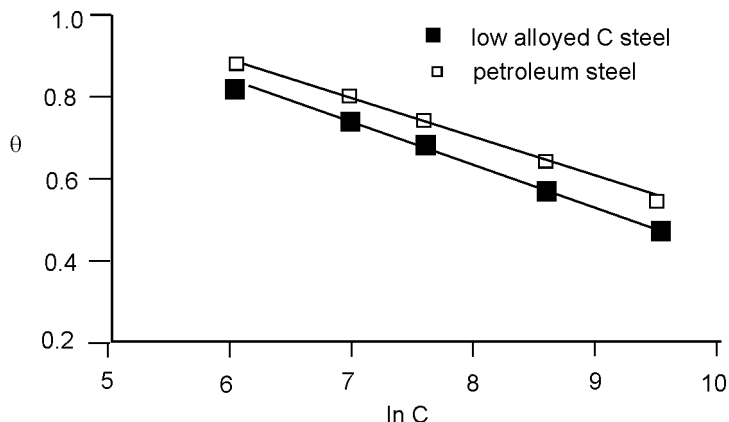


Fig. 9. The Temkin isotherms of petroleum and low alloyed carbon steel obtained by the addition of Congo red inhibitor at various concentrations in 3.5% NaCl medium

It is known that Congo red is used as an indicator in biochemical studies and precipitation of metal ions in a solution [22]. However, in this study, it was used for the first time as a corrosion inhibitor. Its inhibition efficiency was calculated by two different methods: the calculated values were found to be similar. It shows inhibition efficiency up to 80% at the inhibitor concentration of  $2 \cdot 10^{-3}$  M. The corrosion potentials are shifted to more positive values compared with the equilibrium or open circuit potential. In this study, the efficiency of the inhibitor was found to be high for the low alloyed corrosion prone carbon steel and low for the corrosion resistant boron steel.

Based on the adsorption isotherms, distinction between its physical or chemical nature is ambiguous. However it is obvious that the adsorption conditions will differ depending upon the composition of the steels. The compound can easily adsorb upon the steel surface due to nitrogen atoms and  $\pi$  electrons of the aromatic structure. The fact that the adsorption is of Langmuir type on low alloyed carbon steel and petroleum steels, and is of Temkin type on boron steel results from various compositions of the steels.

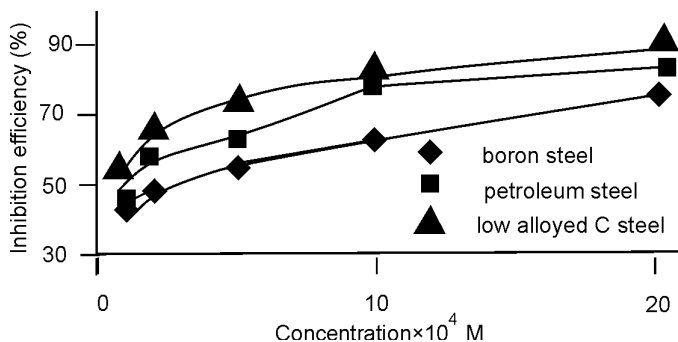


Fig. 10. Dependence of inhibition efficiency of Congo red on the concentration in 3.5% NaCl solution

In conclusion, Congo red was observed to cover the surface by adsorbing upon it and its inhibition efficiency increased with the concentration. The efficiency was highest in low alloyed carbon steels (Fig. 10)

## References

- [1] FONTANA M.G., *Corrosion Engineering*, 3rd Ed., McGraw-Hill, Singapore, 1986.
- [2] FLICK E.W., *Corrosion Inhibitors*, Park Ridge, New Jersey, 1987, p. 68.
- [3] WEBER C.R., DICK L.F.P., BENÍTEZ G., VELA M.E., SALVAREZZA R.C., *Electrochim. Acta*, 54 (2009), 4817.
- [4] NATHAN C.C., *Organic Inhibitors*, NACE, Houston, 1997.
- [5] SAHIN M., BILGIC S., *Anti-Corrosion Meth. Mater.*, 1 (2003), 50.
- [6] EFIRD K.D., JARINSKI R.J., *Corrosion*, 45 (1989), 165.
- [7] FRIGNANI A., FONSATTI M., MONTICELLI C., BRUNORO G., *Corrosion Sci.*, 41 (1999), 1217.
- [8] JOVANCICIEVIC V., RAMANCHANDRAN S., PRINCE P., *Corrosion*, 55 (1998), 449.
- [9] GRANESE S.L., ROSALES B.M., OVIEDO C., ZERBINO J.O., *Corros. Sci.*, 33 (1992), 1439.
- [10] MANSFELD F., *Corrosion*, 29 (1973), 297.
- [11] DEHRI I., ERBIL M., *Doğa*, 42 (2000), 969.
- [12] STERN M., GEARY M., *J. Electrochem. Soc.*, 104 (1956), 56.
- [13] COSTA J.M., LLUCH J.M., *Corrosion Sci.*, 24 (1984), 929.
- [14] AKIYAMA A., NOBE K., *J. Electrochem. Soc.*, 117 (1970), 993.
- [15] MORETTI G., QUARTORONE G., TASSAN A., ZINGALES A., *Werkstoffe Korr.*, 45 (1994), 641.
- [16] LANGMUIR I., *J. Amer. Chem. Soc.*, 39 (1848), 1917.
- [17] DAMASKI B.B., PETRI D.A., BATRAKTOV B., *Adsorption of Organic Compounds on Electrodes*, Plenum Press, New York, 1971.
- [18] FRUMKIN A.N., *Phys. Chem.* (1925) 116.
- [19] BOCKRIS J.O., SWINKELS D., *J. Electrochem Soc.*, 111 (1973), 736.
- [20] ATEYA B., EL-ANADOULI B., EL-NIZAMY F., *Corrosion Sci.*, 24 (1984), 509.
- [21] ZEROVNIK E., POMPA-NOVAK M., SKARABOT M., *Biochim. Biophys. Acta*, 1594 (2002), 1.
- [22] KRANNENBURG O., KROON-BATENBURG M.J., REIJERKERK A., *FEBS Lett.*, 539 (2003), 149.

Received 12 June 2009

# Preparation of Ni/MgO catalysts for carbon nanofibres by a self-propagating low temperature combustion process

Y. ZHANG<sup>1</sup>, Y.H. TANG<sup>2\*</sup>, E.L. ZHANG<sup>2</sup>, L.W. LIN<sup>2</sup>, L.Z. PEI<sup>3</sup>

<sup>1</sup>Department of Mechanical Engineering, Xiamen University of Technology,  
Xiamen Fujian 361024, P.R. China

<sup>2</sup>College of Materials Science and Engineering, Hunan University,  
Changsha, Hunan 410082, P.R. China

<sup>3</sup>School of Materials Science and Engineering, Anhui University of Technology,  
Ma'anshan Anhui 243002, P.R. China.

Ni/MgO catalysts were prepared using nitrate salt and citric acid in various ratios by the sol-gel self-propagating, low temperature combustion process. The products were characterized by the scanning electron microscopy, X-ray diffraction, thermogravimetric analysis and differential scanning calorimetry. The results show that Ni/MgO catalyst precursors of various particle sizes can be obtained by controlling the amount of citric acid. The catalytic activity of Ni/MgO decreases as the calcination temperature increases, owing to the difficulty of the NiO reduction. The mechanism of formation of Ni/MgO catalysts has also been proposed. Self-propagation combustion has great advantage of occurring at low temperatures, and the Ni/MgO is a suitable catalyst for low cost preparation of carbon nanofibres.

Keywords: *Ni/MgO catalyst; self-propagating combustion; sol-gel method*

## 1. Introduction

The availability of a catalyst of high activity and low cost is a key factor for the preparation of bulk-quantities of carbon nanofibres by the catalytic chemical vapour deposition (CVD) method. Generally, Fe, Co and Ni are used as the catalysts, owing to their large specific surface area. However, these nanoscale metal catalysts have great disadvantages, such as high cost and low catalytic activity, due to the conglomeration [1, 2] and difficulty with recycling [3]. Catalyst supports are the most effective way to improve catalyst activity. The catalyst may be highly dispersed onto supports,

---

\*Corresponding author, e-mail: nwfs@sina.com

and may decrease conglomeration. Research on the use of  $\text{Al}_2\text{O}_3$ ,  $\text{SiO}_2$  and  $\text{MgO}$  as the supports showed that the catalytic activity and reaction time may be improved [4–6]. Among various supports,  $\text{MgO}$  has the advantage of being easy to remove during the purification of the as-grown carbon nanofibres [7, 8]. Therefore, great interest has been devoted to the study of  $\text{MgO}$  as a catalyst support in the preparation of carbon nanofibres by the catalytic CVD method.

Magnesium oxide is a kind of good alkali catalyst support, while metallic nickel has catalytic activity at low temperature. Therefore,  $\text{Ni/MgO}$  catalyst offers excellent potential for the preparation of carbon nanofibres owing to its high activity, selectivity and low cost [9, 10]. An  $\text{Ni/MgO}$  catalyst may be fabricated in two main ways, namely by the co-precipitation or the sol-gel method. Using the co-precipitation,  $\text{Ni/MgO}$  catalyst precursors may be produced by high temperature sintering of the hydroxide precursor of  $\text{Ni/MgO}$  obtained from mixed solutions of  $\text{Mg}(\text{NO}_3)_2$ ,  $\text{Ni}(\text{NO}_3)_2$  and  $\text{KOH}$  [11–15].  $\text{Ni/MgO}$  catalyst precursors can also be fabricated by sol-gel method sintering of citrate gel obtained from mixed solutions of  $\text{Mg}(\text{NO}_3)_2$ ,  $\text{Ni}(\text{NO}_3)_2$  and citrates [9, 16–18]. The co-precipitation is not suitable for fabrication of  $\text{Ni/MgO}$  catalyst precursors in bulk quantities, due to a long time of syntheses. On the other hand, the synthesis may easily be controlled by the sol-gel method and can also be conducted on a large-scale. In addition,  $\text{Ni/MgO}$  catalyst precursors must be calcined at temperatures higher than  $700\text{ }^\circ\text{C}$ , which makes the process more costly. At the same time, a higher calcination temperature is necessary to obtain  $\text{NiO-MgO}$  solid solution, with  $\text{NiO}$  diffusing into the  $\text{MgO}$  lattice which restricts the  $\text{NiO}$  to be reduced [19]. A strong oxidation-reduction reaction occurs when heating the organic salt gels, or organic salt and metal nitrate. The reaction releases an abundance of heat which can maintain the reaction space, resulting in formation of oxide powders; the method is known as the sol-gel self-propagating combustion method [20, 21]. The method has the advantage of having a low ignition point ( $150\text{--}250\text{ }^\circ\text{C}$ ) and it can produce powders which have high specific surface areas. It is a low temperature self-propagating combustion process, in contrast with a high temperature self-propagating combustion process [22].

In the paper, we report on the synthesis of  $\text{Ni/MgO}$  catalysts, using citric acid as the reduction agent and  $\text{Mg}(\text{NO}_3)_2$  and  $\text{Ni}(\text{NO}_3)_2$  as the oxidation agents, by a simple sol-gel self-propagating low temperature combustion process at ca.  $250\text{ }^\circ\text{C}$ . The influence of the ratio of citric acid to nitrate salt on the particle size of the catalyst precursors, and the role of the temperature on the sintering property of the catalysts, have been analysed in detail. The  $\text{Ni/MgO}$  catalyst powders synthesized by the low temperature self-propagating combustion process were compared with the powders that had been synthesized by direct calcination at higher temperatures. A formation mechanism of the  $\text{Ni/MgO}$  catalyst precursors synthesized by low temperature self-propagating combustion process is also proposed. The results show that the method takes great advantage of simple apparatus and the synthesis process in which the parti-

cle size of the Ni/MgO can be controlled. This therefore makes it a suitable method for the synthesis of catalysts of carbon nanofibres.

## 2. Experimental

The catalyst precursors were synthesized by the sol-gel self-propagating low temperature combustion process. Stoichiometric quantities of  $\text{Ni}(\text{NO}_3)_2 \cdot 6\text{H}_2\text{O}$  and  $\text{Mg}(\text{NO}_3)_2 \cdot 6\text{H}_2\text{O}$  with molar ratios of Ni to Mg of 2:1, and molar ratios of nitrate salt to citric acid of 1:1, 1:2, 1:3 and 1:4 were mixed and fully dissolved in a given amount of distilled water, and then stirred for 2 h at 20 °C. Then water was removed in an oven at 90 °C until green gel-like products were formed. The yellow-green foam products were further formed by heating them in an oven at 200 °C for 30 min and then at 250 °C in a crucible, to form grey-black Ni/MgO precursor powders. In addition, the foam products were also calcined in air for 2.5 h at 600 °C, 700 °C and 800 °C. The final powder products were then obtained by pulverizing these calcined products.

Scanning electron microscopy observations were performed using a JEOL JSM-5600LV (15 KV) field emission scanning electron microscope. The X-ray diffraction patterns were obtained using a Siemens D5000 X-ray diffractometer with graphite monochromatized  $\text{CuK}_\alpha$  radiation ( $\lambda = 1.5406 \text{ \AA}$ ). The samples were scanned at the rate of 0.05 deg/s in the  $2\theta$  range of 10–80°. Thermogravimetric analyses and differential scanning calorimeter measurements were performed using a STA449C (Netzsch, Germany) in air at the ramp rate of 2 deg/min.

## 3. Results and discussion

The thermogravimetric and differential scanning calorimeter (TG/DSC) curves of the Ni/MgO catalyst precursor gels are shown in Fig. 1. The molar ratios of nitrate salt to citric acid were 1:1 (sample A), 1:2 (sample B), 1:3 (sample C) and 1:4 (sample D). Figure 1a shows the TG curves for samples A–D, which are labelled accordingly. The combustion process for samples A and B initially starts at 200 °C but it becomes more dramatic for A at 270 °C and for B at 350 °C. The TG curves for C and D differ significantly from those for A and B, and exhibit weight loss at 200 °C and 350 °C, respectively, with the increase in the amount of citric acid. According to the DSC curves (Fig. 1b), the exothermic peak increases noticeably at 270 °C for sample A, and very small exothermic peaks occur at 350 °C for samples B, C and D. Therefore, thermal decomposition of Ni/MgO catalyst precursor gels can be explained as occurring in the stages as follows:

- The endothermic process in the DSC curves corresponding to evaporation of water in the gels and fusion of the gels between 70 °C and 200 °C.
- The organic complex compounds decompose from 200 °C to 350 °C, releasing an abundance of heat. However, the change in this stage is closely related to the quantity of citric acid. The gel powder A (1:1) decomposes quickly at 270 °C showing the

exothermic peak on the DSC curve. The weight losses of B and C gels increase dramatically at 350 °C with very small exothermic peaks. This is considered to be mainly attributed to the lower energy requirement for the decomposition of the dissociative carboxylic acid and carboxylic acid salt compared with the energy requirements for gels with higher contents of citric acid. In particular, an endothermic peak at 200 °C is also clearly observed when the molar ratio of the nitrate salt to the citric acid is up to 1:4, which may be caused by the decomposition of the excessive dissociative carboxylic acid. The combustion time at 200 °C increases, and the excessive citric acid of the C and D gels is considered to be partially responsible for this.

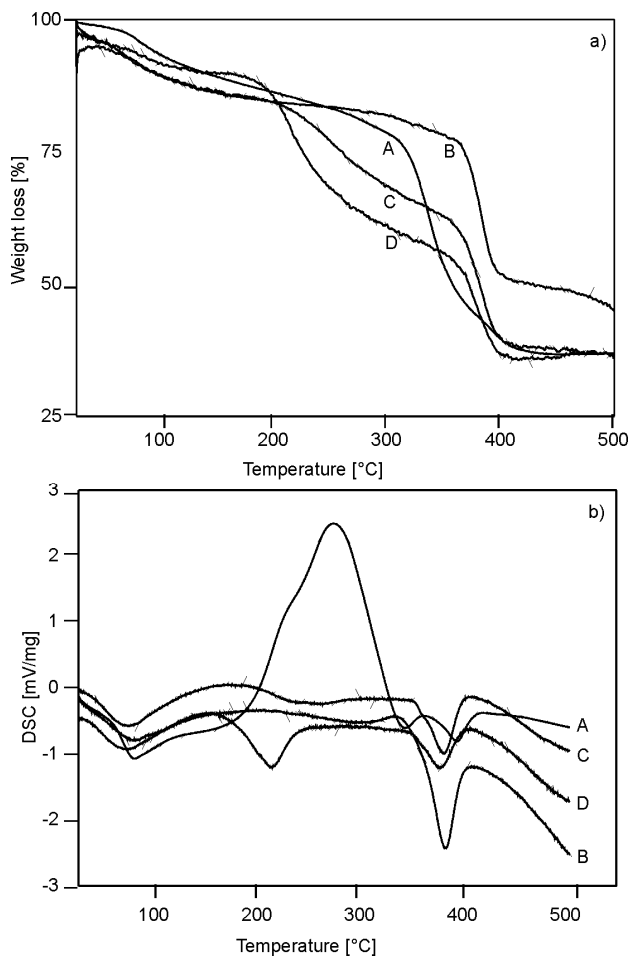


Fig. 1. TG (a) and DSC (b) curves of the catalyst precursor gels

• Ni/MgO catalyst powders form at temperatures higher than 350 °C. The weight losses of gels C and D increase dramatically, owing to the decomposition of the exces-

sive citric acid, according to the TG curves. Thermal decomposition of the catalyst precursor gels is complete above 400 °C.

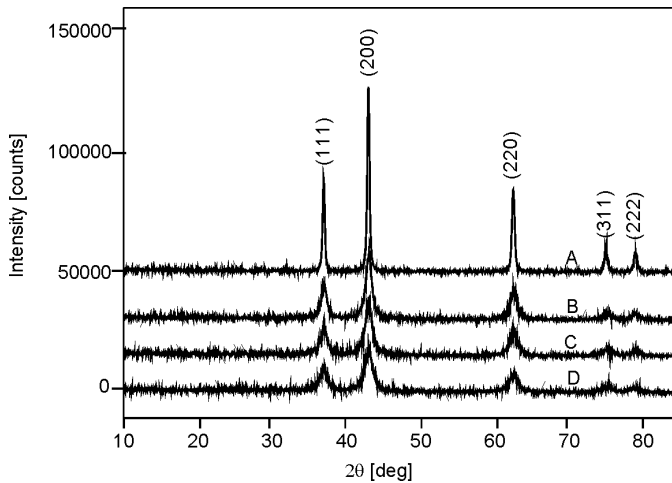


Fig. 2. XRD patterns of the gels with various ratios of nitrate salt and citric acid after self-propagating combustion: A – 1:1, B – 1:2, C – 1:3, D – 1:4

X-ray diffraction (XRD) patterns of the gel powders with various ratios of nitrate salt to citric acid and produced by self-propagating combustion are shown in Fig. 2.  $\text{Ni}_x\text{Mg}_{1-x}\text{O}$  solid solution can be formed from MgO and NiO at random proportions owing to the fact that the lattice parameters of MgO and NiO are similar to that of the NaCl crystal, and that the ionic radii of  $\text{Mg}^{2+}$  and  $\text{Ni}^{2+}$  are very close (0.65 Å and 0.70 Å, respectively). The diffraction peaks of the samples can all be indexed to Ni/MgO solid solution by consulting the data given in the Joint Committee on Powder Diffraction Standards (JCPDS) card for Ni/MgO solid solution (JCPDS 24-0712). The diffraction intensity of the Ni/MgO solid solution decreases significantly and the diffraction peaks broaden with the increase in the proportion of citric acid in samples A to D. The crystalline size of the samples also decreases in inverse proportion to the quantity of citric acid; the average crystalline sizes of samples A to D were calculated, using the Scherrer formula, to be 26.7 nm, 23.75 nm, 19.43 nm and 15.8 nm, respectively.

Scanning electron microscopy (SEM) images of the samples A–D obtained by the self-propagating combustion process are shown in Fig. 3. Ni/MgO catalysts display particle structures with distinct interfaces among the particles. The particle size evidently decreases as the proportion of citric acid increases. The average particle size is highest, reaching the value of 100 nm with an uneven size distribution when the molar ratio of the nitrate salt to citric acid is 1:1. However, the particles have the average size of only 20 nm and a uniform size distribution if the molar ratio of nitrate salt to citric acid is decreased to 1:4.

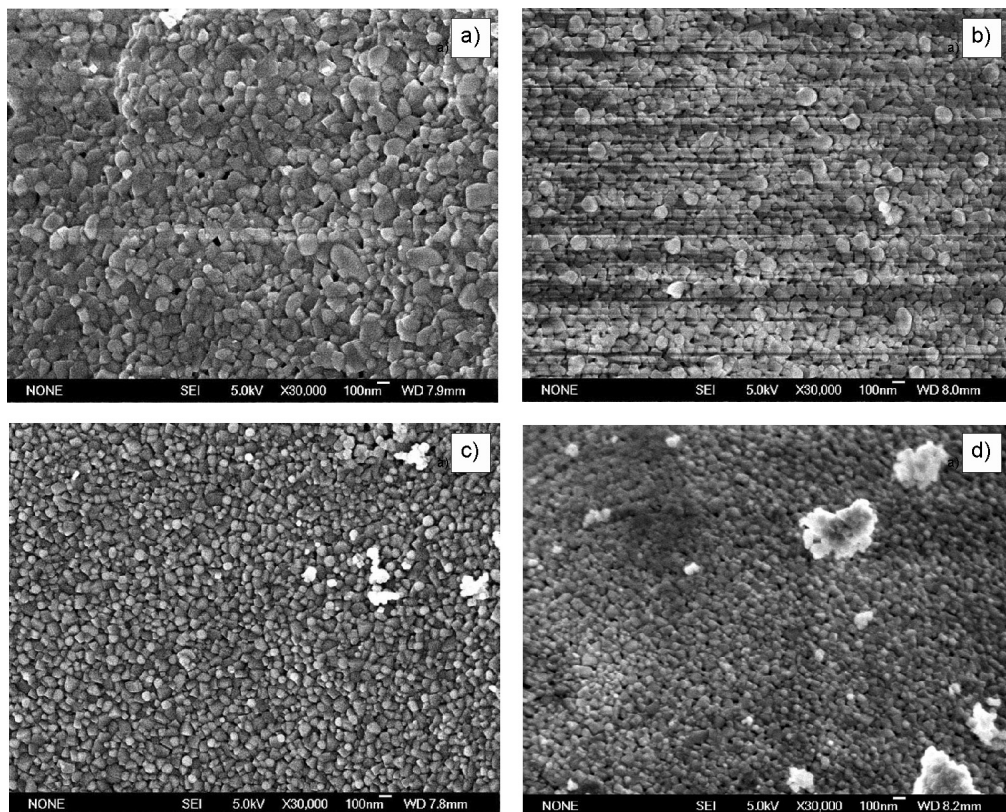


Fig. 3. SEM images of the gels with different ratios of nitrate salt and citric acid after self-propagating combustion: a) 1:1, b) 1:2, c) 1:3, d) 1:4

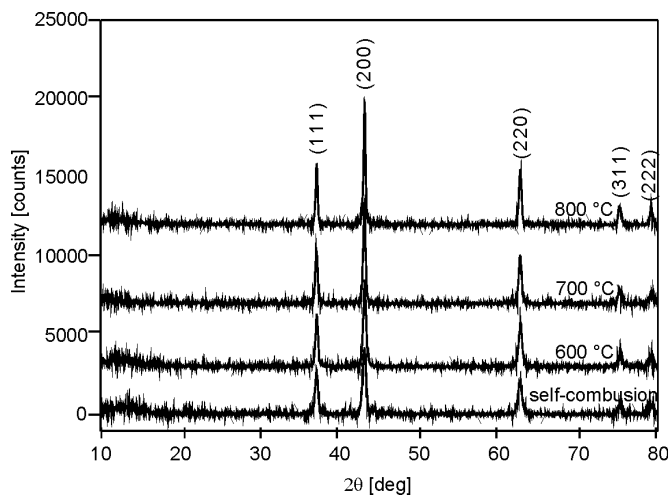


Fig. 4. XRD patterns of the catalyst precursor gel sample B with the molar ratio of 1:2 obtained by a self-propagating combustion process and calcination at various temperatures

Figure 4 shows the XRD patterns of the catalyst precursor sample B (1:2) obtained by self-propagating combustion and calcination at 6 various temperatures. The crystalline structures of the samples are the same as that of NaCl crystal, according to the XRD patterns. The diffraction intensity of the samples increases upon increasing calcination temperature. The results show that Ni/MgO catalyst precursors can be obtained by self-propagating combustion of gels without high temperature heat treatment.

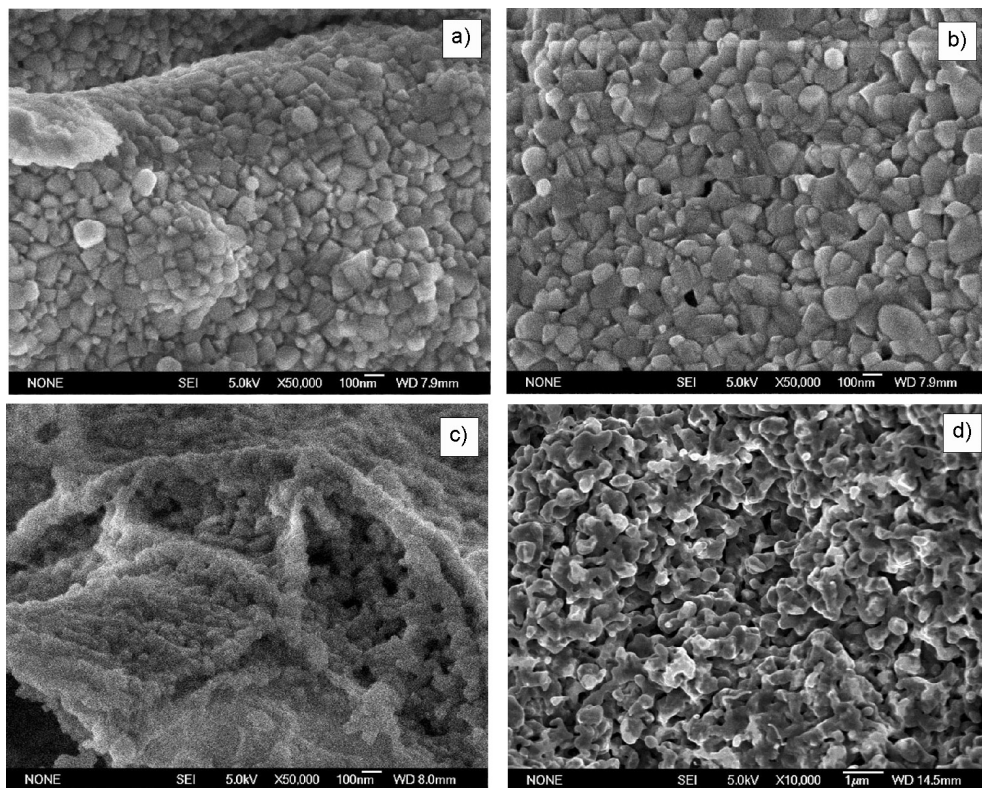


Fig. 5. SEM images of the gels B (1:2) after calcination at various temperatures: a) 600 °C, b) 700 °C, c) 800 °C, d) heat treatment Ni at 600 °C

Figure 5 shows the SEM images of samples B calcined at various temperatures. Compared with Fig. 3b, the products maintain an excellent dispersive state. Regular prismatic and spherical structures with obvious crystal interfaces can be observed in the sample calcined at 600 °C (Fig. 5a). The particle size increases and the particles become deformed after calcination at 700 °C (Fig. 5b). Finally, particles with irregular morphology appear if the sintering temperature is increased to 800 °C (Fig. 5c). The crystal interfaces are obscure and the specific surface areas of the samples also decrease. Therefore, the catalyst precursors can be aggregated by increasing the calcination temperature; this can lower the catalytic activity of the Ni/MgO powders. The

sintering property of the Ni/MgO catalyst powders is also analyzed by making comparisons with nanoscale Ni powders that had been produced without support (Fig. 5d). The specific surface area of the nanoscale Ni powder increases dramatically upon increasing particle size due to the surface effect. It results in an increase of the surface energy. The nanoscale Ni powders attain a semi-molten state at 250 °C, showing that nanoscale Ni powders can be sintered easily.

MgO support has a high dispersive effect resulting in high dispersion of NiO. In addition, the interaction of NiO and MgO prevents the dispersion of particles on the support during the thermal treatment. However, some nanoscale NiO particles aggregate to form particles of large sizes, and the others permeate into the MgO resulting in the sintering process as the temperature increases to 800 °C.

Carbon nanofibres were fabricated at 550 °C, 600 °C, 700 °C and 800 °C using the Ni/MgO catalyst precursor sample A obtained by the self-propagating combustion process. Definite amounts of catalyst precursors were introduced into the horizontal ebullition stove [23]. Then the furnace was heated to a set temperature with the flow of H<sub>2</sub> for 30 min and the flow of CH<sub>4</sub> for 60 min, respectively. After being cooled to room temperature in Ar, the carbon nanofibre products were obtained. The yield of carbon nanofibres  $\eta$  may be calculated by the following formula:

$$\eta = \frac{m_{\text{carbon nanofibres}}}{m_{\text{catalyst}}} \times 100 \quad [\%]$$

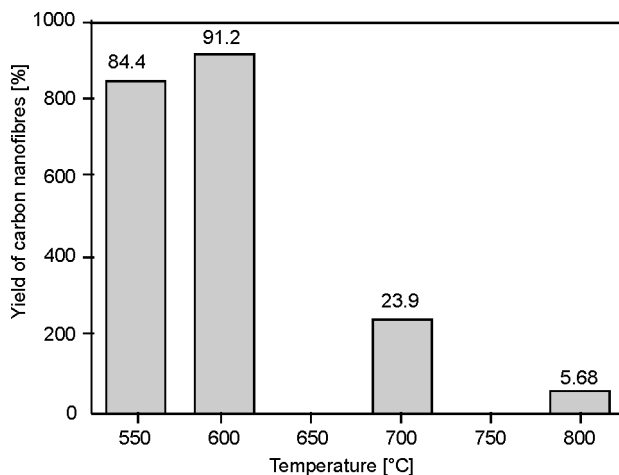


Fig. 6. The yield of carbon nanofibres fabricated with a Ni/MgO catalyst at various temperatures

According to Figure 6, the best growth temperature for the carbon nanofibres is 600 °C, with the highest yield of 91.25%. The yield of the carbon nanofibres decreases dramatically with the temperature, further showing that the temperature plays an important role in the formation of Ni/MgO solid solution. NiO diffuses into MgO, result-

ing in the formation of the NiO/MgO based solid solution after high temperature roasting at 700 °C and preventing the reduction of NiO. At the same time, Ni/MgO reduced from NiO/MgO at 550~600 °C is the most efficient catalyst for growing the carbon nanofibres.

Ni/MgO catalyst precursors were fabricated using citric acid as the gelling agent. Esterification and dehydration occur in the presence of citric acid under acid conditions, forming a sol-gel skeleton of a high molecular polymer with a complex netted texture, because citric acid belongs to hydroxy acids containing both with -COOH and -OH groups in the molecule. The netted texture provides electron pairs as the Lewis base and metal ions  $Mg^{2+}$  and  $Ni^{2+}$  provide empty orbitals as the Lewis acids. Complex reaction occurs among metal ions and a high molecular polymer to form carboxylic acid salt dispersing in the gels without segregation of the composition.

Citric acid salt gels formed from nitrate salt and citric acid are characteristic products of self-propagating combustion. Nitrate salt and citric acid are used as the oxidation agent and the reduction agent, respectively. *In-situ* oxidation-reduction reaction occurs between  $NO_3^-$  and  $COO^{2-}$  of the gels at a specific temperature, resulting in low temperature self-propagating combustion. NiO and MgO powders are formed from metal ions with the exothermic reaction. Then the NiO/MgO solid solution is further formed with the increase in temperature. The chemical reaction becomes complete only when the ratio of oxidation agent to reduction agent is 1:1. Liu et al. [24] analysed the synthesis of NiO with citric acid and  $Ni(NO_3)_2$  as the starting materials. According to the propellant thermal chemical theory, the theoretical ratio of the  $Ni(NO_3)_2$  to citric acid is 1.8:1 when the total oxidation valence is equal to the total reduction valence. However, unlike the above results, the self-propagating combustion process is most efficient when the ratio of the nitrate salt and citric acid is 1:1 which may be caused by the effect of the  $O_2$  in the air during the self-propagating combustion. The oxidation agent is not sufficient with the increasing content of citric acid resulting in decarbonization of the excessive citrate and the decrease of the combustion zone temperature. The results are confirmed by the weight loss of samples C and D at 350 °C (Fig. 1a). At the same time, the crystal size of NiO/MgO solid solution also decreases obviously with the temperature decrease in the combustion zone.

The combustion temperature for the dry gels originating from the nitrate salt and citric acid is an important factor for the formation of NiO/MgO solid solution. The proportion of the solid solution in the products is essential for the catalyst activity of the Ni/MgO. Two formation process of the solid solution may occur due to the effect of the temperature during the reaction of NiO and MgO:

- Reductive NiO based MgO/NiO solid solution may form with the diffusion of NiO on the surface of MgO (1).
- MgO based NiO/MgO solid solution difficult to reduce also may occur as NiO diffuses into the MgO lattice. Therefore, the catalyst activity of Ni/MgO is determined by the location of NiO in the MgO.

## 4. Conclusions

Ni/MgO catalysts were prepared using nitrate salt and citric acid at various ratios, by the sol-gel self-propagating, low temperature combustion. Thermal decomposition of the catalyst precursor gels was analyzed in detail. Close attention was given to how the ratio of citrate and nitrate salt influences the particle size of the catalyst precursors, and also the role of temperature on the sintering property of the catalysts is considered. The gels decompose dramatically when the ratio of the nitrate salt to citric acid is 1:1. The particle size of the catalyst precursors decreases in inverse proportion to the citric acid content. The crystalline structures of the catalyst precursors obtained by the self-propagating combustion are the same as those produced by the sintering process. This means that Ni/MgO catalyst precursors can be obtained by the self-propagating combustion but without high temperature sintering. MgO-based NiO/MgO solid solution, which is difficult to reduce, may result from NiO diffusion into the MgO lattice as temperature increases. The results show that the method takes great advantage of simplicity of the apparatus and synthesis process in which the particle size of Ni/MgO can be controlled, making it suitable for syntheses of the catalysts of carbon nanofibres.

### Acknowledgements

This work was supported by the Creative Research Group of the National Science Foundation of China (2005383) and the Foundation of the Ministry of Education of China for Returned Scholars (50721003).

### References

- [1] YOON Y.J., BAIK H.K., *Diam. Relat. Mater.*, 10 (2001), 1214.
- [2] RODRIGUEZ N.M., *J. Mater. Res.*, 8 (1993), 3233.
- [3] JUNG H.S., KIM H., AHN J.P., PARK J.K., *Met. Mater. Int.*, 10 (2004), 199.
- [4] ISMAGILOV Z.R., SHIKINA N.V., KRUCHININ V.N., RUDINA N.A., USHAKOV V.A., VASENIN N.T., VERINGA H.J., *Catal. Today*, 102 (2005), 85.
- [5] LIM S., YOON S.H., KORAI Y., MOCHIDA I., *Carbon*, 42 (2004), 1765.
- [6] OCHOA-FEMANDEZ E., CHEN D., YU Z.X., TOTDAL B., RONNING M., HOLMEN A., *Catal. Today*, 102 (2005), 45.
- [7] TAKENAKA S., KOBAYASHI S., OGIHARA H., OTSUKA K., *J. Catal.*, 217 (2003), 79.
- [8] ZHENG G.B., KOUDA K., SANO H., UCHIYAMA Y., SHI Y.F., QUAN H.J., *Carbon*, 42 (2004), 635.
- [9] CHEN P., ZHANG H.B., LIN G.D., HONG Q., TSAI K.R., *Carbon*, 35 (1997), 1495.
- [10] BRADFORD M.C.J., VANNICE M.A., *Appl. Catal. A*, 14 (1996), 73.
- [11] LIANG Y., FAN J., JIA Z.J., *Chin. J. Appl. Chem.*, 24 (2007), 626.
- [12] BRADFORD M.C.J., VANNICE M.A., *Catal. Rev. Sci. Eng.*, 41 (1999), 1.
- [13] ZHENG X.U., LIU C., ZHANG J.Y., ZHAO J.B., *Chin. J. Catal.*, 21 (2000), 309.
- [14] SUO Z.H., XU X.F., MA H.X., *Chin. J. Catal.*, 21 (2000), 411.
- [15] RUCKENSTEIN E., HU Y.H., *Appl. Catal. A*, 154 (1997), 185.
- [16] CHEN P., ZHANG H.B., LIN G.D., CHAI Q.R., *Chem. J. Chin. Uni.*, 5 (1998), 100.
- [17] CHEN C.W., CAI Y., LIN Y.Z., LIN J.D., CHEN H.B., LIAO D.W., *Chin. J. Chem. Phys.*, 15 (2002), 123.

- [18] LI F.Y., PENG N.C., WANG M.W., WEI R.Z., *J. Mol. Catal.*, 17 (2003), 65.
- [19] WANG Y.H., LIU H.M., XU B.Q., *Chin. J. Catal.*, 26 (2005), 1117.
- [20] BOWEN R., DERBY B., *British Ceram. Trans.*, 96 (1997), 25.
- [21] WANG X.H., ZHOU Y.C., *Chin. J. Mater. Res.*, 15 (2001), 387.
- [22] HUANG J., ZHUANG H., LI W., *Mater. Res. Bull.*, 38 (2003), 149.
- [23] ZHANG E.L., TANG Y.H., ZHANG Y., GUO C., *Physica E*, 41 (2009), 655.
- [24] YOSHIDA T., TANAKA T., YOSHIDA H., FUNABIKI T., YOSHIDA S., *J. Phys. Chem.*, 100 (1996), 2302.

*Received 27 September 2009*

*Revised 8 November 2010*

# Synthesis and characterization of magnetite nanoparticles by a simple solvothermal method

P. OU, G. XU, C. XU, Y. ZHANG, X. HOU, G. HAN\*

State Key Laboratory of Silicon Materials, Department of Materials Science and Engineering,  
Zhejiang University, Hangzhou 310027, P.R. China

Magnetite ( $\text{Fe}_3\text{O}_4$ ) nanoparticles were successfully synthesized via a simple solvothermal process and characterized by X-ray diffraction, field emission scanning electron microscopy, and physical property measurement system (PPMS). It was found that the diameters of as-synthesized  $\text{Fe}_3\text{O}_4$  nanoparticles became larger as the reaction temperature increased, and the magnetic properties of these nanoparticles could change from ferrimagnetic to superparamagnetic with the decrease in particle size. A possible mechanism for the formation of  $\text{Fe}_3\text{O}_4$  nanoparticles has also been proposed.

Keywords:  *$\text{Fe}_3\text{O}_4$  nanoparticles; ethylene glycol; solvothermal process; magnetic properties*

## 1. Introduction

On the nanometer scale, properties of materials are dramatically different from their bulk counterparts [1]. Unique properties of nanomaterials arise from a large fraction of atoms residing on the surface of these particles and the finite number of atoms in each crystalline core [2]. Magnetite ( $\text{Fe}_3\text{O}_4$ ), as a common ferrite with a cubic inverse spinel structure, exhibits unique electric and magnetic properties, based on the transfer of electrons between  $\text{Fe}^{2+}$  and  $\text{Fe}^{3+}$  ions at the octahedral sites [3]. In recent years, the synthesis of nanostructured magnetic materials, especially  $\text{Fe}_3\text{O}_4$  nanoparticles, has become a particularly important research field and is attracting growing interest [4–6]. Besides practical applications in industry such as in catalysis, ceramics, energy storage, magnetic data storage, and ferrofluids [7, 8], magnetite nanoparticles have already been applied in clinical diagnosis and medicine transporters [9].

Conventionally,  $\text{Fe}_3\text{O}_4$  nanoparticles are produced via aqueous or organic solution synthesis. A hydrothermal reaction of  $(\text{NH}_4)_2\text{SO}_4 \cdot \text{FeSO}_4 \cdot 6\text{H}_2\text{O}$  in the presence of hydrazine produces  $\text{Fe}_3\text{O}_4$  particles of about 70 nm [10]. Other aqueous solution syntheses such as coprecipitation of ferrous ( $\text{Fe}^{2+}$ ) and ferric ( $\text{Fe}^{3+}$ ) ions or by thermal de-

---

\*Corresponding author, e-mail: opyp@163.com

composition of alkaline solution of  $\text{Fe}^{3+}$  chelate in the presence of hydrazine and by sonochemical decomposition of hydrolyzed Fe(II) salt have also been developed in recent years. But none of these synthesis methods could be used for the fabrication of nanoparticles smaller than 20 nm and with a satisfactory size distribution [11–13]. An organic solution phase decomposition route has been widely used in iron oxide nanoparticle synthesis, and decomposition of  $\text{Fe}(\text{cup})_3$ ,  $\text{Fe}(\text{acac})_3$ , or  $\text{Fe}(\text{CO})_5$  followed by oxidation can lead to high quality monodisperse  $\gamma\text{-Fe}_2\text{O}_3$  nanoparticles [14–16], which usually requires relatively higher temperatures and a complicated operation. The solvothermal process is one of the successful methods for growing crystals in which the grains formed have a better crystallinity than those obtained with other methods, and it has been used to obtain  $\text{Fe}_3\text{O}_4$  fine particles with highly uniform sizes. Gao et al. used  $\text{Fe}(\text{acac})_3$  as a precursor to fabricate magnetite nanoparticles with the diameter below 20 nm which can be controlled easily through tailoring surfactants under solvothermal conditions [17]. Yan et al. prepared size controlled  $\text{Fe}_3\text{O}_4$  nanoparticles via the solvothermal method by using mixed surfactants of SDS and PEG as protective reagents. The sizes of the nanoparticles can be varied from 15 nm to 190 nm by adjusting some experimental parameters such as the reaction time, initial concentration of reactants, and the molar ratio of reactant to protective reagents, etc. [18]. However, even though they produce highly crystalline and uniformly sized magnetic nanoparticles, these synthesis routes cannot be applied to large scale economic production because they usually require complicated operations and sometimes expensive/toxic reagents. Herein, we present a simple surfactant-free solvothermal process to synthesize  $\text{Fe}_3\text{O}_4$  nanoparticles employing  $\text{Fe}(\text{NO}_3)_3 \cdot 9\text{H}_2\text{O}$  and KOH as the starting materials, ethylene glycol as the solvent. Reduction of the  $\text{Fe}^{3+}$  by ethylene glycol is expected. The size of the as-synthesized magnetite nanoparticles can be controlled easily through adjusting reaction temperature in the ethylene glycol system. Magnetic properties of the  $\text{Fe}_3\text{O}_4$  nanoparticles synthesized at various temperatures were also investigated.

## 2. Experimental

Chemical reagents used in the present work were: iron nitrate ( $\text{Fe}(\text{NO}_3)_3 \cdot 9\text{H}_2\text{O}$ ), potassium hydroxide (KOH) and ethylene glycol ( $\text{C}_2\text{H}_6\text{O}_2$ ). All the chemicals were of analytical grade.

A typical synthesis procedure was as follows: 4.85 g  $\text{Fe}(\text{NO}_3)_3 \cdot 9\text{H}_2\text{O}$  and 2.46 g KOH were separately dissolved in 10  $\text{cm}^3$  of ethylene glycol. Then the mixed solution was stirred vigorously for 10 min. The resulting mixture was loaded into a 50  $\text{cm}^3$  Teflon lined autoclave, which was then filled with ethylene glycol up to 80% of the total volume. The autoclave was sealed and maintained at a certain temperature which was controlled from 200 °C to 250 °C for 24 h. Finally, it was cooled down to room temperature naturally. The products were washed several times with deionized water

and absolute ethanol to remove any impurities, and then dried at 60 °C for 6 h for characterization.

The as-prepared powder samples were characterized by X-ray powder diffraction (XRD) using a Rigaku D/max-RA X-ray diffractometer (Rigaku, Tokyo, Japan) with  $\text{CuK}_\alpha$  radiation ( $\lambda = 1.5406 \text{ \AA}$ ). Field emission scanning electron microscopy (FESEM) images were obtained from a SIRION FESEM (FEI, Eindhoven, the Netherlands). Magnetization was measured by using a physical property measurement system (PPMS-9T, Quantum Design, San Diego, CA).

### 3. Results and discussion

Figure 1 shows the XRD patterns of the samples formed by the solvothermal process and held at various temperatures for 24 h. Curve 1a displays the XRD pattern of the sample prepared by the solvothermal reaction at 200 °C. Obviously, all the peaks can be indexed to a pure phase  $\text{Fe}_3\text{O}_4$  with a cubic inverse spinel structure belonging to the  $Fd3m$  space group, fully consistent with the reported data (JCPDS: 85-1436). The XRD pattern of the sample synthesized at 250 °C is shown in Fig. 1, curve b. All the diffraction peaks could also be indexed to pure phase  $\text{Fe}_3\text{O}_4$ , and no impurities were detected. In correspondence with the increase in the reaction temperature, from 200 °C to 250 °C, the peaks became stronger and sharper. This indicates that an increase in temperature would promote evolution and crystallization of magnetite.

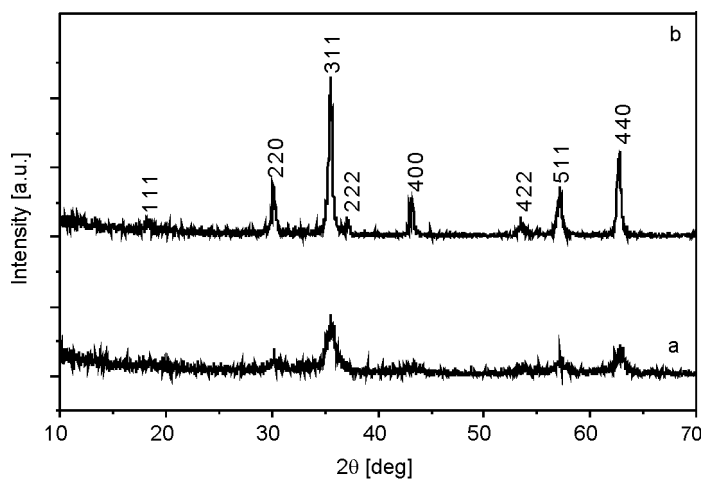


Fig. 1. X-ray diffraction patterns of the solvothermally synthesized samples at: a) 200 °C, b) 250 °C for 24 h

Figures 2a and 2b show the SEM images of samples solvothermally treated at 200 °C and 250 °C for 24 h, respectively. As shown in Fig. 2a, the powder consists of

uniform spherical nanoparticles with an average diameter of about 12 nm. However, when the solvothermal temperature was promoted to 250 °C, considerable changes in the diameter of Fe<sub>3</sub>O<sub>4</sub> crystallites could be found. As shown in Fig. 2b, the increased temperature resulted in uniform spherical Fe<sub>3</sub>O<sub>4</sub> particles, having an average size of about 53 nm, implying that a relatively higher temperature would promote crystallization of the magnetite phase. These observations are highly consistent with the above XRD results. The larger particle sizes of crystals prepared at higher temperature can be attributed to the (natural) dynamics of crystal nucleation.

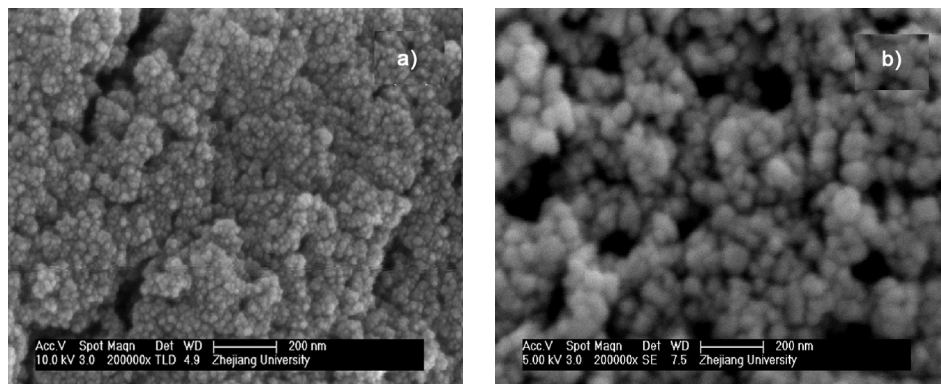
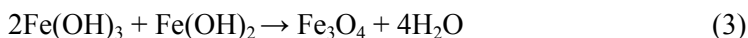
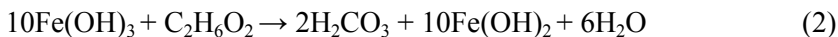


Fig. 2. Scanning electron microscopy images of the solvothermally synthesized Fe<sub>3</sub>O<sub>4</sub> powders at: a) 200 °C, b) 250 °C for 24 h

In our experiment, Fe(NO<sub>3</sub>)<sub>3</sub>·9H<sub>2</sub>O and KOH were dissolved in ethylene glycol, and then Fe(OH)<sub>3</sub> fast precipitated. Ethylene glycol, a strong reducing agent with a relatively high boiling point [19–24], served as both a solvent and reducing agent. Fe(OH)<sub>2</sub> was obtained through reduction of Fe(OH)<sub>3</sub> with ethylene glycol in the solvothermal process. Due to this treatment at 200 °C or 250 °C, Fe(OH)<sub>3</sub> and newly produced Fe(OH)<sub>2</sub> formed more stable Fe<sub>3</sub>O<sub>4</sub> phase in high alkaline solutions (pH higher than 12). From the above analysis, the corresponding possible reaction describing the formation of the Fe<sub>3</sub>O<sub>4</sub> nanoparticles can be expressed by the following equations:



The magnetization of the as-prepared samples under magnetic field at room temperature was also investigated. The magnetization curves (Fig. 3a) do not display hysteresis, the coercivity field and remnant magnetization cannot be detected from the curves, indicating that Fe<sub>3</sub>O<sub>4</sub> nanoparticles synthesized by the solvothermal process at 200 °C have superparamagnetic properties. The magnetization curve (Fig. 3b) showed

ferrimagnetic-like properties and the bulk-like behaviour was observed. The coercive field is 109.7 Oe and the remnant magnetization is 13.6 emu/g. This result is in agreement with the data reported by Sun et al. [25].

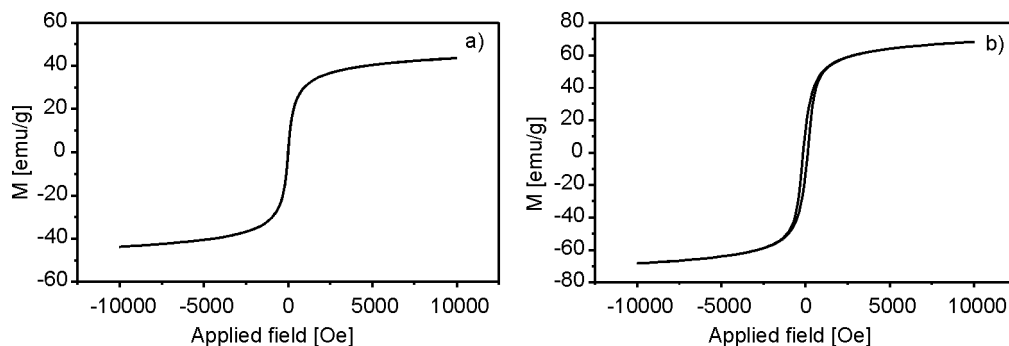


Fig. 3. The magnetization curves recorded at room temperature for the solvothermally synthesized  $\text{Fe}_3\text{O}_4$  nanoparticles at: a) 200 °C, b) 250 °C for 24 h

From the magnetization curves (Figs. 3a, b), we can also see that the saturation magnetization ( $M_s$ ) of the  $\text{Fe}_3\text{O}_4$  nanoparticles increases from 43.60 to 68.82 emu/g when the sizes of magnetite increase in accordance with the rise in solvothermal temperature, from 200 °C to 250 °C. The magnetic properties of the as-synthesized  $\text{Fe}_3\text{O}_4$  nanoparticles change when the particle size is decreased. This can be attributed to the significant size effect [26]: for particles of very small size, anisotropy energy is lower than the heat disturbance energy of ions, thus magnetization has no strong orientation in a particular direction, and the movement of the ions is random. Consequently, the sample should exhibit superparamagnetic properties, like a paramagnetic body. As the nanoparticle size increases, the anisotropy energy barriers increase accordingly, and superparamagnetic behaviour is replaced by ferrimagnetism.

## 4. Conclusions

A simple solvothermal method for synthesizing  $\text{Fe}_3\text{O}_4$  nanoparticles has been presented. XRD and SEM data for the  $\text{Fe}_3\text{O}_4$  nanoparticles synthesized by the solvothermal process showed that increasing the reaction temperature would improve the evolution and crystallization of  $\text{Fe}_3\text{O}_4$  nanoparticles. A one step, low-cost, surfactant free method described in the paper is suitable for large-scale production. It may also be employed for the preparation of other kinds of inorganic nanoparticles.

## Acknowledgements

This work was supported by the Chinese National Foundation of Natural Science Research (50452003).

## References

- [1] YANG T.Z., SHEN C.M., YANG H.T., XIAO C.W., XU Z.C., CHEN S.T., SHI D.X., GAO H.J., *Surf. Interface Anal.*, 38 (2006), 1063.
- [2] PUNTES V.F., KRISHNAN K.M., *Appl. Phys. Lett.*, 78 (2001), 2187.
- [3] CORNELL R.M., SCHWERTMANN U., *The Iron Oxides: Structure, Properties, Reactions, Occurrence and Uses*, VCH Publisher, New York, 1996.
- [4] YANG T., SHEN C., LI Z., ZHANG H., XIAO C., CHEN S., XU Z., SHI D., LI J., GAO H., *J. Phys. Chem. B*, 109 (2005), 23233.
- [5] MA D., GUAN J., NORMANDIA F., DENOMMEE S., ENRIGHT G., VERES T., SIMARD B., *Chem. Mater.*, 18 (2006), 1920.
- [6] ARRUEBO M., GALAN M., NAVASCUES N., TELLEZ C., MARQUINA C., IBARRA M.R., SANTAMARIA J., *Chem. Mater.*, 18 (2006), 1911.
- [7] BEYDOUN D., AMAL R., LOW G.K.-C., MCEVOY S., *J. Phys. Chem. B*, 104 (2000), 4387.
- [8] RAJ K., MOSKOWITZ R., *J. Magn. Magn. Mater.*, 85 (1900), 233.
- [9] FU L., DRAVID V.P., JOHNSON D.L., *Appl. Surf. Sci.*, 181 (2001), 173.
- [10] LI Y.D., LIAO H.W., QIAN Y.T., *Mater. Res. Bull.*, 33 (1998), 841.
- [11] SAPIESZKO R.S., MATIJEVIC E., *J. Colloid Interface Sci.*, 74 (1980), 405.
- [12] VIJAYAKUMAR R., KOLTYPIN Y., FELNER I., GEDANKEN A., *Mater. Sci. Eng.*, A286 (2000), 101.
- [13] FRIED T., SHEMER G., MARKOVICH G., *Adv. Mater.*, 13 (2001), 1158.
- [14] ROCKENBERGER J., SCHER E.C., ALIVISATOS P.A., *J. Am. Chem. Soc.*, 121 (1999), 11595.
- [15] HYEON T., LEE S.S., PARK J., CHUNG Y., NA H.B., *J. Am. Chem. Soc.*, 123 (2001), 12798.
- [16] SUN S.H., ZENG H., *J. Am. Chem. Soc.*, 124 (2002), 8204.
- [17] HOU Y.L., YU J.F., GAO S., *J. Mat. Chem.*, 13 (2003), 1983.
- [18] YAN A.G., LIU X.H., QIU G.Z., WU H.Y., YI R., ZHANG N., XU J., *J. Alloys Compd.*, 458 (2008), 487.
- [19] PENG Q., DONG Y.J., LI Y.D., *Angew. Chem. Int. Ed.*, 42 (2003), 3027.
- [20] PENG Q., XU S., ZHUANG Z.B., WANG X., LI Y.D., *Small.*, 1 (2005), 216.
- [21] SUN X.M., LI Y.D., *Angew. Chem. Int. Ed.*, 43 (2004), 3827.
- [22] SUN X.M., LI Y.D., *Angew. Chem. Int. Ed.*, 43 (2004), 597.
- [23] WANG J.W., WANG X., PENG Q., LI Y.D., *Inorg. Chem.*, 43 (2004), 7552.
- [24] ZHANG Y., LI Y.D., *J. Phys. Chem. B*, 108 (2004), 17805.
- [25] SUN S.H., ZENG H., ROBINSON D.B., RAOUX S., RICE P.M., WANG S.X., LI G.X., *J. Am. Chem. Soc.*, 126 (2004), 273.
- [26] ZHANG L.D., *Nanometer materials and nanometer structure*, Science Press, Beijing, 2001.

Received 23 October 2009

Revised 18 April 2010

# Room temperature ferromagnetism in Si nanocaps on self-assembled glass beads

Y.C. CHI<sup>1\*</sup>, Y. LIU<sup>2</sup>

<sup>1</sup>Institute of Materials Engineering, National Taiwan Ocean University,  
Keelung, 20224 Taiwan, Republic of China

<sup>2</sup>Institute of Physics, Academia Sinica, Taipei, 11529 Taiwan, Republic of China

Based on self-assembly techniques, Si layers of various thicknesses were deposited on glass bead arrays of various dimensions. The experimental results support the view that the self-assembled glass beads of small sizes (i.e., 10 and 20 nm in diameter), covered with a Si layer below 5 nm in thickness, can induce ferromagnetism. Regularity in the saturation magnetization confirms that the ferromagnetic-like behaviours heavily depend on both the size of the glass beads as well as the thickness of Si nanocaps. Maximum magnetization (750 emu/cm<sup>3</sup>) was found in the 20 nm glass bead template on which was deposited an ultra-thin 1 nm Si layer. We suggest that the quantum confinement mechanism helps to promote the unpaired electrons, which interact with neighbouring counterparts through the tunnelling effect and, thus, contribute to room temperature ferromagnetism.

Keywords: *ferromagnetism; nanosphere lithography; quantum confinement; exciton Bohr radius; tunneling effects*

## 1. Introduction

Ferromagnetism is one of the most important quantum-mechanical phenomena in atomic systems. Only atoms with partially filled shells (i.e., unpaired spins) can experience a net magnetic moment in the absence of an external field. However, in recent years, many developments in systems such as CaB<sub>6</sub> [1], HfO<sub>2</sub> [2], or special forms of carbon [3] have been reported as having magnetic order above room temperature. Moreover, efforts have concentrated on studying the onset of the nanoscale systems. The reduced sizes and dimensions of certain materials have given rise to a renewed scientific interest in producing magnetism in systems that are originally non-magnetic in their bulk state [4–7]. Quantum magnetism has become one of the most challenging areas of condensed matter and materials physics. More recently, Gari-

---

\*Corresponding author, e-mail: chiyc@aec.gov.tw

taonandia et al. reported that nanoparticles of Au, Ag, and Cu of the size of 2 nm can exhibit magnetic behaviour at ambient temperature [8]. Liou et al. reported inspiring ferromagnetic findings in Ge quantum dots (QDs) [9, 10]. Those studies demonstrate the existence of ferromagnetism without the contribution of magnetic transition metals. In addition, theories such as that of Lieb and Kagome, have been introduced in order to predict the possibilities of flat-band ferromagnetism in quantum dot arrays [11–14]. However, even though many investigations on the general physical properties of Si have been extensively reported, no ferromagnetism has ever been ascribed to Si, due to its intrinsic behaviour and bulk structures, leaving the study of silicon as the last virgin territory of research into magnetism, and which still needs to be fully explored.

The discovery of room-temperature visible photoluminescence in Si has been confirmed [15, 16]. The size dependence of the energy gap of Si nanostructures has also been discussed extensively [17–19]. The quantum confinement effect, resulting in a blue shift of the energy gap with decreasing size, is widely believed to be responsible for the novel properties. This strongly implies that when Si has the form of low-dimensional structures such as Si QDs, its physical properties are quite different from those of its bulk state. Furthermore, Ren et al. show that a Si cluster of 4.9 nm in diameter has virtually the same band gap and density of states as a bulk Si crystal [20]. Recently, Yamamoto et al. observed that Si clusters in SiO<sub>2</sub> glass film matrices with average diameters of 3, 4, and 5.1 nm exhibit quantum confinement effects [21]. Moreover, Si has an exciton Bohr radius ( $a_{\beta}$ ) of 4.9 nm [22], thus, if nanoscale Si can be involved in the formation of ordered magnetic states beneath the dimension of ca. 5 nm, it will become one of the most promising directions for magnetism research.

One simple self-assembly approach, i.e. nanosphere lithography, is introduced to control the placement of the Si layers on top of the nanospheres. This technique is an effective method of growing large area and well ordered arrays. With the aid of nanosphere lithography, a closely-packed, hexagonal array can be easily formed, in which triangular voids exist among any three nanospheres that are in physical contact with each other. When a Si layer is deposited on the substrate, many hemispherical Si nanocaps which nicely mimic the shapes of the nanospheres underneath are expected to form due to the masking effect. Part of the Si flux may penetrate through the voids and accumulate on the surface of the underlying substrate. It is worth noting that the masking effect normally decreases with the size of the nanospheres, thus the evaporated Si flux cannot easily pass through the increasingly ultrasmall triangular voids. As a result, the Si flux would seal off the voids and, further, coalescence to form a continuous film on top of the template.

## 2. Experimental

In this experiment, glass beads of four sizes (i.e., 10, 20, 50, and 100 nm in diameters) are obtained, which were diluted in a solution of surfactant Triton (Aldrich) and

well-mixed with isopropanol (1:1000 for small glass beads and 1:600 for large glass beads; ratio by volume). To make contaminant-free samples, the clearing procedure is strictly observed. Si substrates ( $7 \times 7 \times 0.5 \text{ mm}^3$ ) are first cleaned by the Piranha method. This cleaning process can remove organic and certain metal contaminants, and result in a hydrophilic surface. To degrease the surface of the substrate, solvent-based cleaning, with sequences of acetone, methanol and deionized water were used, each sonicated for 30 min. Solution was dipped and then spin-coated on Si substrate below 500 rpm (Chemat Tech., KW-4 A). High-purity intrinsic Si (99.9999%) is obtained as the deposition source. Si layers of various thicknesses (i.e., 1, 2, 3, 5, and 10 nm) were chosen to carry out thermal deposition onto various glass bead templates. A low deposition rate (0.1 nm/min) was selected during the evaporation process, which was performed under the pressures of  $1 \times 10^{-7}$  Torr. Energy dispersive spectroscopy (EDS) was used to investigate the impurities. Within the detection limit (0.1%) of EDS, neither intact Si targets (bulk form) nor deposited samples (layer form) indicate the presence of magnetic contaminants. The magnetization measurements of the samples were carried out by using a vibrating sample magnetometer (VSM) at room temperature. Both atomic force microscopy (AFM) and field emission scanning electron microscopy (FESEM) were chosen to investigate the morphological evolutions of the Si samples.

### 3. Results and discussion

Based on the above, a scheme is proposed: self-assembled glass beads covered with Si layers of various thicknesses are introduced, as schematically shown in Fig. 1a. If the

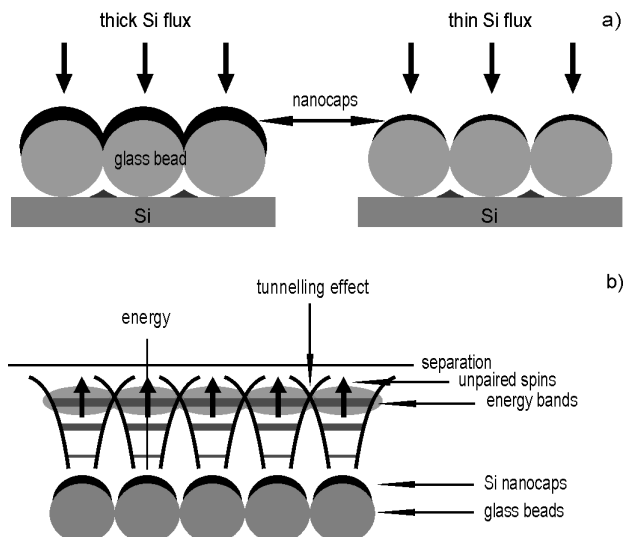


Fig. 1. An illustrative scheme of Si deposition characterized by thick and thin fluxes onto a glass bead arrays (a) and a simplified scheme introducing an ideal nano-scale ferromagnetic system of Si (b)

deposited Si layer is thick enough, all forms of the glass beads will be wrapped by Si. In this case, good hysteresis loops are not expected to occur, because a substantial quantity of Si in the initial deposition layer becomes transferred to the film. On the other hand, for light deposition, appropriate hemispherical nanocaps are expected to form. We suggest that when the Si nanocaps are sufficiently small, degenerated energy levels split into discrete levels as a consequence of the quantum confinement effects. At such ultra-small dimensions, unpaired spins are likely to contribute to the magnetic moments, which interact with neighbouring counterparts through the tunnelling effect and then initiate the quantum ferromagnetism. However, in the extreme case (i.e., the 10 nm glass bead array), we recall that if the voids are too small, they may extensively block the penetration of the Si flux, due to the fading of the masking effect. Many enlarged nanocaps are expected to form all over the template and effectively degrade ferromagnetism. Therefore, on the contrary, they may not necessarily show the largest magnetizations. Yet on top of the large glass beads (e.g., 100 nm in diameter), thin but larger nanocaps are not expected to display strong ferromagnetism either, for both the enlarged nanocaps (far beyond  $a_\beta$ ) and the voids may seriously impair the quantum confinement effects. In Figure 1b, a schematic diagram illustrates the discrete energy bands that are involved, confined energy barriers, unpaired spins, and so forth, in an ideal nanoscale Si system (i.e., a template comprised of small uniform glass beads and thin Si nanocaps).

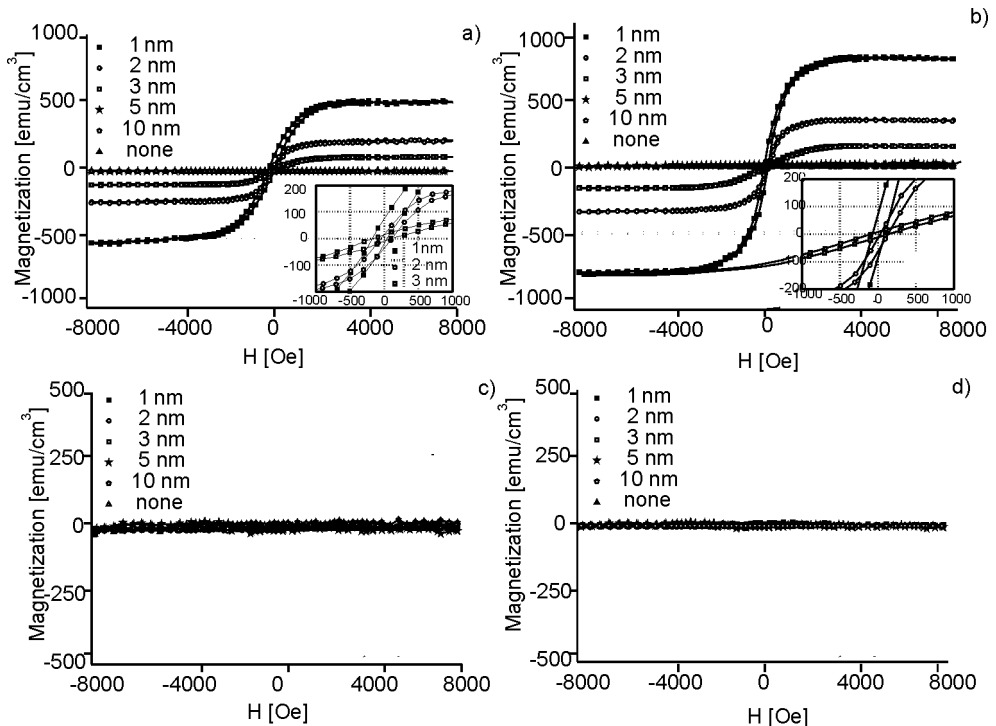


Fig. 2. Room temperature magnetization loops (per unit volume) vs. external magnetic field of: a) 10 nm, b) 20 nm, c) 50 nm, and d) 100 nm glass bead arrays deposited with various Si layers

Figure 2 shows the room temperature magnetization loops (per unit volume) vs. the external magnetic fields of the samples (i.e., 10, 20, 50, and 100 nm glass bead arrays deposited with various Si layers) without the diamagnetic contribution of the substrate. We find that in Figs. 2a, b, the 10 nm and 20 nm glass bead templates deposited with various Si layers show ferromagnetic hysteresis loops with amazing regularities. As the deposited Si layer increases from 1 to 5 nm, the saturation magnetization consistently decreases from the maximum value down to null. The highest magnetization ( $\sim 750$  emu/cm<sup>3</sup>) was found in the 20 nm glass bead array on which was deposited an ultra-thin 1 nm Si layer. The insets show the magnification of the hysteresis loops of the 10 nm and 20 nm templates, each of which were deposited, at low field strength, with 1, 2, and 3 nm Si layers. However, if the glass bead arrays are large (i.e., 50 nm or 100 nm in diameter), then diamagnetism always occurs, regardless of the thickness of the Si layer deposited on the surfaces of the beads, as shown in Figs. 2c,d. We found no significant magnetic signals with such samples.

For a clear description, we take two representative arrays, i.e. 20 nm and 100 nm glass bead arrays. Si layers of various thicknesses were deposited on each of these types of arrays to illustrate the comparative performance in ferromagnetism. The former type of array is selected for its better quantum confinement mechanism in magnetic presentations, whereas the latter is chosen because its dimension is far greater than  $a_\beta$  and because it exhibits the worst magnetization. By using FESEM, we carefully investigate the morphological evolutions of the samples. In Figure 3a, which shows the micrograph of a 20 nm bead array deposited with 1 nm Si, we can directly observe that these nanocaps, lying on top of the glass beads, have good shapes. When these nanocaps are close enough to each other, room temperature ferromagnetism occurs. However, due to weak communications (i.e., tunnelling effects) among these unpaired spins, the squareness of the hysteresis loop cannot be broadened dramatically. In Figure 3b, the fuzzy junctions among the glass beads can barely be observed for 2 nm Si coverings upon the template. The magnetization was found to be reduced to 300 emu/cm<sup>3</sup>. Yet as the thickness of the Si layer increases to 3 nm, apparent junctions emerged in the vicinity of the nanocaps, as shown in Fig. 3c. Correspondingly, poor magnetization (ca. 140 emu/cm<sup>3</sup>) arises at this stage, which implies that the presence of homogeneous Si junctions does not enhance ferromagnetism, but spoils it. In Figure 3d, when the Si layer increases to 5 nm, we can see a clear continuous film formed on top of the template. The magnetization undoubtedly drops to null. Similarly, in Fig. 3e, when the Si layer increases to 10 nm, we get the same diamagnetic result as that which occurs with the 5 nm Si layer. No hysteresis loops can be detected, just as expected. The drops in the saturation magnetizations basically comply with the increasing thickness of the nanocaps, for layer thicknesses below 5 nm. Once the nanocaps thicken to 5 nm or above, they immediately lose all their ferromagnetism.

For the largest glass bead arrays (i.e., 100 nm in diameter), Figs. 3f, g show the micrographs, barely visible, of the 1 nm and 2 nm Si nanocaps on top of the templates, respectively. Likewise, as the thickness increases to 3 nm, fuzzy junctions with

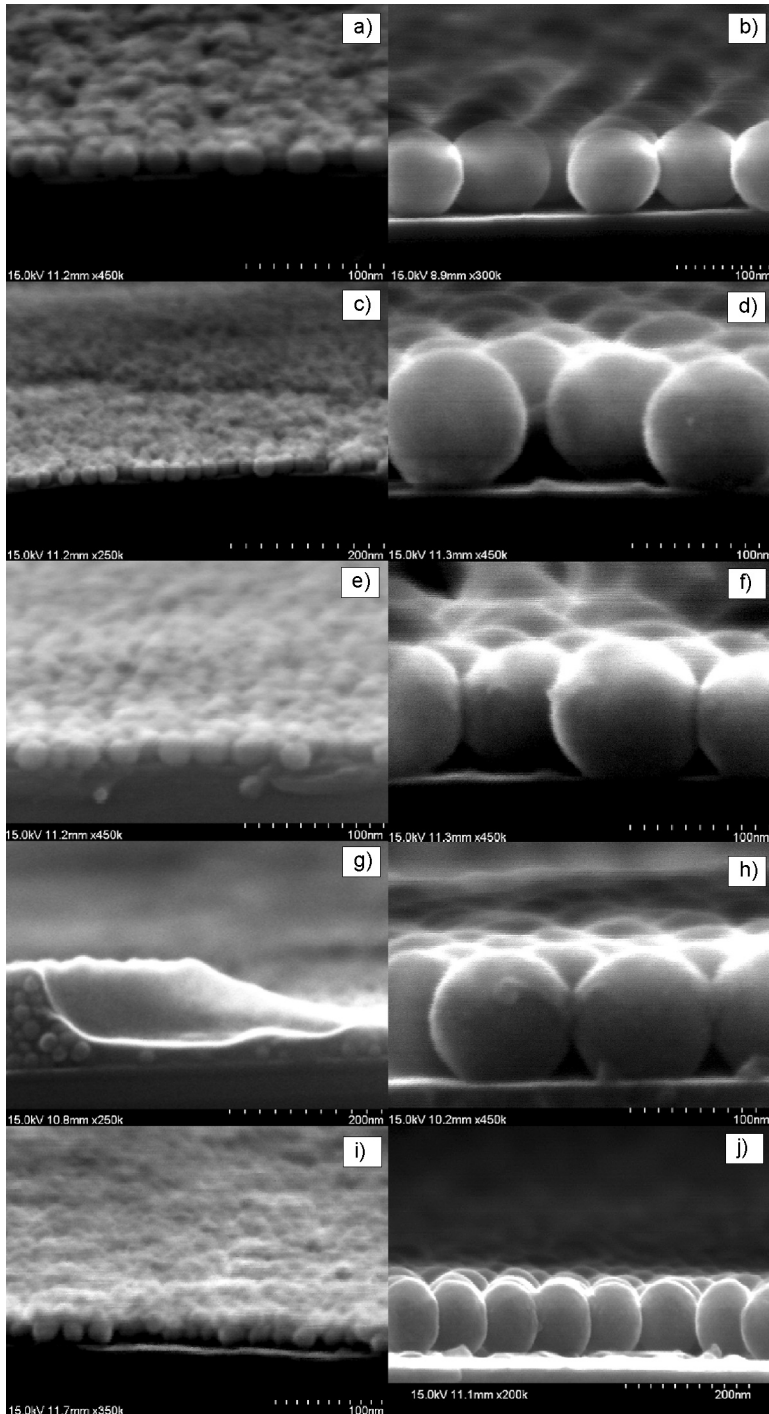


Fig. 3. Cross-sectional FESEM micrographs of various Si layers on 20 nm glass bead arrays (a)–(e), and on 100 nm glass bead arrays (f)–(j)

nanocaps gradually appear, as shown in Fig. 3h. For thicker depositions (i.e., 5 nm and above), Figs. 3i, j illustrate the tendency of the Si flux to form coalescent nanocaps on the templates. Unfortunately, they are all diamagnetic. None of them exhibit the slightest ferromagnetism, due to thick coverings (thicknesses far greater than  $a_\beta$ ) on the beads and the prevalence of large voids on the substrate. They dynamically prevent the moment coupling, leading to null magnetism. Therefore, neither 1 nor 10 nm layers of Si deposited on the 100 nm glass bead arrays result in measurable magnetism.

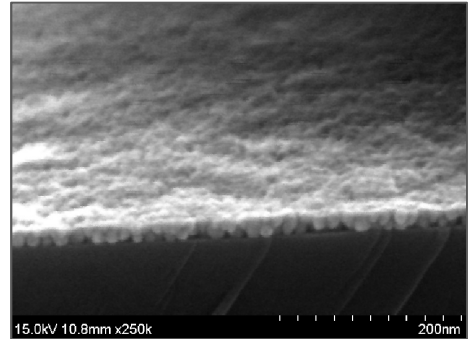


Fig. 4. Cross-sectional FESEM micrograph of 1 nm Si deposited on top of a 10 nm glass bead array

Initially, we expect to observe stronger magnetism in the 10 nm glass bead array deposited with thin nanocaps than that of its counterpart, i.e. the 20 nm glass bead array. But this does not happen at all. Upon re-examining the samples, we find that the 10 nm glass bead array deposited with a 1 nm Si layer suffers a coalescence problem, as shown in Fig. 4. Ties and junctions can be clearly seen on top of the beads. The fading of the masking effect helps in the formation of larger nanocaps, resulting in extensive magnetic degradation. On the other hand, the 20 nm glass bead template can induce the formation of many isolated, uniformly-distributed nanocaps. We hardly see any serious coalescence in the latter case, unless a thick Si layer redistributes itself. We speculate that if the voids are a suitable size, this will help Si flux to penetrate through without detrimental seal-off. Therefore, the magnetizations of the 10 nm glass bead arrays, whether they are deposited with 1, 2, or 3 nm thick layers of Si, are always inferior to those of the 20 nm glass bead arrays.

In view of the fact that the thin 1 nm Si nanocaps on the 20 nm glass bead array result in the largest saturation magnetization, we therefore claim that Si nanocaps can exhibit room temperature ferromagnetism provided that the optimum glass beads, with appropriately thin Si coverings, are in mutual contact. However, if the size of the glass beads increases above 50 nm and/or if the Si layer thickens above 5 nm, the magnetization quickly decreases to background levels (diamagnetism). This can be attributed to the following causes. Firstly, the dimension of the thin nanocaps having Si deposition layers of 1 or 2 nm thick, and lying on top of the 50 nm (or 100 nm) glass beads, far exceeds the quantum confinement edge (ca. 5 nm). Moreover, the long centre-to-centre distance of the beads and the prevalence of the large voids prohibit the occurrence of the exchange interactions, thereby leading to the smallest level of magnetization.

Secondly, a thick layer (e.g., 5 nm or 10 nm) deposited on any template will eventually transform into continuous film. A 5 nm thick Si layer is too thick to form isolated, quantum-sized nanocaps on top of the beads, regardless of the bead size (see Figs. 3d, i). AFM micrographs support this finding, as shown in Fig. 5. Significant coalescence (i.e., 5 nm Si) can be clearly observed on both the 20 nm glass bead array (Fig. 5a) as well as on the 100 nm glass bead array (Fig. 5b). This implies that thick Si layers always induce the least, or negligible, ferromagnetism. We suggest that the missing quantum confinement effects are responsible for the great loss of the induced ferromagnetism.

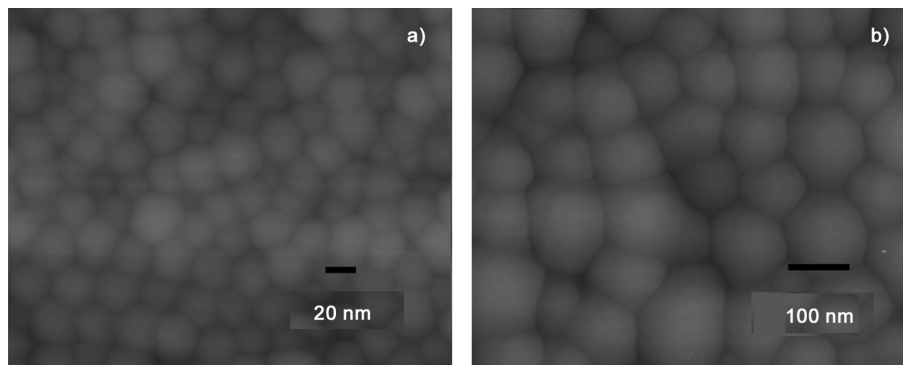


Fig. 5. AFM micrographs of (a) the 20 nm glass bead array and (b) the 100 nm glass bead array deposited with 5 nm Si, respectively

Magnetic impurities are always present, even though considerable precautions have been taken to preclude contaminants that might contribute to magnetic interference. However, impurities can be ruled out by considering the following facts: (1) the evidence of EDS examinations; (2) theoretical assessment [9]. For example, if there were a large amount of magnetic impurities of ca. 500 ppm (0.05%) in the samples, the maximum saturation magnetization per unit volume would be expected to be ca.  $0.5 \text{ emu/cm}^3$ , which is much smaller than the actual magnetization measurements of this study; (3) linear increment of the thickness of Si layer accompanies a corresponding decrement in the saturation magnetization. If significant magnetic impurities had been present, we would have measured ascending levels of magnetization corresponding to the increment in the layer thickness; and (4) all magnetic samples exhibited a spontaneous and continuous decay in magnetization strength when they were left to stand alone for a period of time. However, magnetic contaminants should maintain stable magnetism on the host material, unless an effective purge was carried out.

#### 4. Conclusions

Based on self-assembly techniques, glass bead arrays deposited with Si layers of various thicknesses (i.e., 1–10 nm) were investigated. The 10 nm and 20 nm glass bead arrays having Si deposition layers of various thicknesses induce ferromagnetic hysteresis loops with remarkable regularities. Maximum magnetization (ca.  $750 \text{ emu/cm}^3$ )

was found in the 20 nm glass bead array deposited with an ultrathin 1 nm Si layer. Regularity in saturation magnetizations confirms that the ferromagnetic-like Si nanocaps heavily depend on both the size of the glass beads as well as on the thickness of the Si layers. Quantum confinement on excitons in variously sized Si nanocaps has been proposed as the most reasonable explanation for the quantum ferromagnetism. The experimental results support the view that the quantum confinement mechanism helps to promote unpaired electrons which interact with neighbouring counterparts through the tunnelling effect, and then initiate the quantum ferromagnetism. However, the squareness of the hysteresis loops cannot be arbitrarily broadened, due to weak interactions among these unpaired spins.

In this study, we provided evidence for soft ferromagnetic behaviour in Si nanocaps at room temperature. It has been suggested that very small Si nanocaps exhibit a localized magnetism, in contrast to the diamagnetism characteristic of bulk Si. The possibility of controlling the magnetization might open up a wide area of research on quantum ferromagnetism. Ferromagnetic nano-scale Si systems might possibly be utilized and exploited.

#### Acknowledgements

This research has been partially supported by the Atomic Energy Council of Taiwan. The author acknowledges S.T. Chiou (ROCAEC), Y.M. Lan, C.L. Chen, C.S. Tsai and T.W. Chu (INER) for their expert support.

#### References

- [1] DORNELES L.S., VENKATESAN M., MOLINER M., LUNNEY J.G., COEY J.M.D., *Appl. Phys. Lett.*, 85 (2004), 6377.
- [2] COEY J.M.D., VENKATESAN M., STAMENOV P., FITZGERALD C.B., DORNELES L.S., *Phys. Rev. B*, 72 (2005), 024450.
- [3] ESQUINAZI P., HÖHNE R., *J. Magn. Magn. Mater.*, 290 (2005), 20.
- [4] HERNANDO A., SAMPEDRO B., LITRÁN R., ROJAS T.C., SÁNCHEZ-LÓPEZ J.C., FERNÁNDEZ A., *Nanotechnology*, 17 (2006), 1449.
- [5] DUTTA P., PAL S., SEEHRA M.S., ANAND M., ROBERTS C.B., *Appl. Phys. Lett.*, 90 (2007), 213102.
- [6] WANG W.C., KONG Y., HE X., LIU B., *Appl. Phys. Lett.*, 89 (2006), 262511.
- [7] SUBER L., FIORANI D., SCAVIA G., IMPERATORI P., PLUNKETT W.R., *Chem. Mater.*, 19 (2007), 1509.
- [8] GARITAONANDIA J.S., INSAUSTI M., GOIKOLEA E., SUZUKI M., CASHION J.D., KAWAMURA N., OHSAWA H., DE MURO I.G., SUZUKI K., PLAZAOLA F., ROJO T., *Nano Lett.*, 8 (2008), 661.
- [9] LIU Y., SHEN Y.L., *Adv. Mater.*, 20 (2008), 779.
- [10] LIU Y., SU P.W., SHEN Y.L., *Appl. Phys. Lett.*, 90 (2007), 182508.
- [11] MIELKE A., *J. Phys. A*, 24 (1991), L73.
- [12] LIEB E.H., *Phys. Rev. Lett.*, 62 (1989), 1201.
- [13] TASAKI H., *Phys. Rev. Lett.*, 69 (1992), 1608.
- [14] MOULTON B., LU J.J., HAJNDL R., HARIHARAN S., ZAWOROTKO M.J., *Angew. Chem. Int. Ed.*, 41 (2002), 2821.
- [15] TAKAGI H., OGAWA H., YAMAZAKI T., ISHIZAKI A., NAKAGIRI T., *Appl. Phys. Lett.*, 56 (1990), 2379.
- [16] CANHAM L.T., *Appl. Phys. Lett.*, 57 (1990), 1046.
- [17] WANG L.W., ZUNGER A., *J. Phys. Chem.*, 98 (1994), 2158.

- [18] YORIKAWA H., UCHIDA H., MURAMATSU S., J. Appl. Phys., 79 (1996), 3619.
- [19] KUX A., CHORIN M.B., Phys. Rev. B, 51 (1995), 17535.
- [20] REN S.Y., DOW J.D., Phys. Rev. B, 45 (1992), 6492.
- [21] YAMAMOTO M., HAYASHI R., TSUNETOMO K., KOHNO K., OSAKA Y., Jpn. J. Appl. Phys., 30 (1991), 136.
- [22] CULLIS A.G., CANHAM L.T., CALCOTT P.D.J., J. Appl. Phys., 82 (1997), 909.

*Received 20 June 2010*

# Modification of the 306 Edwards sputtering system for the reproducible fabrication of sensitive thin films

A. YOFFE<sup>1</sup>, V. SHELUKHIN<sup>2\*</sup>

<sup>1</sup>The Helen and Martin Kimmel Center for Nanoscale Science, Weizmann Institute of Science, PO Box 26, Rehovot, Israel

<sup>2</sup>Department of Materials and Interfaces, Weizmann Institute of Science, PO Box 26, Rehovot, Israel

Modifications to the 306 Edwards sputtering system have been discussed for the production of sensitive thin films, specifically amorphous pyroelectric perovskite films. For technical reasons, it is not possible to produce high quality thin films using standard sputtering systems. Furthermore, additional problems arise with the reproducibility of the films. The authors found that in unmodified sputtering systems, a general problem is that independent adjusting of the pressure in the chamber and the gas flow during the sputtering is not possible. Additional problems were low accuracy of gas ratio measurements, and high temperature radiation during sputtering which made impossible keeping the temperature conditions during deposition. Modifications to a standard set-up have been proposed and its operation has been checked. As a test-case, SrTiO<sub>3</sub> thin film samples were fabricated. Their high quality confirmed validity of the modifications.

Keywords: *Edwards sputtering; thin film; vacuum system*

## 1. Introduction

The 306 Edwards sputtering system has been available for users for over 20 years. However some problems have been encountered with the production of sensitive thin film using this system. These popular sputtering systems were produced by Edwards until 2009 [1] and are still being used in many science laboratories for high quality thin film deposition [2, 3], including universities such as Massachusetts Institute of Technology and University of California at Berkeley. A detailed description of this sputtering system will be found at the official site of Berkeley Microfabrication Laboratory [4]. These systems are very good for the ordinary sputtering of metals and films, which is non-sensitive to sputtering conditions. But the production of films that are dependent on the stoichiometric ratio is very problematic. For example, the repro-

---

\*Corresponding author, e-mail: Victor.Shelukhin@weizmann.ac.il

ducible preparation of amorphous thin films of  $\text{SrTiO}_3$ ,  $\text{BaZrO}_3$  and  $\text{BaTiO}_3$  by this sputtering system [5, 6], namely thin films which do not crystallize during sputtering, remains a complicated technical problem. The reasons are the inadequacy of component systems (the pressure controller, gas injection and flow monitoring systems) and the fact that the gas injection and pumping systems cannot be controlled independently. Consequently, the pressure and gas flow ratio readings for this sputtering system have a 15% measurement error. Therefore it is almost impossible to obtain films of high quality, because that would entail much stricter production requirements: an exact  $\text{O}_2/\text{Ar}$  flow ratio should be maintained under a stable pressure and strong gas flow. It should be noted that uncontrolled thermal variations of the wafer during sputtering is a problem which also influences the sample quality. The sputtering modifications we describe here establish a procedure for the reproducible fabrication of high quality thin films, and this has been difficult to achieve before now. We demonstrate the effectiveness of our approach by producing pyroelectric films of  $\text{SrTiO}_3$ , but we believe our scheme can be used in more general cases.

## 2. Sputter modification

The Auto 306 rf and dc sputter coater with a turbomolecular pump consists of the following major components: Seiko turbo pump, short FL50 chamber, Poppet high vacuum isolation valve, rotary pump, liquid nitrogen trap, single button automatic vacuum control with Penning and two Pirani gauges, shutters; dc source advanced energy, rf source Dressler, two EPM75 magnetrons Edwards. The system allows the production of metal and dielectric films under  $10^{-6}$  Torr base pressure.

The system auto 306 sputter has only three settings for the "Poppet" valve for the limitation of downstream: "Open", "Close" and "Process". The "Nupro" needle valves and Edwards "Pirani" vacuum gauges are used in the standard configuration to control the injection of gases into the sputtering system, for flow changes and pressure measurements. In order to obtain the requisite pressure in the chamber under "Process" mode, one has to change the gas flow. In other words there is no possibility of adjusting flow and pressure independently. As a result, with this sputtering system, there is a 15% measurement error for pressure and gas flow ratio readings. Therefore it is almost impossible to obtain films of high quality, because then an exact  $\text{O}_2/\text{Ar}$  flow ratio would have to be maintained, under a stable pressure and strong gas flow.

The following changes to the sputtering system (Fig. 1) were made:

1. Vacuum throttle valve (VAT series 61 butterfly control system) was added to enable selection, independently of the gas flow, of the pumping strength and the gas pressure in the chamber, in accordance with user requirements for experiments.
2. MKS baratron type 622A and PM3 pressure controller were added to the system, for pressure measurements and for controlling the throttle valve.
3. The needle valves were changed to MKS type 247D four channel readout – for manual flow changes and type 1179A mass flow controller for precise gas injections.



Fig. 1. Added instruments: MKS type 247D four channel readout and VAT PM3 pressure controller (a), butterfly VAT series 61 throttle valve (b), inside view of the sputtering system, new throttle valve is beneath a “Poppet” valve (in the ring) (c)

The introduced modifications allowed us to change the pressure in the chamber and the flow of each gas independently and, as a result, to obtain the measurement accuracy of 0.1–0.2% for the flow ratio, and 0.5–1.0% for the pressure. We find that the temperature of the sample during the sputtering is very significant, because the temperature of the wafer critically influences the crystallization of the sputtered layer during the sputtering process. Therefore, in order to minimize the heating of the samples, it was necessary to construct a special holder, placed in the vacuum system and having reliable components, and which has good thermal contact with the chamber or can facilitate the cooling of samples in another way. In our case, to reduce heat build-up in the samples during the sputtering process, Si wafers were placed in a special, massive sample holder equipped with a heat sink. The temperature of the samples was directly measured on the wafer in the control experiment, using irreversible thermometers “SPIRIG”. If the temperature of a sample during deposition was below 71 °C, amorphous layers of good quality were obtained, while if the temperature was higher than 143 °C, the films crystallized. If the temperature was between 71 °C and 143 °C, the samples were partially crystallized, depending on other parameters of experiments (thickness of SrTiO<sub>3</sub> layer, metals used for a bottom layer, etc).

### 3. Results and discussion

As a result of the modifications, reproducible, good quality films were obtained. More than 20 experiments were conducted, in each SrTiO<sub>3</sub> was sputtered onto Si sub-

strate or Si/SiO<sub>2</sub> wafer covered with metal (Cr and W). Highly doped 2 inch Si wafers with the resistivity of 0.2–20 Ω·cm were used. Kurt J. Lesker targets were applied of the aforementioned materials (Cr or W), of 99.99% purity, for metal sputtering in an Ar atmosphere under the pressure of  $1.2 \times 10^{-2}$  Torr and flow 2 standard cubic centimeters (sccm), in a dc mode, at 100 W power. The thicknesses of the metal layers were 150–200 nm. The sputtering of the SrTiO<sub>3</sub> films (using target – Semiconductor Materials, 99.9%, metal base) was done in an rf regime, without opening the chamber after metal deposition, in an Ar and O<sub>2</sub> atmosphere under  $3 \times 10^{-2}$  Torr and 12 sccm flow of each gas, 100 mm distance between the target and Si wafer (or metal covered SiO<sub>2</sub>/Si wafer). In the rf mode the power regime was 100–120 W and the thicknesses of the films were 65–120 nm. The base pressure in the chamber was  $(1-2) \times 10^{-6}$  Torr. The temperature of the samples was up to 60 °C.

The gradient heating procedure (pulling through a temperature gradient) was done after sputtering in the manner described in the paper [5], for film transfer to quasi-amorphous state and followed pyroelectric measurements [7].

More than 80% of wafers were sputtered with 65–120 nm SrTiO<sub>3</sub> films were useful after top 2×2 mm<sup>2</sup> metal contacts evaporation and lift-off process, for making pyroelectric measurements, and they exhibited pyroelectric properties. All the samples used had good stoichiometric ratios. The ceramic composition was identified by X-ray photoelectron spectroscopy (XPS). The data was acquired with an Axis-HS, Kratos analytical spectrometer. Exemplary data for one of the examined samples is presented in Table 1.

Table 1. XPS data for SrTiO<sub>3</sub> film on Cr/SiO<sub>2</sub>/Si

State	Peak	Atomic concentration [%]	Stoichiometric ratio*
As deposit	Ti 2p	14.94	1.0
	Sr 3d	15.31	1.0
	O 1s	50.72	3.3
After 100 s sputtering	Ti 2p	19.93	1.0
	Sr 3d	19.27	1.0
	O 1s	55.19	2.9
After 160 s sputtering	Ti 2p	22.03	1.1
	Sr 3d	19.60	1.0
	O 1s	54.95	2.8

\*Stoichiometric ratio data is normalized to the Sr content, data corresponds to Sr:Ti:O with 1:1:3 stoichiometric ratio within the limit of the measurement method error (10%)

These SrTiO<sub>3</sub> samples are examples of sensitive thin films because only good stoichiometric, amorphous films exhibit pyroelectric properties after gradient temperature pulling [8, 9]. Wafers sputtered with SrTiO<sub>3</sub> were divided into two sets of samples, and each individual sample had dimensions of 6×40 mm<sup>2</sup>; one set of samples was

used for checking certain physical properties such as refractive indices, stress and composition measurements etc. The other set, consisting of more than 30 samples, was used for pyroelectric measurements: typical pyroelectric raw data from several of these samples is presented in Fig. 2. As can be seen from this figure, a time-dependent pyroelectric signal, generated in response to laser pulses used for sample heating, was recorded.

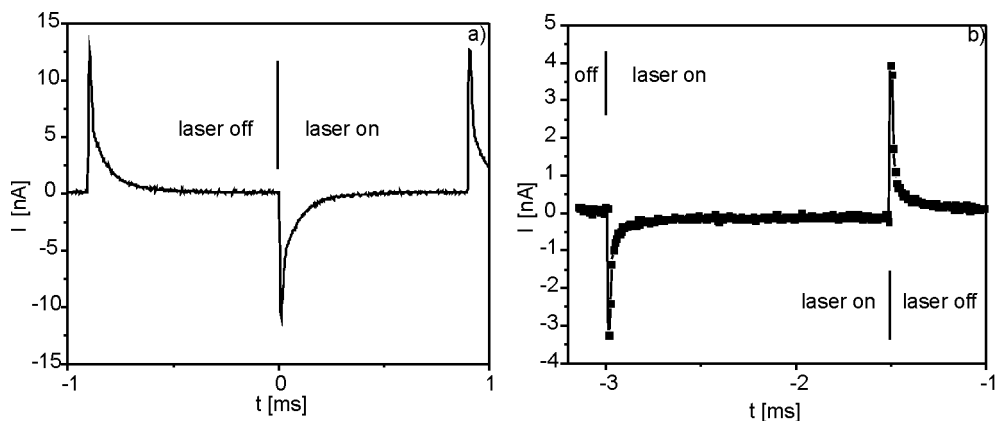


Fig. 2. Raw data from Tektronix TDS 7104 digital phosphor oscilloscope for several samples: a) Cr-SrTiO<sub>3</sub>-Cr, b) W-SrTiO<sub>3</sub>-W

Sr, Ti and O can form a variety of structures, perhaps SrTiO<sub>2</sub> [10], Sr<sub>2</sub>TiO<sub>4</sub> [11], SrTiO<sub>2.72</sub> [12], SrTiO<sub>3-x</sub> [13, 14]. We assume that diversity of sputtering conditions (first pertinent of all – the oxygen content in the sputter chamber) leads to the formation of diversely different compounds. Furthermore, if conditions fluctuate during the sputtering process, this leads to formation of a nonstoichiometric film: XPS analysis confirms structural differences at different film depths in the film samples.

The XPS data for good samples is profiled by the data in Table 1. The surface contamination (mainly C, OH groups and water oxygen) was removed after 50–100 s of sputtering during XPS process, after then the stoichiometric ratio was measured, with the reservation that a tendency for Ti metallization is encountered.

Non-stable conditions and/or non-homogeneity of the process can all lead to defect formation, which provides crystallization centres. Failure to prevent high temperatures in the wafer also leads to crystallization of sputtered film, whereas samples maintained at low temperature do not crystallize during sputtering. It is possible that high temperature affected crystallization by itself or crystallization was a result of local extremely high temperature at some places on the substrate. But low temperature certainly prevents crystallization during the sputtering process.

Factors which are taken into account in the choice of a contact material are: quality of adhesion, temperature stability, unstressed growth during sputtering and stresses induced into a film during post-sputtering annealing (pulling samples through the hot zone). In order to find an appropriate metal for contact, five metals such as Au, Ag, Cr, W, and Mo were examined. Some of these metals have drawbacks: Ag does not

allow elevated heating; Au has poor adhesion to SrTiO<sub>3</sub>; when Mo was used as the bottom layer, no stress changes were observed after pulling through the temperature gradient (the reason for such behavior is unclear and it is now under investigation). Cr and W were found to be suitable candidates for a metal contact layer. Good SrTiO<sub>3</sub> adhesion on these metals allows the growth of homogeneous defect-free films.

The time dependent pyroelectric signal generated in response to the laser switching was recorded and compared with the theoretical predictions. As shown in Ref. [9], this pyroelectric signal must satisfy the following:  $I^2(t) \sim 1/t$  ( $I$  is the electric current,  $t$  – time), in accordance with theory. In our experiments, the same pyro electric behavior was found for all samples. Samples with two identical metal contacts, top and bottom, were used for the elimination of contact potential differences.

## 4. Conclusion

Modifications to the standard 306 Edwards sputtering have been described, implemented and tested. It was shown that they lead to reproducible fabrication of films of high quality, quasi-amorphous perovskite pyroelectric thin films in this case, as confirmed by XPS data and pyroelectric measurements.

It should be stressed that not only are the modifications to the sputtering system itself essential, but also author's recommendations regarding the preparation procedures for making the films, are indeed a critically important factor for achieving successful results. Important factors for film fabrication are: the temperature regime (less than 70 °C on the sample) as well as the gas ratio of the flow for two gases during sputtering.

The authors hope that their sputter modifications and recommendations will be used for the preparation of thin films from other materials, and for more general uses than the fabrication of quasi-amorphous pyroelectric films.

## Acknowledgements

We thank Prof. Igor Lubomirsky for fruitful discussions, Dr. Hagai Cohen and Dr. Tatyana Bendikov for detailed XPS analyses, and M.Sc. Sergey Khodorov for picture processing.

This work was partly supported by The Center for Absorption in Science, and in accordance with Agreement No.710546.

## References

- [1] <http://www.edwardsvacuum.com/Products/List.aspx?r=125>, Edwards Limited (2010).
- [2] AKTHER H., BHUIYAN A.H., *New J. Phys.*, 7 (2005), 135.
- [3] DAI N.V., THUAN N.C., HONG L.V., PHUC N.X., LEE Y.P., WOLF S.A., NAM D.N.H., *Phys. Rev. B*, 77 (2008), 132406.
- [4] <http://microlab.berkeley.edu/labmanual/chap6/edwards.pdf> (2010).
- [5] LYAHOVITSKAYA V., ZON I., FELDMAN Y., COHEN S.R., TAGANTSEV A.K., LUBOMIRSKY I., *Adv. Mater.*, 15 (2003), 1826.

- [6] LYAHOVITSKAYA V., FELDMAN Y., ZON I., WACHTEL E., GARTSMAN K., TAGANTSEV A.K., LUBOMIRSKY I., *Phys. Rev. B*, 71 (2005), 094205.
- [7] EHRE D., LYAHOVITSKAYA V., TAGANTSEV A.K., LUBOMIRSKY I., *Adv. Mater*, 19 (2007), 1515.
- [8] FRENKEL A.I., FELDMAN Y., LYAHOVITSKAYA V., WACHTEL E., LUBOMIRSKY I., *Phys. Rev. B*, 71 (2005), 024116.
- [9] EBRALIDZE I., LYAHOVITSKAYA V., ZON I., WACHTEL E., LUBOMIRSKY I., *J. Mater. Chem.*, 15 (2005), 4258.
- [10] WEN X.-D., CAHILL T.J., GEROVAC N.M., BUCKNUM M.J., HOFFMANN R., *Inorg. Chem.*, 49 (2010), 249.
- [11] SHIBUYA K., DITTMANN R., MI S., WASER R., *Adv. Mater.*, 22 (2010), 411.
- [12] CRANDLES D.A., NICHOLAS B., DREHER C., HOMES C.C., MCCONNELL A.W., CLAYMANB P., GONG W.H., GREEDAN J.E., *Phys. Rev. B*, 59 (1999), 12842.
- [13] CALVANI P., CAPIZZI M., DONATO F., LUPI S., MASELLI P., PESCHIAROLI D., *Phys. Rev. B*, 47 (1993), 8917.
- [14] YAN X.B., XIA Y.D., XU H.N., GAO X., LI H.T., LI R., YIN J., LIU Z.G., *Appl. Phys. Lett.*, 97 (2010), 112101.

*Received 22 November 2010*

*Revised 31 January 2011*

## Contents

P. S. Sahoo, A. Panigrahi, S.K. Patri, R.N.P. Choudhary, Impedance and modulus spectroscopy studies of $Ba_4SrSmTi_3V_7O_{30}$ ceramics.....	763
H. Sahan, H. Göktepe, S. Patat, Cycling behaviour of barium doped $LiMn_2O_4$ cathode materials for Li ion secondary batteries .....	773
W. Wang, Q. Ling, M. Lin, Q. Chen, A study of a block copolymer synthesized by RAFT polymerization containing carbazole groups and a europium complex .....	781
M. Sahin, H. Celikkan, A. Asan, M.L. Aksu, The effect of Congo red inhibitor on the corrosion of various steels in a 3.5% NaCl medium.....	795
Y. Zhang, Y.H. Tang, E.L. Zhang, L.W. Lin, L.Z. Pei, Preparation of Ni/MgO catalysts for carbon nanofibres by a self-propagating low temperature combustion process.....	805
P. Ou, G. Xu, C. Xu, Y. Zhang, X. Hou, G. Han, Synthesis and characterization of magnetite nanoparticles by a simple solvothermal method .....	817
Y. C. Chi, Y. Liou, Room temperature ferromagnetism in Si nanocaps on self-assembled glass beads.....	823
A. Yoffe, V. Shelukhin, Modification of 306 Edwards sputtering system for the reproducible fabrication of sensitive thin films .....	833